University of New Mexico
UNM Digital Repository

Chemical and Biological Engineering ETDs | Engineering ETDs

8-31-2011

Novel routes for synthesis of Pd nanoparticles and faceted ZnO supports for heterogeneous catalysts

Patrick David Burton

Follow this and additional works at: https://digitalrepository.unm.edu/cbe_etds

Recommended Citation
Burton, Patrick David. "Novel routes for synthesis of Pd nanoparticles and faceted ZnO supports for heterogeneous catalysts." (2011).
https://digitalrepository.unm.edu/cbe_etds/11

This Dissertation is brought to you for free and open access by the Engineering ETDs at UNM Digital Repository. It has been accepted for inclusion in Chemical and Biological Engineering ETDs by an authorized administrator of UNM Digital Repository. For more information, please contact disc@unm.edu.

Patrick D. Burton
Candidate

Chemical Engineering
Department

This dissertation is approved, and it is acceptable in quality and form for publication:

Approved by the Dissertation Committee:

, Chairperson

Novel routes for synthesis of Pd nanoparticles and faceted ZnO supports for heterogeneous catalysts

by

Patrick David Burton

B.S. Chemical Engineering, New Mexico Institute of Mining and Technology 2006

M.S. Chemical Engineering, University of New Mexico 2009

DISSERTATION

Submitted in Partial Fulfillment of the

Requirements for the Degree of

Doctor of Philosophy

Engineering

The University of New Mexico

Albuquerque, New Mexico

May, 2011

©2011, Patrick David Burton

Dedication

To my parents, Paul and Kathy.

Acknowledgments

I am grateful to my adviser, Prof. Abhaya Datye for his support and guidance throughout my graduate studies.

I will also take this opportunity to thank Dr. Timothy J. Boyle for allowing me to conduct nanoparticle and oxide support synthesis experiments at Sandia National Laboratories' Advanced Materials Laboratory. I thank the members of the Datye and Boyle research groups; Valerie Ashbacher, Elena Berliba-Vera, Sivakumar Challa, Noel Dawson, Andrew DeLaRiva, Thu Doan, Tyne Johns, Barr Halevi, Sarah Hoppe, Leigh Anna Ottley, Jonathan Paiz, Eric Peterson, Hien Pham, Alia Saad, Angelica Sanchez, Aaron Roy, Derek Wichhart and Daniel Yonemoto.

I thank Geoff Courtin for assistance with the acetylene hydrogenation reactor.

In addition, I appreciate the assistance of Dr. Ying-bing Jiang and Dr. Shenghong Huang for their assistance in using the Jeol 2010F microscope.

I will also take this opportunity to thank Dr. Susan Atlas, Prof. Boris Keifer, Dr. Frank Abild-Pederson and Dr. Felix Studt for their mentorship on the density functional theory portion of this work.

My research has been supported by the United States Department of Energy, Office of Basic Energy Sciences under contract number DE-FG02-05ER15712, and the Partnership for International Research and Education (PIRE) under the National Science Foundation, grant number OISE 0730277. The research conducted has been augmented by the electron microscopy facilities at the University of New Mexico which are supported by the NSF EPSCOR and NSF NNIN grants.

Finally, I thank the members of the committee, Prof. Abhaya Datye, Dr. Timothy J. Boyle, Prof. Dimiter Petsev and Prof. Rick Kemp.

Novel routes for synthesis of Pd nanoparticles and faceted ZnO supports for heterogeneous catalysts

by

Patrick David Burton

ABSTRACT OF DISSERTATION

Submitted in Partial Fulfillment of the

Requirements for the Degree of

Doctor of Philosophy

Engineering

The University of New Mexico

Albuquerque, New Mexico

May, 2011

Novel routes for synthesis of Pd nanoparticles and faceted ZnO supports for heterogeneous catalysts

by

Patrick David Burton

B.S. Chemical Engineering, New Mexico Institute of Mining and Technology 2006

M.S. Chemical Engineering, University of New Mexico 2009

Ph.D, Chemical Engineering, University of New Mexico, 2011

Abstract

Alcohol steam reforming is a promising source of hydrogen as fuel, and could be improved by the use of an optimal catalyst. The methanol steam reforming reaction, $\mathrm{CH_3OH} + \mathrm{H_2O} \rightarrow 3\mathrm{H_2} + \mathrm{CO_2}$ is frequently conducted by means of a Cu/ZnO catalyst. Unfortunately, this catalyst deactivates quickly and is pyrophoric. Pd catalysts are much more stable, but reactions using these catalyst follow the decomposition pathway, $\mathrm{CH_3OH} \rightarrow 2\mathrm{H_2} + \mathrm{CO}$. PdZn alloys can achieve the desired selectivity, and have been noted to form under reaction conditions from Pd/ZnO heterogeneous catalysts. In the present work, careful synthesis techniques of specific support and nanoparticle surfaces have been developed to gain a better understanding of the interaction between each phase.

Synthesis focused on preferential exposure of the most active surface of each material. In the case of ZnO, the polar facets of the crystallite were desirable. These high-energy

surfaces are less commonly exposed than non-polar facets in typical powders. Tailored platelet shapes were produced in solution by restricting the growth along the (0001) direction, producing thin crystallites. The surfaces of these crystallites were primarily (0001) surfaces, and *en masse* constituted a high surface area powder, ideal for use as a catalyst support.

For the Pd nanoparticle phase, small particles are necessary for high activity. Synthetic techniques to produce nanoparticles typically use organic capping material, which was shown here to be detrimental to the overall activity. A simpler technique was developed in which methanol was used to reduce a Pd precursor in solution without capping agents. This method was effective when depositing Pd on carbon, and has been shown to be strongly dependent on surface chemistry when used with oxide supports. By manipulating the oxide surface with simple solvents, this technique has been generalized for the synthesis of supported nanoparticle catalysts.

Contents

List of Figures

List of Tables

Glossary

$\frac{W}{F}$	Space time, given in units of catalyst weight per flow rate, $\frac{kg \cdot s}{gmol}$
reflux	A technique where a single pass shell and tube heat exchanger is fitted to the top of a reaction flask to condense effluent vapor and return it to the reaction.
SEM	Scanning Electron Microscopy uses a focused electron beam (usually low energy, 2-10 kV) to image a sample. The two imaging modes used in this study are secondary electron (SE) and backscattered electron (BSE).
TEM	Transmission Electron Microscopy differs from SEM by the intensity of the electron beam used. Whereas the SEM uses low energy electrons to interact with the surface, a TEM uses a high energy (200 kV) beam to penetrate the sample and produce a projected image.
XRD	X-ray diffraction is used to study the crystallographic structure of a material. Incident X-rays are projected onto a sample and are diffracted by the crystallites present. The diffraction pattern corresponds to the material present and the size of the crystallites.
PEM	Proton Exchange Membrane fuel cells use a semipermeable membrane to split hydrogen into protons and electrons. The protons pass through the membrane and a subsequent electrolyte to a cathode. The electrons are

	transported outside the electrolyte through an external load and reintroduced to the protons at the cathode.
TGA/DTA	Thermogravimetric analysis and differential thermal analysis are two related techniques integrated into the same instrument. TGA measures the mass loss of the sample as it decomposes, and DTA compares the temperature difference between the sample and a reference.
BET	The Brunauer, Emmet and Teller method [9] of determining surface area by gas adsorption.
MSR	Methanol Steam Reforming: $CH_3OH+H_2O \rightarrow CO_2+3H_2$
GC	A Gas Chromatograph is used to separate constituent gases by flowing them through a porous column. Samples were run under isothermal conditions, depending only upon elution time to identify each gas (acetylene, ethylene and ethane).

Chapter 1

Introduction

Lithium ion batteries have enabled the development of an entire ‘ecosystem’ of portable electronic devices. The continuing progression of smaller batteries with higher capacity and improved lifespan stimulates the idea of reaching a Moore’s Law conundrum in power technology. How small and how dense can batteries get? Just as the semiconductor industry is facing material limitations to how much smaller chips can be made, there is a physical limit to the capacity of a battery. The most dense energy carriers are liquid fuels, which are fed to fuel cells to produce electric current. There are two options for using a liquid fuel; reform a small hydrocarbon to produce hydrogen, which is then fed to the fuel cell, or feed that hydrocarbon directly to a compatible fuel cell.

1.0.1 Background of Fuel Systems

The two fuel cell types considered here are reformed hydrogen polymer exchange membrane (H_2PEM) devices and direct methanol PEM fuel cells (DMFC). Both operate on the same basic platform; the key difference is in the fuel delivery. The simplest fuel in terms

of reaction is the oxidation of hydrogen to water (reaction 1.1).

$$\mathrm{H_2} + \frac{1}{2}\mathrm{O_2} \rightarrow \mathrm{H_2O} \qquad \Delta \mathrm{H_f} - 285.5 \frac{\mathrm{kJ}}{\mathrm{mol}} \tag{1.1}$$

The reaction is energetic and produces one of the most benign products possible, water. Unfortunately, transporting the necessary hydrogen as fuel for this reaction is difficult. Compressed hydrogen is dangerous to store, and likewise cumbersome to transport, so it is not an ideal fuel for portable applications. Other options include storing the hydrogen in a metal hydride, or reforming it on-site from a liquid hydrocarbon. Metal hydrides store atomic hydrogen within the interstitial spaces of a lattice, which allows for the storage of hydrogen without the danger of spontaneous tank decompression as is the fear with a compressed hydrogen storage system. There is a large body of work dedicated to finding suit-

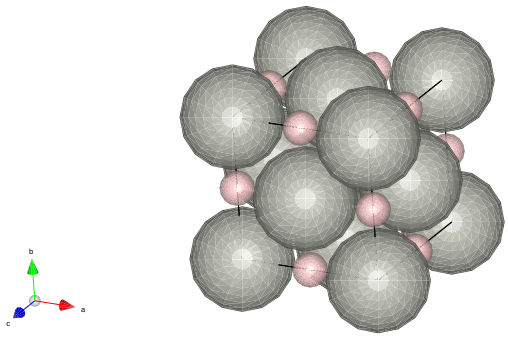

Figure 1.1: Schematic of a metal hydride (PdH) where H atoms (pink) fill in the interstitial spaces between the Pd atoms (grey). Structure courtesy of Downs and Hall-Wallace [1], rendered using VESTA [2].

able hydrides that can be cycled to absorb and release hydrogen in a safe and predictable manner. While promising for automotive applications, metal hydride storage is not an optimal system for personal electronic devices. The most feasible solutions to powering portable electronic devices are to reform a hydrocarbon to produce hydrogen on demand, or use the hydrocarbon directly. Short chain alcohols, such as methanol or ethanol are the most frequently considered hydrocarbons as potential fuels. These liquids are viable options because they have a reasonably high energy density (see table 1.1) and are easily

transported. According to Rashidi et al. [10], methanol has been recently approved by the DOE for transport aboard aircraft.

Fuel	Volume (mL)	Mass (g)
Lithium ion battery	600	1000
$H_{2,gas}$	340	920
$H_{2,liquid}$	95	
$H_{2,metal\ hydride}$	95	530
MeOH	33	26
Diesel	13	13

Table 1.1: Energy density of common energy carriers to deliver 150 Wh, adapted from Browning et al. [8]

DMFC

Incoming methanol and water are fed to the fuel cell, where it is contacted with oxygen in one of two ways. In an active DMFC, a stoichiometric quantity of oxygen is injected into the system, where it reacts with a likewise stoichiometric quantity of MeOH. In contrast, a passive DMFC relies on available oxygen from the atmosphere to react with an unmonitored influx of MeOH. According to Rashidi et al. [10], active DMFCs are high-maintenance, high output devices, whereas passive DMFCs are low-maintenance, low output devices. In either case, the incoming MeOH/water solution is contacted with a PtRu catalyst to produce 6 protons and electrons, of which the electrons are directed through a working circuit, and the protons pass through the electrolyte to the cathode. Once at the cathode, the protons react with the completed circuit and incoming oxygen to produce water. A significant drawback to the DMFC is methanol crossover, where MeOH crosses the through the electrolyte with the protons, as discussed in section 1.1.

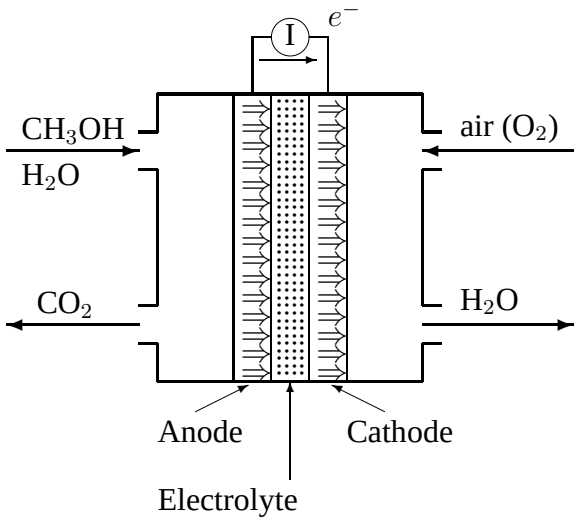

$$\text{Anode} : CH_3OH + H_2O \rightarrow 6e^- + 6H^+ + CO_2 \tag{1.2}$$

$$\text{Cathode} : \frac{3}{2}O_2 + 6e^- + 6H^+ \rightarrow 3H_2O \tag{1.3}$$

$$\text{Overall} : CH_3OH + \frac{3}{2}O_2 \rightarrow 2H_2O + CO_2 \tag{1.4}$$

Figure 1.2: Schematic of a DMFC fuel cell system, adapted from Karim [3].

H_2PEM

A steam reformed methanol H_2PEM relies upon a pretreatment to convert MeOH to hydrogen. An incoming aqueous MeOH solution is passed over a catalyst bed to reform the methanol into hydrogen and CO_2, as illustrated by reaction 1.5.

$$CH_3OH + H_2O \rightarrow 3H_2 + CO_2 \tag{1.5}$$

$$CH_3OH \rightarrow 2H_2 + CO \tag{1.6}$$

$$3H_2 + CO_2 \rightleftharpoons CO + H_2O \tag{1.7}$$

Since steam reforming is a gas-phase reaction, the feed must be vaporized as it enters the reforming unit. The heat is provided by combusting excess hydrogen redirected from the fuel cell stack. The remaining hydrogen is then stripped of the electron at the anode and passed through the electrolyte. After completing an electric circuit, the electron recombines with the hydrogen and oxygen from the air at the cathode. In a self-contained system, the waste water is recycled into the methanol feed.

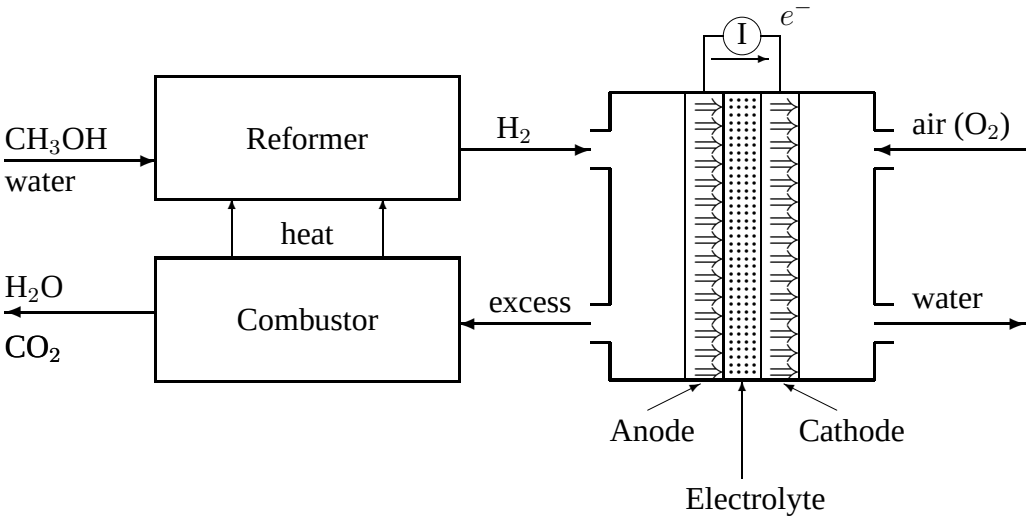

$$\text{Anode} : 2H_2O + H_2 \rightarrow 2H_3O^+ + 2e^- \tag{1.8}$$

$$\text{Cathode} : \frac{1}{2}O_2 + 2H_3O^+ + 2e^- \rightarrow 3H_2O \tag{1.9}$$

$$\text{Overall} : 2H_2O + 2H_2 + \frac{1}{2}O_2 \rightarrow 3H_2O \tag{1.10}$$

Figure 1.3: Schematic of a H_2PEM, courtesy of Karim [3].

The use of an appropriate catalyst is of the highest importance to this reaction, because it is possible for MeOH to decompose directly to hydrogen and CO (reaction 1.6). CO is undesirable because it is a health hazard and poisons PEM membranes. It is necessary to

use a selective catalyst that will avoid the production of CO as much as possible. It is not possible to produce exclusively CO_2 due to the reverse water-gas shift (reaction 1.7). The reverse water-gas shift is an equilibrium between the products of the MeOH reforming reaction (reaction 1.5) and less desirable products. To further illustrate the similarities between the two systems, note reactions 1.2 and 1.5. The anode of a DMFC is effectively a methanol reforming reactor. On the basis of the reactor system, the H_2PEM system appears to be much more cumbersome than its direct methanol counterpart; however, there are important design aspects to be considered.

1.1 Balance of Plant

Both of the systems presented in this study share a very similar operating chemistry. The key difference between them is in the way that the reaction is managed by the balance of plant. From initial inspection, it would seem that a H_2PEM fuel cell would require more hardware to provision the cell. The fuel cannot be used directly, so in addition to the fuel cell itself, the H_2PEM requires a reforming unit to pretreat the fuel. The ostensibly less complex DMFC does not require fuel pretreatment; however, it suffers from fuel diffusion through the cell, termed crossover. Fuel crossover reduces the cell potential and, depending on the system, may require post-processing by a recycle stream.

1.1.1 Methanol Crossover

According to Aydinli et al. [11], the most vital component to an active DMFC is a methanol sensor to combat fuel crossover. Methanol can diffuse through the membrane very readily and react with oxygen at the cathode [12, 13], see reaction 1.11.

$$\mathrm{CH_3OH} + \mathrm{O_2} \rightarrow \mathrm{CO} + 2\mathrm{H_2O} \tag{1.11}$$

This competing reaction does not contribute to the external electrical load, and is thus a loss to the system. Instead of electrons flowing through an outside circuit, they are retained by the MeOH and lower the potential at the cathode. Furthermore, methanol oxidation depletes the available oxygen to complete the cathodic reaction, thereby reducing the total output. This is an especially problematic scenario for actively fed systems that rely on a stoichiometric supply of oxygen. The control systems used to ensure a stoichiometric feed must be constantly overtaxed to combat crossover. This naturally requires a more robust, larger, and more energy-expensive monitoring and control system to perform continuous corrections. If methanol crossover did not occur, it is conceivable that the control system would only need to modulate minor fluctuations in the fuel and oxygen streams and could be much less complex. Passive systems would not suffer quite as much from oxygen consumption, as the feed is non-stoichiometric to begin with.

The opportunity for methanol crossover to occur stems from the nature of the oxidation reaction at the anode. The oxidation of MeOH is relatively slow [14], so there is a high chance of MeOH passing through the membrane unreacted or partially reacted. Furthermore, in a DMFC, the methanol concentration gradient is greatest at the anode, so in addition to slow kinetics, there is a strong driving force for MeOH to diffuse. Since crossover is caused by diffusion, both the temperature [11, 13] and fuel concentration must be reduced to limit fuel loss. A lower MeOH concentration provides less of a driving force for diffusion to occur; however, the cost comes in reduced capacity by carrying less fuel.

1.1.2 Catalyst Efficiency and Thermal Management

Since the methanol in a reformed H_2PEM is vaporized and nearly entirely converted to hydrogen and side products, fuel crossover does not exist in a H_2PEM. What little MeOH might remain unconverted is a very small percentage of the total fuel, so it is unlikely to diffuse through the membrane. Unreacted MeOH is an inefficiency of the system, but is

due to an insufficient catalyst, not diffusion. The catalyst used in the steam reforming unit

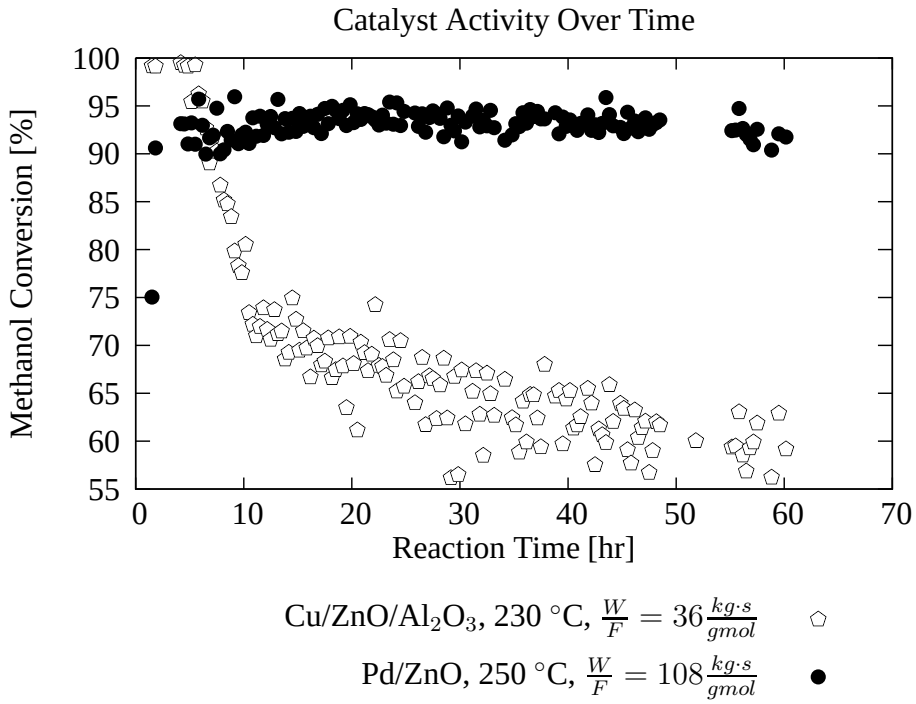

Figure 1.4: Methanol steam reforming catalysts demonstrate various degrees of activity and stability. $Cu/ZnO/Al_2O_3$ based catalysts are highly active, however, they deactivate quickly. Pd/ZnO catalysts are much more stable, however, are significantly less active.

is a key focus of research for H_2PEM systems, as noted by several researchers [3, 15–17]. There are several aspects to improving the catalyst; activity, CO_2 selectivity, and stability. Current commercial catalysts are $Cu/ZnO/Al_2O_3$, which demonstrate a high initial activity, but degrade quickly (see Figure 1.4). Furthermore, Cu based catalysts are pyrophoric and thus undesirable in a mobile system [3]. Pd/ZnO catalysts demonstrate much greater stability (Figure 1.4); however, are significantly less active. The required mass of the Pd/ZnO catalyst is three times greater than the corresponding Cu catalyst for the same flow rate of MeOH to achieve the same conversion. Thus, while it is possible to achieve very high conversion of MeOH to H_2 and CO_2, it is not yet practical. A further complication

of reforming methanol is that Pd tends to decompose MeOH rather than reforming it to hydrogen, as illustrated in reaction 1.12.

$$CH_3OH \rightarrow 2H_2 + CO \tag{1.12}$$

The selectivity of the reaction to proceed towards methanol reforming rather than decomposition is dependent on the type of catalyst used. The polymer membrane used in H_2PEM

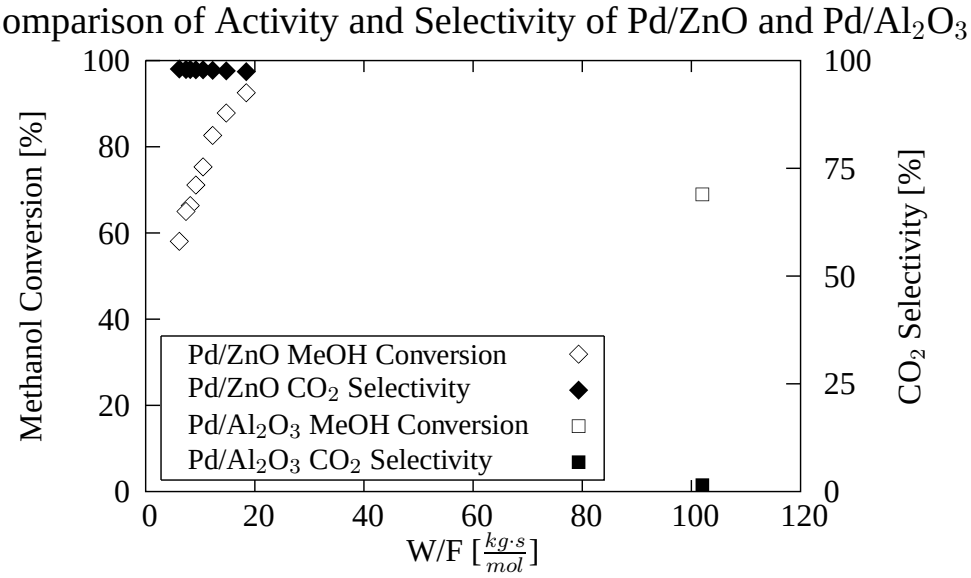

Figure 1.5: Pd/ZnO catalysts demonstrate high conversion (◊) and selectivity (♦), while Pd/Al_2O_3 catalysts show poor conversion (□) and non-existent selectivity (■) towards CO_2.

systems is sensitive to CO poisoning, so it is desirable to avoid production of CO during the reforming reaction. This is especially important in mobile systems, where the weight, volume, and operating energy of a CO scrubbing unit are undesirable. Pd/ZnO catalysts show the greatest utility for steam reforming, but still require improvement to ensure a high activity and near complete conversion.

A consequence of near complete vapor phase conversion is the thermal management of the system. Methanol steam reforming catalysts are active at 250 °C [3, 15], which can

rapidly become a problem for small devices. A notebook computer operating at such a temperature would not be particularly user friendly, though it would be a 'hot' consumer product. The functionality of the product would be entirely dependent on effective insulation, or separating the reforming unit from the electronic device. The effectiveness of insulation would dominate the portability of the product. If an additional centimeter of insulation was required for a cellular phone, the product would be regarded as bulky by modern design standards. A notebook computer or other somewhat larger electronic device could survive the application of an extra layer of insulation. Separating the reforming unit could be useful to low demand customers, who could use a large reforming unit as a hub to provide hydrogen for individual electronic devices. This application does significantly reduce the portability of the system, so it seems to be an unlikely solution.

1.2 Summary

The two devices studied are variations of reactors designed for the same reaction. A DMFC reforms methanol in a liquid phase by an electronic process, and a H_2PEM achieves the same result by a gas phase thermal process. The phase of the reactants is the critical difference between the two systems. The greatest challenge in deploying DMFCs is methanol crossover, which limits the design of the entire system. Crossover MeOH lowers the potential of the system by competing for oxygen at the cathode. Since stoichiometric feed is required for high output devices, such competition severely impacts the performance of the device. Passive DMFCs would logically be the optimum implementation of DMFC technology in low power demand electronics.

In H_2PEM fuel cells, vaporizing the fuel provides the necessary driving force to avoid fuel diffusion later in the fuel cell stack. The greatest concern in these systems is the onboard reformer, which requires high temperatures to operate. Improving the performance of the H_2PEM fuel cell could be achieved by using a more active catalyst which is effective

at lower temperatures.

1.3 Selectivity improvement by alloy formation

Copper based catalysts are currently used in industrial syngas plants, but suffer from the limitations discussed previously. Palladium based catalysts are much more stable, but are not as active or selective under all conditions. Iwasa and Takezawa [4] demonstrated that the selectivity towards CO_2 production of various Pd-based catalysts depends on the support used. Since this discovery, the interaction between Pd and ZnO has been extensively

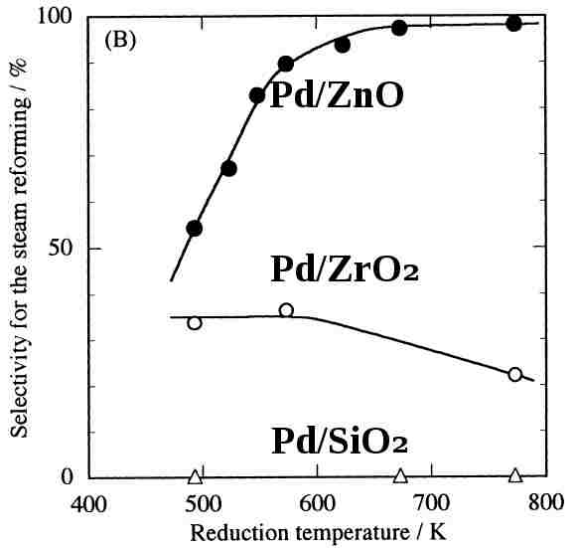

Figure 1.6: Selectivity of Pd/ZnO, Pd/ZrO_2 and Pd/SiO_2 as a function of reduction temperature. From Iwasa and Takezawa [4]

studied from an experimental and theoretical approach. The increase in selectivity as reduction temperature increases (Figure 1.6) is a particularly interesting phenomenon. Work by Conant [18] has shown that a bimetallic PdZn phase forms under reaction conditions. It was suggested that Zn migrated from the support to the Pd particles, producing the desired PdZn phase. This process was described as a self-healing mechanism, leading to

enhanced stability of the catalyst over several cycles. The improvement in selectivity of PdZn compared to Pd is believed to be caused by the similar electronic structures of PdZn and Cu. Chen et al. [19] have shown that the Cu density of states matches PdZn closely. The similarities between *d*-band states was further investigated by Lim [16, 20] to verify a proposed reaction mechanism for methanol steam reforming and decomposition. In that work, methoxide decomposition was found to be much more favorable on Pd than Cu or PdZn. Further dehydrogenation lead to CO, the undesired product in reaction 1.6. The critical difference in steam reforming or decomposition is the scission of the C-O anc C-H bonds. In the case of Pd catalysts, dehydrogenation is much more favorable, leading to a single CO molecule. Stepped Cu and PdZn surfaces were found to increase the C-H bond breaking barrier, and improve CH_2O binding, an important intermediate to CO_2 production. The authors noted that small islands of metallic Pd could be responsible for some CO production in experimental catalysts. In conjunction with the findings of Conant [18], there is an apparent need to understand the formation of PdZn under the most ideal conditions.

1.4 Previous reports of PdZn formation

The PdZn alloy formation reported by Conant [18] was the result of reducing a Pd/ZnO catalyst after it had been charged to the reactor. This was an effective, but non-specific technique which left questions about the formation of the most active phase. Particle size and composition varied widely, which complicated the analysis. Karim et al. [21] reported an unexpected *lack* of size dependence on selectivity, as particles up to 30 nm in diameter were selective catalysts. Improving the uniformity requires precise control over both the metal and oxide phases. This is easily achievable under ultrahigh vacuum conditions, in which precise amounts of metal can be sputtered onto a substrate of choice [22–24]. Unfortunately, large scale production of powder catalysts cannot use this technique due to

the porosity of powder substrates. Aqueous synthesis is much simpler, and only requires precipitation of solvated $Pd(NO_3)_2$ and $Zn(NO_3)_2$ in a desired ratio. The resulting product is highly disordered (Figure 1.7a) and therefore not suitable for detailed study. In the same work, an organic precursor ($Pd(OAc)_2$) was dissolved and added drop-wise to the powder until the pore volume was filled (incipient wetness, Figure 1.7b). The powder was then

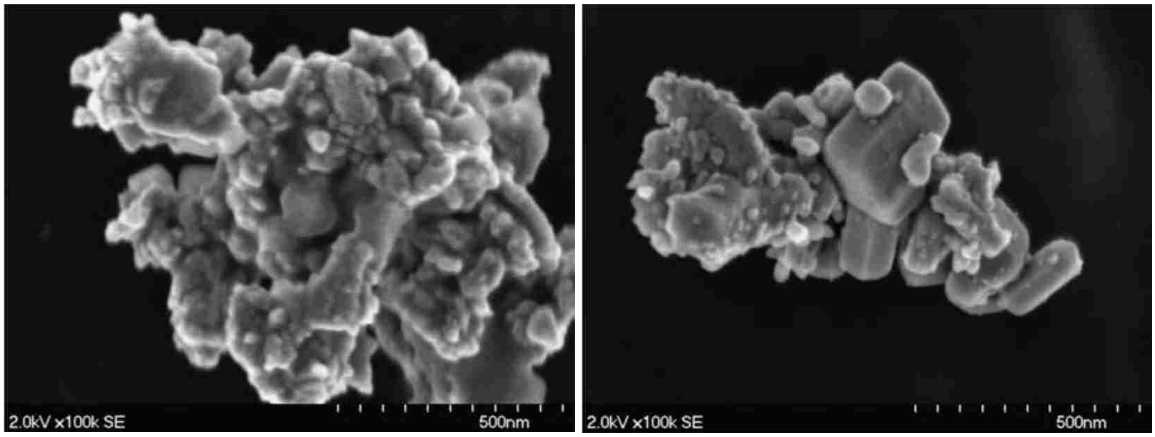

(a) Coprecipitation (b) Incipient wetness

Figure 1.7: Conventionally prepared Pd/ZnO samples prepared by [5].

dried and the process repeated until the total volume of dissolved precursor had been used. While time-consuming, this process did produce a more uniform catalyst, with distinct Pd regions coating the ZnO crystallites. The large aggregates produced were also not ideal for a study of Pd-Zn interaction at the interfacial level.

1.5 Problem statement

In order to improve the understanding of PdZn bimetallic formation, and the performance of catalysts in general, it is necessary to develop highly uniform, but practical heterogeneous catalysts. Such catalysts must be suitable for continuous flow reactors, simple to prepare, and provide high surface area for metal-support interaction.

Chapter 2

Synthesis and Activity of Heterogeneous Pd/Al_2O_3 and Pd/ZnO Catalysts Prepared from Colloidal Palladium Nanoparticles

2.1 Introduction

Though widespread, the use of portable electronic equipment remains a function of the portability of the power source. Even the best battery is limited to a finite run time with a fairly low energy density, and requires convenient access to an electrical source to recharge. Furthermore, the battery typically comprises a significant percentage of the size and weight of an electronic device. An alternate solution is to use a liquid fuel, which has a very high energy density, can be easily transported, and provides a much longer lifespan than a typical battery.

Methanol, in particular, is desirable to use as a source for hydrogen because it under-

goes few side reactions, does not contain sulfur, and is reformable at low (200-250 °C) temperatures. Methanol steam reforming is a very simple reaction, so undesirable side products can be minimized. Specifically, CO production can be avoided if the reaction conditions are selective towards the production of H_2 and CO_2 rather than H_2O and CO. The key to utilizing this reaction as a source of hydrogen is efficient, low temperature conversion of methanol.

It has been shown that PdZn alloys are active for methanol steam reforming and selective towards CO_2 [4, 25]. However, previous work in our group [21] and elsewhere [26] has shown that the synthesis method involves coprecipitation of palladium and zinc oxide from a highly acidic solution. This process destroys the ZnO morphology, which is believed to play some role in the final activity of PdZn catalysts. Furthermore, the synthesis methods presented previously require multiple precursor impregnation steps to achieve the desired high metal loading on the oxide. Once deposited, the precursors must be reduced to produce metallic particles.

One less caustic process would be to use an organic based precursor, such as palladium acetate ($Pd(OAc)_2$), which can avoid low pH solutions. This method does minimal damage to the ZnO while producing polydisperse Pd particles. In order to achieve both particle size control and maintain ZnO morphology, colloidal nanoparticle synthesis offers a great advantage over traditional catalyst synthesis from metal salts. Colloidal synthesis allows for a greater control over the nano-particle size while providing a narrow size distribution, the surfactant protects the nanoparticles from agglomeration, and can be removed to expose the surface for catalytic activity.

While other researchers have used acid-free techniques to prepare supported PdZn alloys [27, 28], and Cu/ZrO_2 [29], our work is focused on preparing particles *ex situ* and depositing them on an oxide support of our choice, without damaging the support in the process. Using solution precipitation methods similar to those described by [30] and [31], Pd/ZnO catalysts can be prepared without damage to the ZnO. In a typical procedure,

a metal precursor ($Pd(OAc)_2$) is decomposed in a surfactant (trioctylphosphine or octylamine), producing metal particles enshrouded with an organic capping agent. The organic ligand prevents particles from agglomerating in solution, however, it also restricts catalytic activity. It is necessary to remove the surfactant prior to use as a catalyst, yet this opens the possibility for particles to agglomerate.

This research investigates methods to produce Pd particles, immobilize them on an oxide surface, and then remove the surfactant. Herein, we present preliminary findings of monometallic palladium particles on oxide supports. Catalytic activity is probed by the use of CO oxidation to provide a consistent test reaction to evaluate various oxide supported catalysts. Our work demonstrates a method that incorporates a surfactant to stabilize the nanoparticles, and prevents support degradation by avoiding acidic precursors.

2.2 Experimental

2.2.1 Palladium Nanoparticle Synthesis and Catalyst Preparation

Two different synthesis routes were followed, each based on a common experimental set-up. First, an inert environment was prepared using a 50 mL three neck round bottom flask fitted with a reflux condenser connected to a Schlenk line. The remaining two ports were sealed and used either for a thermocouple support or reagent injection. One method made use of 0.081 g of "$Pd(Mes)_2$", (where Mes = $C_6H_2(CH_3)_3$-2,4,6, in-house intermediate), which was injected into 30 g (80 mmol) of trioctylphosphine (TOP, 90% technical grade, Aldrich). A separate procedure used 0.22 g (1.0 mmol) $Pd(OAc)_2$ (98%, reagent grade, Aldrich) mixed with 0.30 mL (2.0 mmol) of octylamine (Aldrich) and 0.20 g (7.5 mmol) 1, 2-hexadecanediol (90%, technical grade, Aldrich) in 20 mL (67 mmol) octylether (99%, Aldrich) and 0.30 mL (0.5 mmol) olelic acid (90%, technical grade, Aldrich). Both methods then required the system to be opened

to an argon atmosphere and heated to 300 °C using a temperature controlled heating mantle. After the reaction had proceeded for 30 min., the system was allowed to cool to room temperature. Once at room temperature, 50 mL of methanol (Reagent grade, Aldrich) was added to precipitate the particle micelles. The solution was centrifuged to recover the solid and the supernatant was discarded. The remaining solid was redistributed in hexanes (Aldrich, mixture of isomers). This process was repeated until the supernatant was clear. The amine route was further modified following a procedure described by Woehrle et al. [32] to partially substitute a thiol chain for some of the amine ligands. 0.085 mL (10 mol%) 6-mercaptohexanoic acid (90%, Aldrich) or 12-mercaptododecanoic acid (90%, Aldrich) were added to a vial of previously prepared amine-capped colloidal nanoparticle solution and shaken vigorously for five minutes to achieve partial substitution.

2.2.2 Catalytic Activity and Characterization

As-prepared NPs were added to 0.50 g alumina (Sasol) [TOP route] or 0.50 g zinc oxide powder (99.99%, Aldrich) [amine route, thiol-amine route] in 25 μl increments and agitated until the liquid was evenly dispersed throughout the powder. As-prepared samples were examined by TEM and STEM using a Jeol 2010F FASTEM field emission gun scanning transmission electron microscope with Oxford-Link energy dispersive spectroscopy (EDS). Images were taken at 200 kV accelerating voltage. Colloidal samples were pipetted onto a holey carbon 200 mesh copper grid (SPI Supplies) and allowed to dry. The particles were reexamined after CO oxidation to determine the extent of growth and agglomeration. The surfactant removal temperature was found by examining the decomposition temperature using DSC/TGA on a TA SDT Q600 in a temperature range of 0 to 700 °C. Calcined samples were heated at a ramp rate of 10 °C/min. to 80 °C, then 1 °C/min. to 120 °C and held for two hours. Afterwards, the temperature was increased to 350 °C at 5 °C/min. and held for three hours. EDS was used to examine samples for palladium content. CO oxidation was performed using a flow of 1.0% CO and 0.5% O_2 in a balance of helium

at a space velocity of 300,000 ml·h^{-1}·gmol^{-1}. Sample gas was passed through a 12 mm-i.d. glass column packed with Pyrex glass wool and 20 mg of either prepared sample or conventionally prepared (with $Pd(NO_3)_2$ similar to [21]) 0.3 wt% Pd/Al_2O_3 samples. Catalyst powder was crushed and sieved to ensure particles were between 106-250 μm in size. The tube was maintained at the desired reaction temperature by enclosing it in a covered heating mantle. Gas effluent aliquots were analyzed for CO, CO_2 and O_2 every 12 minutes using a Varian 3400 gas chromatograph. The sample chamber temperature was varied from 100 to 250 °C in 5 °C increments from 100 to 160 °C, then 10 °C increments thereafter. The temperature ramp was run three times on an automated system.

2.3 Results and Discussion

2.3.1 Pd/Al_2O_3 from TOP Route

During heating, the solution changed color from transparent brown to opaque black at 60 °C indicating decomposition of the precursor. The nanoparticles produced had an average diameter of 2.4 $\pm$ 0.4 nm, as determined by TEM images (Figure 2.1b). When examined by STEM (Figure 2.1a), the colloidal suspension disperses very evenly on the carbon grid. Average dispersion is approximately 500 particles per 1000 nm^2. This high loading on the carbon film was not observed on the Al_2O_3. Once mounted on Al_2O_3 (Figure 2.5) and oxidized, the particles were observed to grow slightly to 2.6 $\pm$ 0.7 nm. After calcination to 350 °C a bimodal distribution appears at 5 nm, however, the majority of the particles remained close to their original size (2.4 $\pm$ 0.4 nm $\rightarrow$ 2.9 $\pm$ 1 nm, Figure 2.2). Some growth can be expected after calcination, and in this case, the number of particles experiencing growth is low enough to consider the particles to be stable under reaction conditions. TGA analysis, shown in Figure 2.4, indicates that the TOP begins to decompose around 200 °C, but does not fully decompose until 500 °C. Our calcination

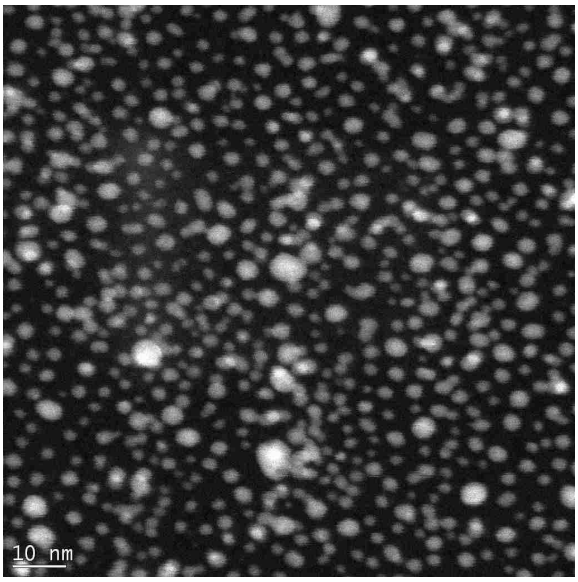

(a)

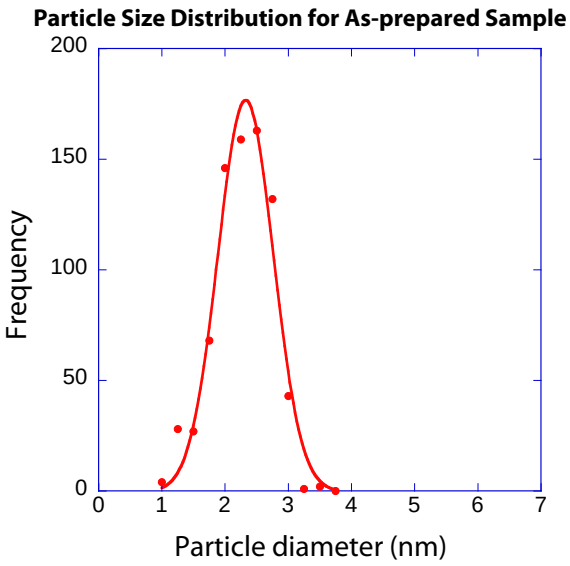

(b)

Figure 2.1: As-prepared TOP-encapsulated Pd particles (a) demonstrate a Gaussian distribution (b).

step was limited to a maximum of 350 °C to avoid particle agglomeration.

Most importantly, the catalytic activity of the calcined sample is seen to be greater than the non-calcined sample, indicating that the surfactant inhibits CO oxidation on the Pd particles. Both are capable of achieving a 100% conversion to CO_2, however, the calcined sample lights off at a much lower temperature as shown in Figure 2.6. For comparison, we also include the results for a 0.3 wt% Pd/Al_2O_3 sample. The conventionally prepared sample (average particle diameter of 4.0 nm) outperforms both laboratory samples with complete oxidation at 160 °C.

EDS spectra indicates that there is a very low Pd loading on the colloidal Pd catalyst since the Pd peak was below EDS detection limits. The activity of this sample, however, increases after the surfactant is removed via calcination.

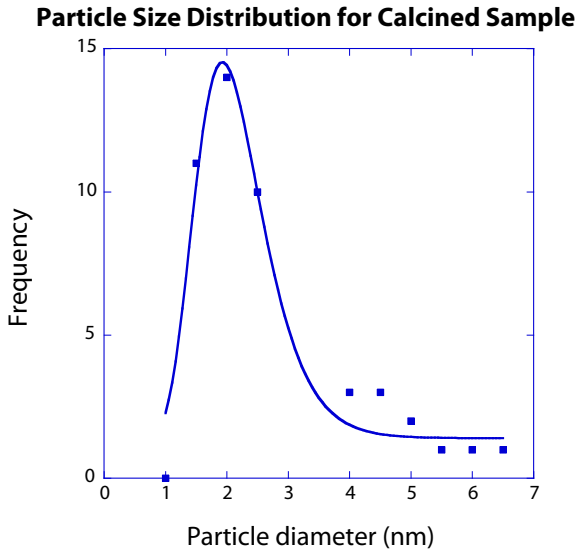

Figure 2.2: Size distribution of calcined Pd nanoparticles [TOP route] fit to a log normal distribution. The peak maximum of 2 nm is similar to that of the as-prepared sample, but an additional tail is seen past 5 nm.

2.3.2 Pd/ZnO from Amine Route

The amine capped nanoparticles tended to be larger than those produced by the TOP route. The average diameter was found to be 4 ± 1 nm for as-prepared particles. The synthesis proceeded in a similar manner to the TOP route (section 2.3.1). The most distinct difference is that the amine coated particles tended to cluster more than the TOP-coated particles (see Figure 2.7a compared to Figure 2.1a). In order to enhance the loading of Pd on the ZnO, the procedure used in section 2.3.1 was modified to include thiol functionalization to improve particle binding to the support. The thiol-amine particles were found to associate (Figure 2.7a) instead of attaching to the ZnO support as intended. While this is not ideal, the ZnO does remain highly faceted (Figure 2.7b, hexagonal face) even after the particles are deposited. No metal-metal interactions are believed to occur between the particles. The clustering effects observed are believed to be due to ligand entanglement. This excess ligand is believed to inhibit catalytic activity in CO oxidation and methanol

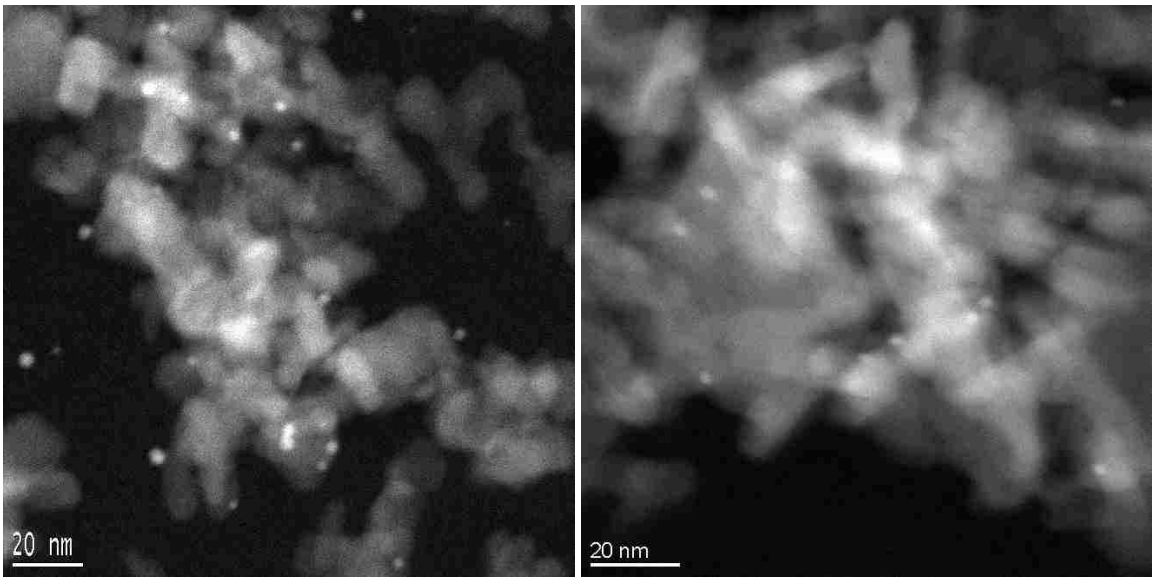

(a) (b)

Figure 2.3: (a) STEM image of Pd nanoparticles supported on Al_2O_3 after CO oxidation. A few larger particles are noticeably outside the 3 nm size range although the majority are smaller than 3 nm. (b) STEM image of calcined Pd/Al_2O_3 sample showing particles of a similar size as their pre-calcined counterparts.

steam reforming tests. Initial tests employed CO oxidation to compare to previous experiments with alumina supported catalysts. Both the amine capped and thiol capped particles demonstrated low activity compared to the 0.3 wt% conventional catalyst as shown in figure 2.8. Little difference is observed between the thiol capped and amine capped particles, suggesting that the activity of both samples is inhibited by the organic ligands. In contrast, the calcined sample (to 350 °C) shows significantly improved activity. The effect of ligand removal can be further corroborated by examining a TGA/DTA scan of the supported samples. The original sample (Figure 2.9, solid line) shows a significant weight loss at 180 °C. The post-calcination sample (medium dashed line) indicates that most of this weight loss is eliminated during calcination. This discrepancy between samples suggests that there is a significant amount of unbound organic material in the original sample. In order to improve catalytic activity, it is therefore necessary to remove all excess organic material

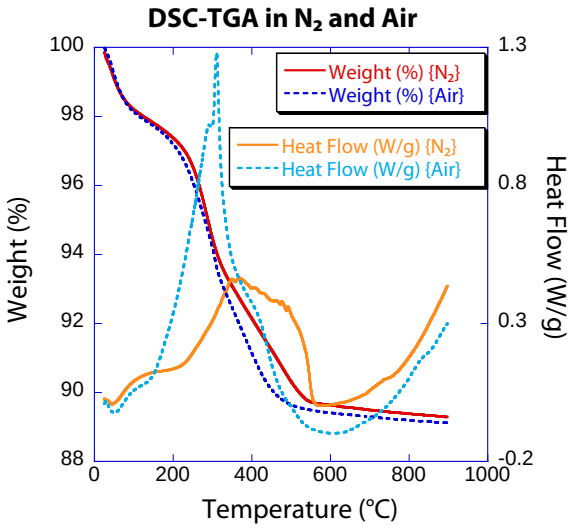

Figure 2.4: TGA/DTA plot of as-prepared [TOP route] Pd nanoparticles in N_2 (solid lines) and air (dashed lines). The particle encapsulating surfactant decomposes at 700 °C as evidenced by the weight loss curves (darker lines).

prior to depositing on an oxide support.

2.4 Conclusions

We have prepared Pd/Al_2O_3 and Pd/ZnO heterogeneous catalysts prepared from colloidal Pd nanoparticles and measured their activity for CO oxidation. Use of organic capping agents was shown to be detrimental to the activity of the catalyst. The organic component prevents particle agglomeration, yet, in doing so, the catalyst cannot achieve full potential activity. We have demonstrated that it is possible to improve the activity by removing the ligands. However, both the alumina and ZnO supported catalysts demonstrate very poor weight loading. Although the colloidal suspensions demonstrate very high loading on carbon TEM grids, we were not able to extend this high loading to the oxide supports. In this work, the prepared powders remained very light colored compared to the 0.3 wt % conventional catalyst. We believe that changing the interfacial interaction can help improve the

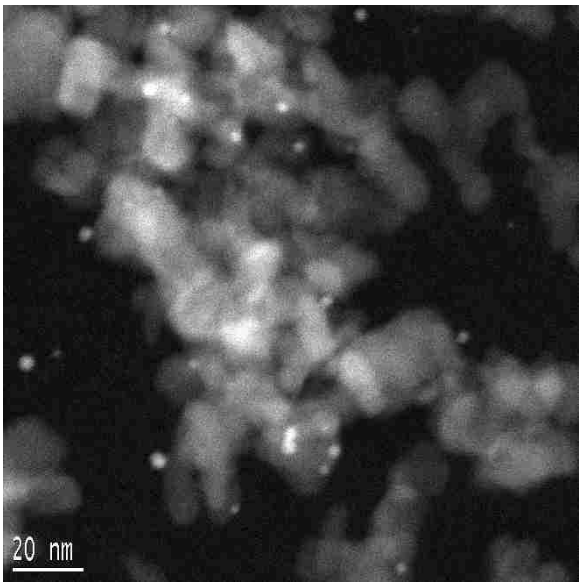

Figure 2.5: STEM image of Pd nanoparticles supported on Al_2O_3 after CO oxidation. A few larger particles are noticeably outside the 3 nm size range although the majority are smaller than 3 nm.

amount of sample deposited on the oxide. The organic ligands used in this work provide an alternative method to producing nanoscale palladium catalysts on an oxide support. The use of this method achieves the two desired properties: avoiding damage to the oxide support and preserving Pd particle size. However, it does introduce the problem of organic inhibition and does not provide high weight loading. We are currently investigating support chemistry and nanoparticle capping agent/support interactions to achieve higher particle adhesion to the oxide surface.

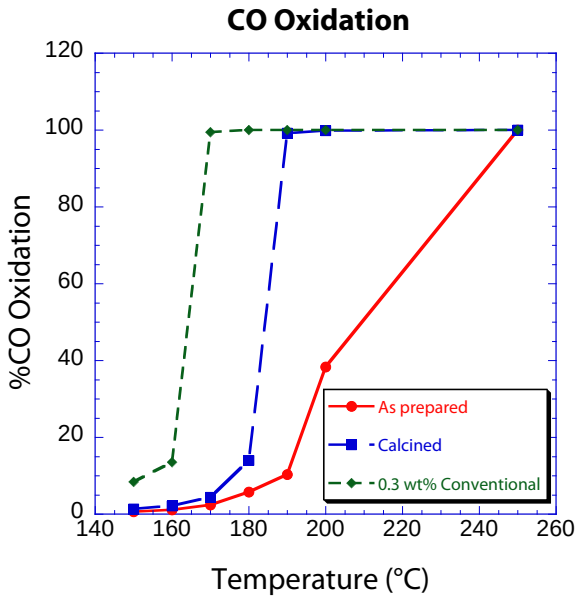

Figure 2.6: The calcined Pd/Al_2O_3 sample (■) achieves full conversion at 180 °C whereas the as-prepared Pd/Al_2O_3 sample (●) requires a temperature of 250 °C to achieve the same conversion. The 0.3 wt % Pd/Al_2O_3 sample (♦) performs better than either.

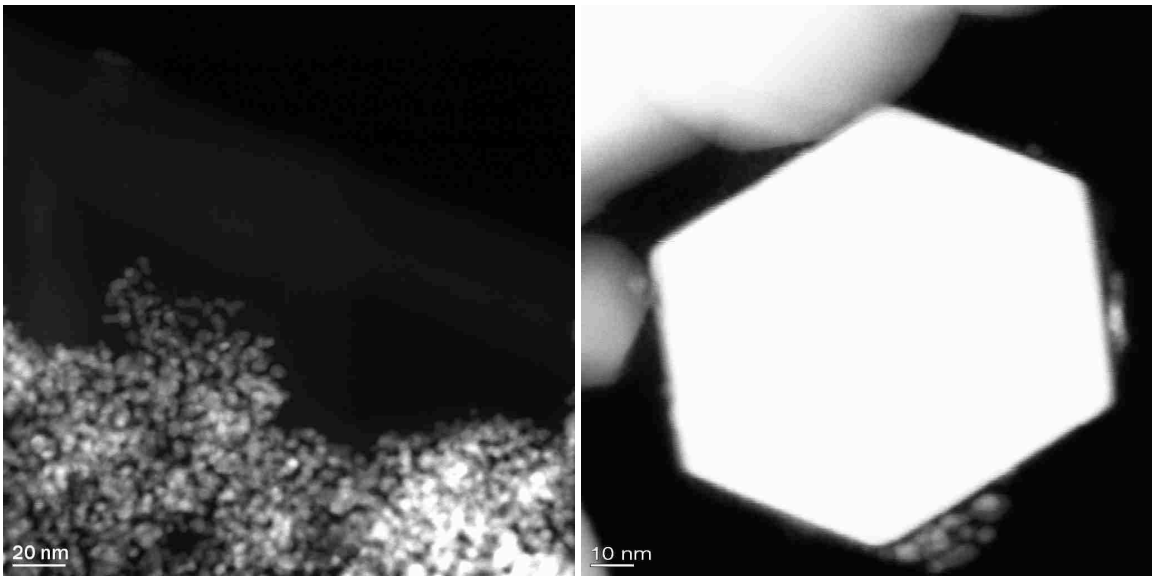

(a) (b)

Figure 2.7: (a) STEM image of colloidal amine coated palladium nanoparticles. (b) Image of Pd nanoparticles on an undamaged ZnO crystallite.

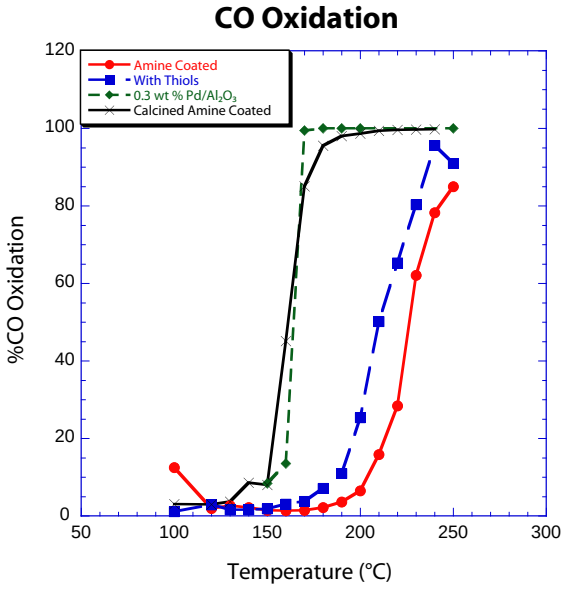

Figure 2.8: CO oxidation results of amine capped and thiol capped Pd/ZnO samples. ●=amine capped particles, ■=thiol substituted particles, ♦=0.3 wt% conventional sample, X=calcined amine coated particles.

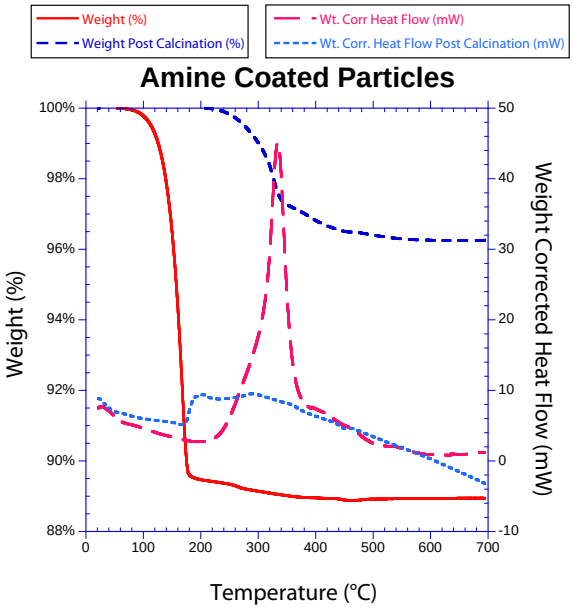

Figure 2.9: TGA/DTA plot of as-prepared and calcined Pd/ZnO samples in air. The solid line indicates the % weight loss of the as-prepared sample and the large dashed line indicates the corresponding heat flow curve. The medium dotted line shows the calcined % weight loss and the small dotted line indicates the corresponding heat flow curve.

Chapter 3

Synthesis of High Surface Area ZnO$(0001)/(000\bar{1})$ Powders

3.1 Introduction

Zinc oxide (ZnO) is an important component of supported catalysts such as those for methanol synthesis [33] and steam reforming [4]. Karim et al. [5] have suggested that faceted ZnO powders play an important role in the activity of Pd/ZnO steam reforming catalysts. Of these facets, the polar (0001)-Zn and $(000\bar{1})$-O surfaces are considered [24, 34–36] the most active ZnO surfaces and are reportedly responsible for the entirety of methanol decomposition activity in a prepared catalyst [34]. Vohs and Barteau [36] have argued that the geometry of the (0001)-Zn surface allows for the exposure of active ion pair sites, while the oxygen terminated surface completely obscures those sites. In practical use, such a geometry is difficult to produce as commercially available powders consist of prisms that do not exhibit pronounced (0001) and $(000\bar{1})$ surfaces. These prisms primarily expose non-polar $(10\bar{1}0)$ and $(11\bar{2}0)$ facets with the only polar facets at the end caps as a result of the unbalanced Zn^{2+} or O^{2-} terminated faces. A typically synthesized ZnO

powder possesses an aspect ratio of 6, where the length of the prism along the [0001] direction is compared to the thickness of the prism in a direction perpendicular to the [0001]. This morphology implies that the majority of the exposed surface of a typical ZnO powder is inactive [37]. To improve the activity, ZnO supports with lower aspect ratios exposing more polar facets are desired.

Polar surfaces are typically prepared by polishing single-crystal wafers [23, 24, 36, 38] or grown by chemical vapor transport [39]. While the exposed plane is well-controlled, these wafers are limited by very small surface areas (tens of square millimeters) and therefore very few active sites are available. To minimize ambient contamination on these limited active sites, catalytic tests on single crystal wafers are conducted under ultrahigh vacuum (UHV) conditions which lend themselves to single turnover experiments. The temperature programmed desorption experiments conducted by Hyman et al. [24] demonstrated that CO was more weakly bound to the Pd/ZnO (0001) surface than to Pd/ZnO $(10\bar{1}0)$ and that the production of CO by MeOH decomposition was likewise greater on Pd/ZnO (0001). The authors suggested that this could be due to more facile PdZn alloy formation on the ZnO(0001) surface rather than the $(10\bar{1}0)$ surface. Such studies offer useful mechanistic insights into the behavior of catalysts, but these samples do not lend themselves to steady state reactivity measurements. Therefore, a high surface area ZnO(0001) powder is needed to take advantage of the molecular level insights into catalytic behavior provided by these surface science studies.

Many techniques exist to synthesize highly faceted ZnO powders, but the platelet surface area is low $(< 15\frac{m^2}{g})$ [40, 41] and thermal stability has not been demonstrated. Some examples of successful routes to powders exposing the (0001) plane include the research efforts of Xu et al. [42] when they prepared ZnO (0001) platelets from a vapor phase transport technique. While this was effective to produce ZnO (0001), it was not easily scalable to appropriately evaluate the catalytic behavior. Wang et al. [43] have reported an electrodeposition method for the production of ZnO (0001) films on ITO glass, but these

tended to pit upon annealing. Such behavior is not unexpected as work by Staemmler et al. [44] has suggested that the (0001) and $(000\bar{1})$ surfaces reconstruct or balance the charge via hydrogenation of the surface.

Charge balance by ligands in solution is an alternate approach to stabilize the polar facets and solution techniques are amenable to large scale synthesis. Of the solution routes available, Yu et al. [45] have demonstrated a technique wherein a range of concentrations of zinc acetate [$\mathrm{Zn(CH_3COO)_2 \cdot H_2O}$, noted as $\mathrm{Zn(OAc)_2}$] and hexamethylenetetramine [$\mathrm{C_6H_{12}N_4}$, termed HMT] produced nanorods or prisms. The prism morphology was improved upon by Wang et al. [46], who produced highly faceted powders composed of low aspect ratio (0.33) (0001) plates using a mixture of water and ethanol as the solvent. A different technique by Tian et al. [47] used a sodium citrate [$\mathrm{HOC(COONa)(CH_2COONa)_2 \cdot 2H_2O}$, denoted as $\mathrm{Na_3Cit}$] solution at room temperature to produce powders with (0001) facet exposure. The amount of $\mathrm{Na_3Cit}$ used was very small in comparison to the amount of ZnO precursor, which suggested that the $\mathrm{Na_3Cit}$ was a very aggressive capping agent and only required in small amounts. While these studies did not report the surface area, it is clear from the size of the prisms presented that the area was minimal (on the order of a few square microns).

This report details the preparation of high surface area (75 $\mathrm{m^2/g}$) ZnO(0001) powders capped with $\mathrm{Na_3Cit}$ in the presence of HMT as a buffering agent. Commercial ZnO powders have surface areas of a few square meters per gram, but they do not expose the polar plane. Hence this work represents a significant improvement in the surface area of ZnO powders that predominately expose the polar plane.

3.2 Experimental

All chemicals used were ACS reagent grade obtained from Sigma-Aldrich. ZnO platelets were prepared by mixing 3.3 g (15 mmol) $Zn(OAc)_2$ with 2.1 g (15 mmol) HMT and either 1 mg (0.0034 mmol), 10 mg (0.034 mmol) or 100 mg (0.34 mmol) of Na_3Cit in 30 mL of distilled water in a three neck round bottom flask fitted with a reflux condenser open to the atmosphere on the benchtop. Prepared samples are described as ZnO-Na_3Cit-1, -10 or -100 throughout this manuscript. An additional batch without Na_3Cit was prepared using otherwise similar conditions and is referred to as ZnO-HMT. The solution was stirred for 5 min or until all reagents were completely dissolved and then heated to reflux temperature ($\sim$90 °C) for 5 h. After cooling, the resultant precipitate was separated from the mother liquor by centrifugation and rinsed with $\sim$50 mL EtOH. The powder was allowed to air dry prior to characterization. Platelet shape was analyzed using images collected in a scanning electron microscope (SEM, Hitachi S5200) operated at 2 kV accelerating voltage. Transmission electron micrographs were acquired on a JEOL 2010F field emission gun transmission electron microscope (TEM) operated at 200 kV. Selected area diffractograms (SAED) were likewise collected on the JEOL 2010F using a Gatan ES500W camera. Powder X-ray diffractograms (XRD) were collected on a Scintag Pad V diffractometer with DataScan 4 software from MDI, Inc. for system automation and data collection. Cu-K_α radiation (40 kV, 35 mA) was used with a Bicron Scintillation detector with a pyrolitic graphite curved crystal monochromator. The scan settings used a 0.02 step size and a 10 second dwell time. Whole-pattern Reitveld refinement [48] was conducted on the collected patterns using GSAS [49] and EXPGUI [50]. Reference values for the ZnO profile were obtained from the American Mineralogist Crystal Structure Database [1]. Fourier-transform infrared spectroscopy (FT-IR) was conducted using an attenuated total reflectance (ATR, Smart Orbit) attachment on a Nicolet 6700 using 256 scans at a resolution of 2 cm^{-1}. Thermogravimetric analysis and differential thermal analysis (TGA/DTA) were performed on a TA SQT Q600 under flowing N_2 at a ramp rate of

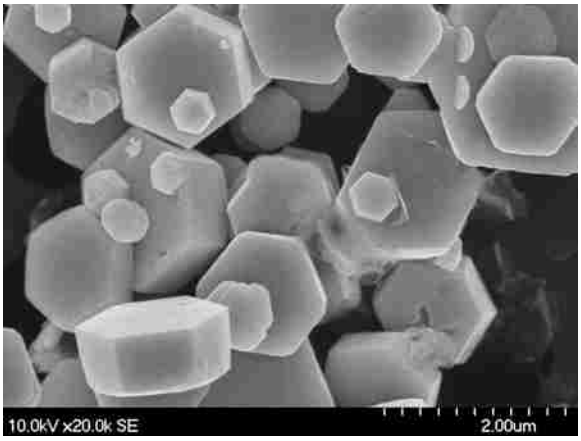

Figure 3.1: Hexagonal prisms of the ZnO-HMT sample did not display any substantial preference towards the exposure of the (0001) facet.

20 °C per minute to 700 °C. The surface area was determined by the Brunauer, Emmet and Teller method [9] with a Micromeretics Gemini 2360 after outgassing at 120 °C in flowing N_2 overnight. Additional pretreatments were conducted at 250 and 340 °C in flowing N_2 to evaluate the stability of the plates at and above a commonly used temperature for methanol steam reforming [5].

3.3 Results and discussion

3.3.1 Role of HMT on ZnO Morphology

Following the synthetic procedure outlined in Section 5.1, ZnO powders were synthesized in the presence of HMT to produce ZnO-HMT regular hexagonal prisms, as shown in Figure 3.1. The exposed area of the polar (0001)/$(000\bar{1})$ planes was comparable to that of the $(10\bar{1}0)$ facet as determined by a visual inspection of the SEM images. The surface area was estimated at 1 m^2/g using the average crystallite size found by inspection of the SEM images. BET analysis (Table 3.1) was unable to provide a reliable measurement as the

value was below the minimum range of the instrument and could not be accurately determined. Since the surface area was undetectable at the lowest (120 °C) outgas temperature, further pretreatment was not undertaken.

3.3.2 Role of Na_3Cit on ZnO Morphology

ZnO powders were also synthesized in the presence of HMT with 1, 10 or 100 mg of Na_3Cit to produce ZnO-Na_3Cit-1, -10 and -100 platelets. These samples had a plate-like morphology, and the plates became thinner with increasing Na_3Cit content. The dependence upon Na_3Cit concentration can be seen in Figure 3.2, where the lowest concentration (ZnO-Na_3Cit-1, Figure 3.2a) produced a combination of thin plates and prisms. Increasing the concentration further (ZnO-Na_3Cit-10, Figure 3.2b and 3.2c) yielded plates which tended to stack regularly in the [0001] direction like a ream of paper, while the ZnO-Cit-100 plates were much more disordered (Figure 3.2d).

This was suspected to be a result of the differing degrees of surface charge compensated for by the capping agent. TGA and FTIR analysis of the Na_3Cit plates revealed that the surfaces were capped in Na_3Cit with no detectable HMT present. TGA/ DTA analysis (Figure 3.3) indicated that the HMT volatilized completely between 200 and 300 °C. In contrast, both the Na_3Cit and the ZnO-Na_3Cit-100 exhibited similar peaks near 150 and 315 °C. The close match suggests that the ZnO-Na_3Cit-100 was coated with Na_3Cit, thereby causing similar peaks to occur during TGA/DTA analysis. In addition, FT-IR spectroscopy (Figure 5.7) confirmed the presence of the Na_3Cit on the prepared powder. Combined, these results suggested that the Na_3Cit was strongly bound to the ZnO surface with no evidence to indicate the presence of HMT. This behavior suggested that the HMT acted as a buffer in solution, while the Na_3Cit was actively bound to the ionic surfaces, consistent with reports in the literature [45, 51]. Therefore the Na_3Cit acted as a charge stabilizer and was observed in the product, while the HMT was not retained on the sur-

face. As a result, the platelets synthesized with Na_3Cit and HMT had a more thoroughly charge compensated surface and were able to grow much thinner (Figure **??**c and d) than the prisms produced with HMT alone (Figure **??**a).

3.3.3 Characterization of ZnO Platelets

The above data indicated the Na_3Cit concentration had a strong influence on the stacking of the platelets as well as the morphology. In order to determine the exposed facets, we studied the powders via XRD and electron diffraction in the TEM. Reitveld analysis of the XRD pattern (Figure 4.2) indicated a substantial anisotropic broadening of the (0002) peak, which is a higher order reflection of the forbidden (0001) reflection. This peak broadening also substantially reduced the (0002) peak height. An additional set of peaks was identified as $\{[Zn_2(C_2H_2N_3O)(OH)_3] \cdot 2H_2O_n\}$ based upon a match to a similar copper compound in the ICSD database (card # 260453, [52]). This phase was found to comprise $\sim$ 20 wt% of the crystalline fraction of the sample by Reitveld analysis, which suggested that the material existed as a bulk contaminant in the powder rather than a monolayer adsorbed on the surface and did not contribute to the layered structure. The average plate thickness was found by XRD to be 25 nm, which is at the high end of the range (10-25 nm) measured from SEM images (Figure 3.2c). Since the XRD average determined by the Scherrer equation is a volume average, the calculated value was weighted towards thicker plates. SEM measurements were also imprecise due to the error induced by measuring images of a tilted surface. The platelet thickness calculated from the BET surface area, as described in Equation 3.1, (derivation in Appendix B) was 7 nm.

$$c = \frac{2}{BET \times \rho_{ZnO}} \tag{3.1}$$

While it was not possible to determine an exact aspect ratio due to the difficulty in measuring the width of the platelets, we estimate it to be on the order of 0.01 when considering the stacks of micron-sized platelets with 7 nm thickness.

In contrast, the ZnO-Na_3Cit-100 sample showed randomly oriented platelets which did not form layered structures. Inspection of individual ZnO-Na_3Cit-100 platelets via selected area electron diffraction (Figure 3.6) confirmed exposure of the (0001) facet.

The stacking of platelets in each sample strongly influenced the surface area and thermal stability. The surface area measurements (Table 3.1) for each sample correlated to the concentration of Na_3Cit in the synthesis step. The ZnO-Na_3Cit-10 sample demonstrated a surface area of 50 m^2 per gram, and the surface area of the ZnO-Na_3Cit-100 sample was nearly doubled (96 m^2/g). The weight loss (by TGA, Figure 3.8) of the ZnO-Na_3Cit-100 sample was double that of the ZnO-Na_3Cit-10.

3.3.4 Thermal Stability of ZnO Plates

Since these platelets were were developed as novel supports for steam reforming catalysts, the thermal stability was tested by heating the samples to 250 °C. When heated, the surface area of the ZnO-Na_3Cit-10 decreased, which is believed to be due to the stacked orientation of the platelets. The layered structure observed by SEM (Figure 3.2c) placed each crystallite in close proximity to a neighboring platelet. Upon heating, the energetically unstable $(0001)/(000\bar{1})$ facets were in close contact and fused easily (Figure **??**a). Similar stacking behavior has been reported by Cao et al. [53] when growing ZnO platelets on Si substrates. In contrast, the ZnO-Na_3Cit-100 sample was very disordered, and thus

Table 3.1: BET surface area of prepared ZnO powders.

Sample	Surface Area $(\frac{m^2}{g})$		
	120 °C	250 °C	340 °C
ZnO-HMT	< 1		
ZnO-Na_3Cit-10	50	< 1	
ZnO-Na_3Cit-100	96	75	48

a greater void space existed between each platelet (Figure 3.9b). Since the polar facets were not in immediate contact, the platelets could not condense like the ZnO-Na_3Cit-10 sample. As a result, the sample retained a high surface area (75 m^2/g) when heated to methanol steam reforming temperatures. The plates developed a mottled texture, as seen in Figure 3.9. TEM images show that the plate had broken into individual crystallites, but these retained their orientation as seen from electron diffraction patterns in Figure 3.7. These small crystallites also exhibited (0001) faces as shown by SAED (Figure 3.7, inset). Reitveld analysis indicated that the average thickness after heating to 250 °C was 11 nm, which along with the BET (5 nm) and SEM measurements (20-30 nm) demonstrated that the platelets could survive moderate heat treatment. As noted previously, determination of plate thickness via SEM was difficult since it was not easy to find plates that were sitting edge-on. Further pretreatment at 340 °C caused additional loss in surface area.

The presence of Na_3Cit was found to have no effect on the platelet thermal stability. FTIR scans (Figure 3.10) of post-treated ZnO-Na_3Cit-100 samples indicated that some Na_3Cit remained on the surface at 340 °C and thus removal of the ligand was not considered to be a factor in the break up of the plates into smaller crystallites. As such, the ligand is not necessary to maintain platelet stability and can be removed to avoid interference with subsequent catalytic activity.

3.4 Conclusion

We have demonstrated a simple solution-based synthetic technique that produced high surface area ZnO platelets with (0001) faces. The growth mechanisms via synthesis using the amine-based competing ion technique and citrate based poisoning method show that the competing ion effect provided only a weak interaction, while the poisoning method was a far more robust process. FTIR and TGA/DTA results indicated the HMT ligand was not bound to the ZnO after synthesis, thereby implying that it provided a weak interaction

in solution to moderately favor (0001) facet growth. In contrast, the presence of Na_3Cit produced a much thinner platelet. The thermal stability of the sample was found to be dependent on the relative proximity of the individual platelets. Stacked platelets tended to condense upon removal of the citrate ligand by heat treatment whereas plates that were separated from each other retained a high surface after thermal treatment. The stacked platelets lost surface area when they sintered to form thicker crystallites. In contrast, the disordered platelets did not have the nearest neighbor contact that the stacked platelets did, and thus remained distinct. Many of the deformed plates continued to expose the (0001) facet, which suggests that moderate heat treatments were not detrimental to the overall exposed facet. Studies to investigate the activity of supported catalysts using these polar powders are underway.

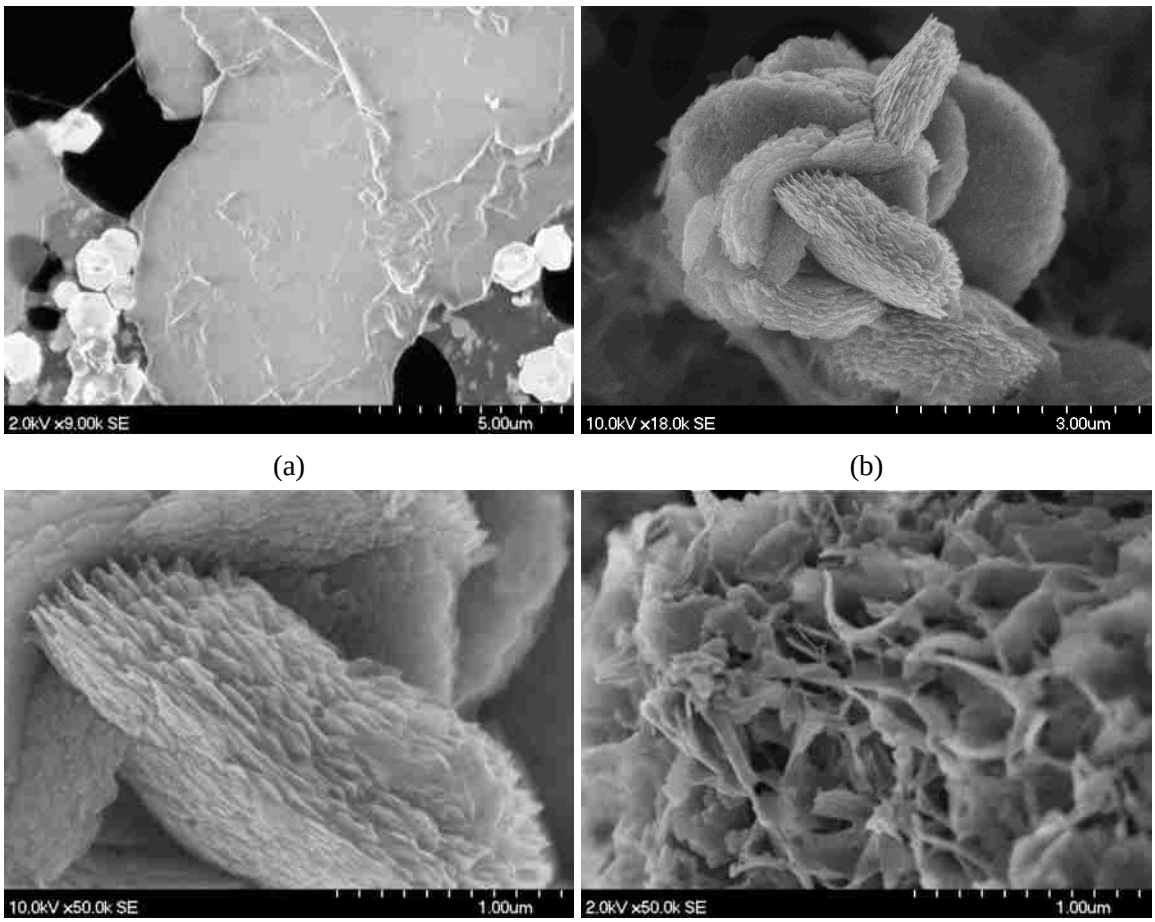

Figure 3.2: Samples synthesized with a range of Na_3Cit from 1 mg (ZnO-Na_3Cit-1, a) to 10 mg (ZnO-Na_3Cit-10 plates, b and higher magnification, c) and 100 mg (ZnO-Na_3Cit-100, d) demonstrated formation of increasingly thin platelets.

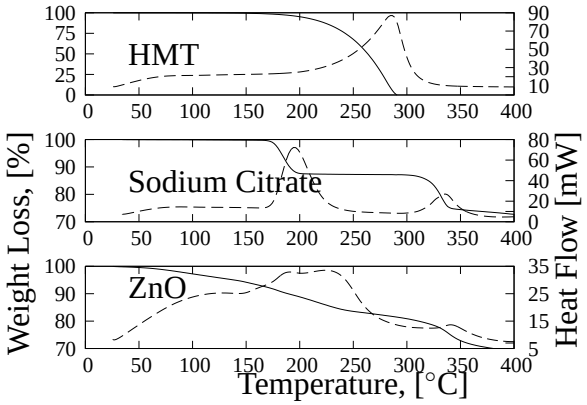

Figure 3.3: TGA-DTA analysis showing thermal stability of pure HMT (top), Na_3Cit (middle) and ZnO-Na_3Cit-100 (bottom) to 400 °C.

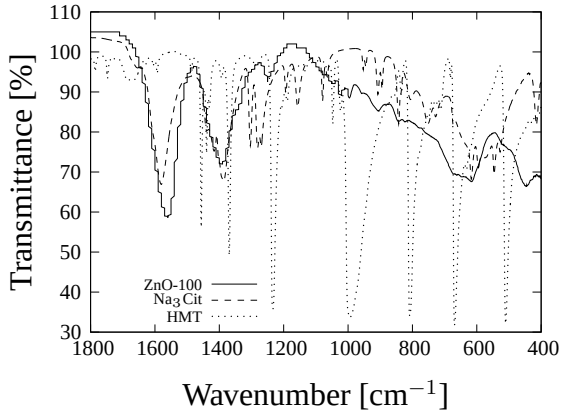

Figure 3.4: FTIR spectra showing similarity between the ZnO-Na_3Cit-100 and pure solid Na_3Cit, in contrast to the pure solid HMT.

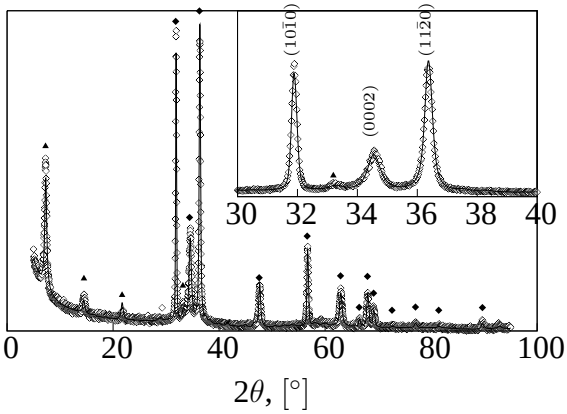

Figure 3.5: XRD diffraction pattern showing ZnO-Na_3Cit-10 (Open diamonds) with corresponding Reitveld refinement curve shown as a solid line. Major peaks corresponding to ZnO (Wurtzite, [1]) are noted by filled diamonds. The other set of peaks (filled triangles) fit the pattern for an organometallic phase (ICSD card # 260453).

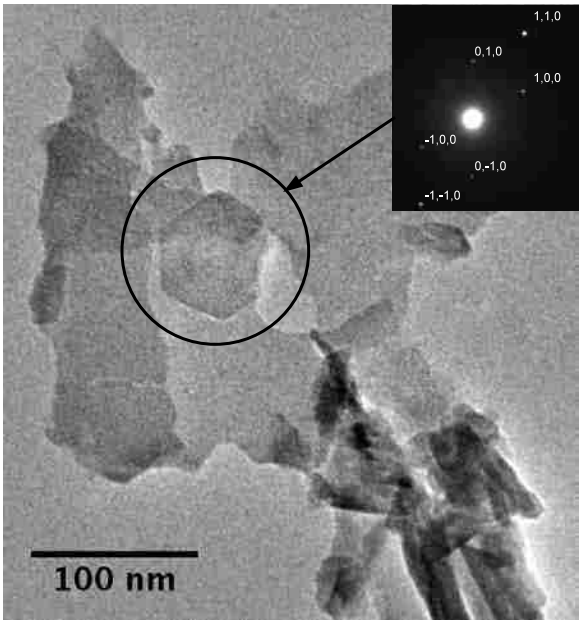

Figure 3.6: SAED (inset) of an individual platelet of the ZnO-Na_3Cit-100 sample after heating to 150 °C exposing the (0001) facet. Images processed with ImageJ [6].

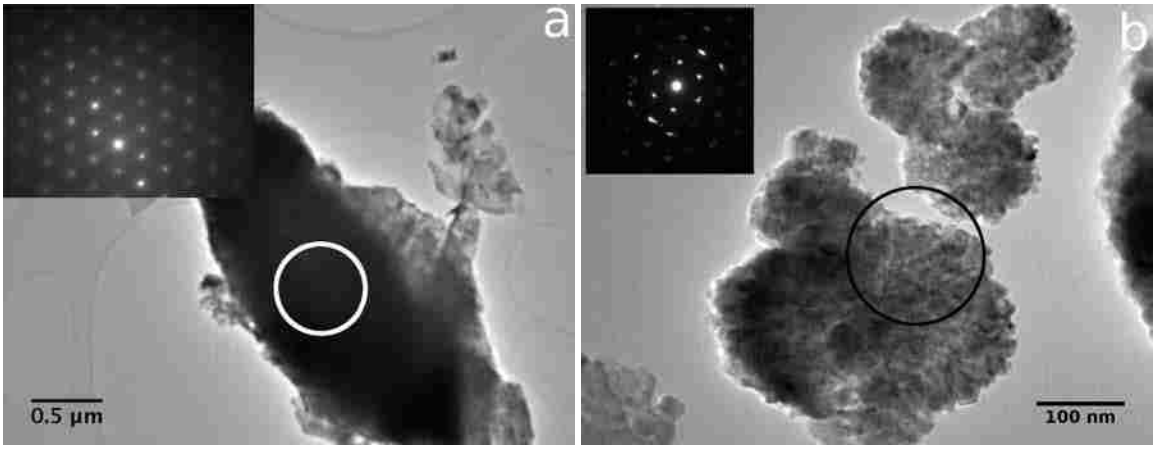

(a) (b)

Figure 3.7: Both the ZnO-Na_3Cit-10 (a) and ZnO-Na_3Cit-100 (b) samples maintained the (0001) facet upon heating to 250 °C, as shown by the SAED images (insets).

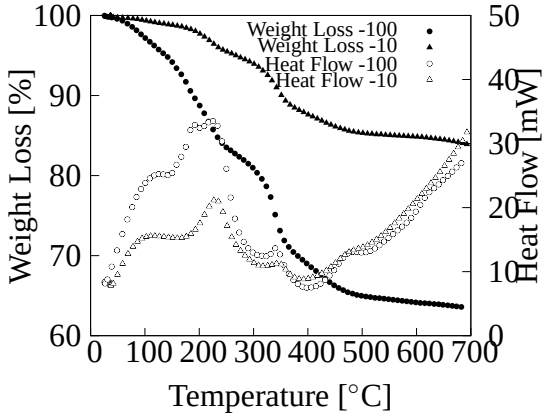

Figure 3.8: TGA/DTA analysis of ZnO-Na_3Cit-10 and -100 samples show a significant difference in weight loss due to ligand removal.

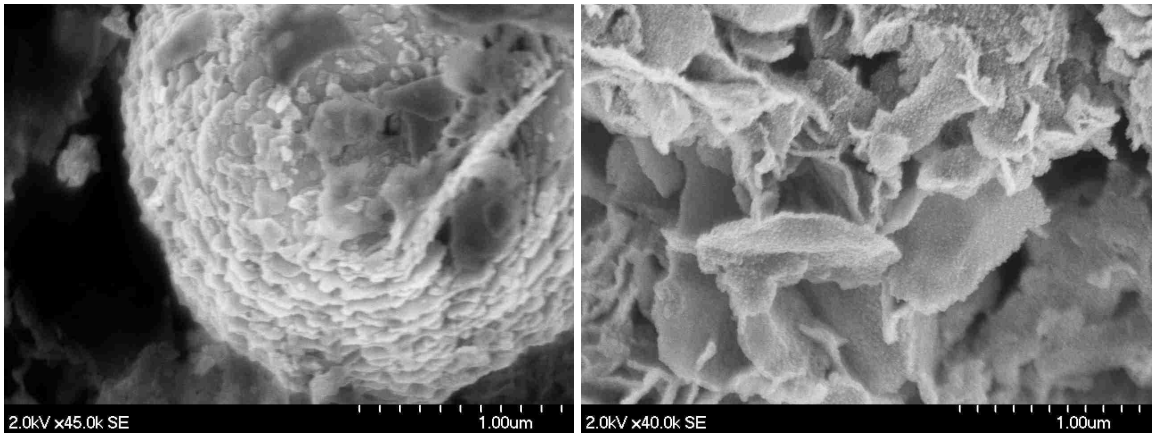

(a) (b)

Figure 3.9: After heating to 250 °C, the ZnO-Na_3Cit-10 (a) and ZnO-Na_3Cit-100 (b) plates remained intact but showed signs of thermal damage.

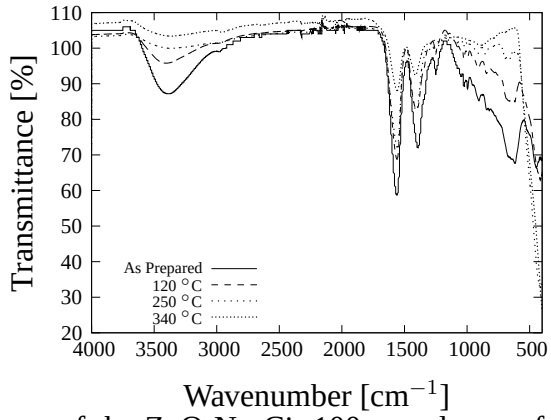

Figure 3.10: FTIR spectra of the ZnO-Na_3Cit-100 sample as a function of pretreatment show that the sample retained some Na_3Cit at each pretreatment temperature.

Chapter 4

Acetylene Hydrogenation Activity of Monodispersed Pd Nanoparticles by Photoreduction in Methanol

4.1 Introduction

Supported Pd nanoparticles constitute the active phase in catalysts used for energy conversion, chemical synthesis and pollution abatement. To achieve the highest selectivity and reactivity, it is desirable to have well dispersed nanoparticles (NPs) that have identical properties and distribution of active sites [54]. Unfortunately, conventional synthesis routes do *not* provide the requisite degree of control, since they start from Pd salts which are first deposited on a support by impregnation or precipitation. Reduction is achieved by high temperature treatments involving calcination and H_2 reduction, or chemical reduction by sodium borohydride [55]. The resulting broad distribution of particle size, shape, and composition is detrimental to catalyst performance. Hence, there has been considerable interest in developing colloidal routes to synthesize well defined nanoparticles that could

be used to prepare heterogeneous catalysts [56–58]. Typically, solution routes require various reducing agents such as hydrazine [59], alkaline borohydrides, [60] or amine groups [61] where the particles are protected by polymer groups, surfactants or ligands to prevent agglomeration and growth [60, 62].

Polymer protecting agents such as poly(vinyl pyrrolidone) (PVP) and polyvinyl alcohol (PVA) allow preparation of metal colloids that can be stable for months with reasonable control over size as well as shape [63–67]. The synthesis involves addition of polymer to the metal salt followed by chemical or thermal reduction to produce a stable black suspension of Pd^0 particles. These polymer-capped nanoparticles have been shown to be capable of adsorbing probe molecules (i.e., CO) [65] and to be active in a variety of liquid-phase reactions, such as olefin hydrogenation [56] as well as alcohol oxidation [68]. However, when the polymer capped nanoparticles are deposited on a support for gas-phase reactions, the capping agent must be removed to achieve catalytic activity [54, 69, 70]. The high temperature oxidation and reduction treatments used can lead to particle growth and loss of monodispersity. Therefore, there is a need to develop novel routes that can provide metal nanoparticles without protective polymers or capping ligands.

In solvothermal synthesis, precursors such as palladium chloride, or palladium (bis acetyl acetonate) are added to high boiling solvents such as bromobenzene, toluene or methyl isobutyl ketone in the presence of a surfactant to achieve reduction to the metal [71]. A more easily reduced precursor, such as palladium acetate (noted as $Pd(OAc)_2$) allows for colloidal synthesis at lower temperature using simple alcohols as reducing agents [57, 58, 72]. However, literature reports that utilize methanol (MeOH) without a capping agent indicate that large aggregates will form [72]. These aggregates can reach diameters of 50 nm and are not suited for catalytic applications. The uncontrolled reduction of Pd complexes at elevated temperatures has been described in the homogeneous catalysis literature as a nuisance [73]. These studies all suggest that capping agents or ligands are essential for the synthesis of nanoparticles in solution at elevated temperatures.

Recent work by Chen et al. [74] has shown that graphene oxide can directly reduce K_2PdCl_4 to produce NPs. While this is an effective technique and yields Pd nanoparticles of about 3 nm in diameter, it is limited to reactions using graphene oxide as a support. We describe here a more general route for synthesizing nanoparticles that involves the reduction of the precursor by the solvent. In order to avoid capping agents, a mild reducing agent must be employed to limit rapid particle formation, growth, and coalescence. We have found that the room temperature reduction of $Pd(OAc)_2$ in MeOH is slow enough to produce a suspension of Pd NPs. These NPs can then be used as the metal phase of a heterogeneous catalyst without the need for thermal treatment prior to reaction. A Pd-NP/C catalyst was prepared by mixing the carbon support into the suspension of Pd NPs and evaporating the solvent. Aggregate formation was a concern, as there were no capping agents to prevent particle growth. Therefore, the nanoparticles were collected quickly before substantial aggregation could occur. As the reduction was not caused by the support, this technique is general and can be extended to other powder supports. The catalyst was active as-prepared and was found to be active and very selective for acetylene hydrogenation in the presence of excess ethylene.

4.2 Methods

4.2.1 Chemicals

All chemicals were used as received and stored under ambient conditions unless otherwise noted. Two separate containers of $Pd(OAc)_2$ were used, one stored and used in an argon-filled glovebox and the other stored and used under bench-top conditions. Anhydrous MeOH and bench-top MeOH, ethanol, 2-propanol, toluene and acetone were reagent grade and purchased from Sigma Aldrich. Vulcan XC72R was obtained from Cabot Corporation. Hydrogen, nitrogen, and a mixture of 0.5% acetylene and 35% ethylene (balance nitrogen)

were UHP grade from Matheson Trigas.

4.2.2 Synthesis

Preparation of colloidal nanoparticles

For a typical sample, Pd nanoparticles were synthesized by mixing $Pd(OAc)_2$ (5 mg) in MeOH (15 mL) in a scintillation vial and stirring for approximately 5 min with unobstructed exposure to room lighting. The vial was placed on an elevated stir plate for observation and allowed to react undisturbed for 20 min. After 20 min, a TEM grid was dipped into the vial and allowed to dry. Variations on this method were conducted with air-exposed precursors and solvents, including acetone, toluene, ethanol, and 2-propanol. The dependence upon light was evaluated by isolating a vial in an insulated container placed over a stir plate. The solution was stirred for 5 min in the dark and allowed to sit undisturbed over a 2 h period. Observations were conducted at 10 min intervals to minimize light exposure.

Preparation of supported catalyst

A supported catalyst was prepared by dissolving anhydrous $Pd(OAc)_2$ (20 mg) in anhydrous MeOH (30 mL) and stirring continuously for 10 min in a Schlenk flask under inert atmosphere. The flask was removed to ambient atmosphere and Vulcan XC72R carbon (1.0 g) was added. The slurry was mixed for an additional 10 min and subsequently attached to a rotovap, using the bath to maintain the flask at ambient temperature. The solvent was removed while the reaction continued to progress. After 30 min, the reaction was complete and the slightly damp powder was allowed to air dry prior to characterization. No additional treatments were performed prior to catalytic activity measurements. This sample will be referred throughout the manuscript as Pd-NP/C. A similar sample

was prepared under identical conditions, except toluene was used as the solvent. As this sample did not form nanoparticles in solution, it will be referred to simply as Pd/C.

4.2.3 Acetylene hydrogenation

The catalyst was granulated by pressing the dried powder under $\sim$7 metric tons with a Carver hydraulic press to produce a pellet. The pellet was ground and the powder sieved to between 106 and 250 μm using # 140 and # 60 U.S. standard testing sieves from VWR. A sample of 15 mg of powder was mixed with 400 mg SiC (350 μm average grain size, Washington Mills) as an inert to minimize temperature non-uniformity. The mixed powder was packed in a 0.25 inch quartz tube between two plugs of quartz wool. A mixture of acetylene (0.5%) and ethylene (35%) in a balance of nitrogen was passed over the powder at a flowrate of 66 mL/min. Hydrogen was passed at 1.4 mL/min to produce a 5:1 ratio of hydrogen to acetylene. Product gases were sampled at temperature intervals of 10 °C by a Varian 3800 gas chromatograph equipped with a CP-PoraBOND U column and an FID detector.

4.2.4 Characterization

FTIR (Nicolet 6700, 32 scans, 4 cm^{-1} resolution) was used to probe for the presence of hydroxyl groups on each precursor. The prepared colloids were examined by transmission electron microscopy (TEM, JEOL 2010F) operated at 200 kV in scanning (STEM) and high resolution (HRTEM) modes to determine the size and composition of the particles. X-ray diffraction (XRD, Panalytical X'Pert Pro, 45 kV 40 mA) was used as a complementary technique. An aliquot of the colloid was pipetted onto a zero-background Si wafer and allowed to dry at room temperature. As the solvent evaporated, the particles coalesced and produced a film, which was then analyzed to verify production of a metallic phase.

4.3 Results and Discussion

The initial investigation involved the reduction of $Pd(OAc)_2$ in MeOH to produce a suspension of Pd NPs (Figure 4.1). A systematic study of precursor conditions, light exposure and solvent was undertaken. In the initial study, using an air-exposed precursor and solvent, the dissolution of the red-orange $Pd(OAc)_2$ in MeOH yielded a pale yellow solution which progressively darkened to a black solution after 60 min (Figure 4.1a).

Subsequent attempts to reproduce the reaction resulted in longer reaction times (up to days) and moderate variation in particle size. Under rigorously dry conditions, the color change was found to be both faster (dark green in 20 min, black in 30 min) and reproducible. A TEM grid was dipped into the solution at 20 min and a dark field STEM image is shown in Figure 4.1b. The mean diameter of 1.5 nm (Figure 4.1d) is remarkable in view of the simplicity of the preparation. Multiple tests were performed and it was found that the size distribution was very similar in each case. The Pd particles were so small that they were very difficult to detect via HRTEM on the carbon film and could only be imaged via dark field imaging in a STEM. Our estimate of precision in size measurement is based on the probe size used for our STEM imaging, 0.2 nm. The electron diffraction pattern is very diffuse in agreement with the small size and the low loading of the Pd NPs on the carbon film.

A sample of $Pd(OAc)_2$ in MeOH that was stored in a 'black box' was found to yield no color change after 2 h. Exposure to UV light only led to a similar reaction rate as the sample under ambient light. Larger chain alcohols (ethanol and 2-propanol) produced a color change in several hours, but non-alcohol solvents, such as acetone took one week to react. TEM samples prepared from the acetone preparation revealed that large Pd aggregates had formed. These observations indicated that alcohols were effective reducing agents, as noted by Hirai et al. [56]. Exposing a solution of $Pd(OAc)_2$ in anhydrous MeOH to ambient room light yielded optimal results. Following these reaction conditions, a cat-

alyst was prepared by mixing Vulcan XC72R carbon powder into the solution after 10 min of reaction. The suspension was stirred for an additional 10 min followed by drying *in vacuo* at room temperature. The powder was analyzed by TEM (Figure 4.1c) and the nanoparticles were found to be similar in size to those noted in the previous synthesis (Figure 4.1b). The Pd NPs in this colloid were confirmed to be metallic based on the XRD analysis of the dried colloid, which yielded the expected fcc Pd pattern. An XRD sample of the colloid was prepared by pipetting an aliquot of the suspension on a silicon wafer and allowing it to dry prior to analysis. As there were no surfactants, the metal dried to a thin film which produced peaks corresponding to metallic Pd. These peaks were indexed to ICCD card 89-4897 (fcc Pd) while the precursor did not display any metallic phase, shown in Figure 4.2. The Pd-NP/C powder did not feature any prominent Pd peaks, which was expected due to the small crystallite size and low weight loading. EDS indicated that $\sim$1 wt % loadings had been achieved.

Each as-prepared catalyst was subsequently tested for acetylene hydrogenation with a 70:1 mixture of ethylene:acetylene in a packed bed reactor. Interestingly, the Pd-NP/C catalyst was found to be selective (Eq. (4.1)) toward ethylene production at high conversion (Figure 4.4) and active (Figure 4.3, $E_a = 49\frac{kJ}{mol}$) without any pretreatment. Four subsequent trials showed similar results (Figs. 4.3 and 4.4, Table 4.1). The catalyst was therefore active without pretreatment, and stable over the time interval studied. Pd is a well-known hydrogenation catalyst and is commonly diluted with other metals when used for selective hydrogenation of acetylene [7, 75]. The Pd-NP/C catalyst yielded selectivity equivalent to the performance of the best catalyst reported in the literature, Pd_3Ga_7 [76]. The Pd/C catalyst exhibited an activation process where subsequent trials showed much greater activity in comparison to the initial experiment (Figure 4.3, activation energies tabulated in Table 4.1). Each trial was significantly less selective (Figure 4.4) at 100% conversion of acetylene. Both catalysts demonstrated activation energies within the reported values of 40-50 $\frac{kJ}{mol}$ [7, 77], except for trial 1 of Pd/C.

Table 4.1: Comparison of the performance of the Pd catalysts using selectivity as defined by Eq. (4.2).

Sample	$E_a \frac{kJ}{mol}$	Conversion (%)	Selectivity (%)
Pd-NP/C			
Trial 1	49	76	+72
Trial 2	47	100	+52
Trial 3	47	100	+43
Trial 4	45	98	+44
Trial 5	42	96	+40
Pd/C			
Trial 1	98	100	-105
Trial 2	37	100	-224
Trial 3	39	100	-203
Trial 4	42	100	-76
Trial 5	42	100	-89
Pd_3Ga_7 [76]		99	+71
Pd/Al_2O_3 [76]		43	+17

Selectivity was defined as the moles of ethylene generated per mole of acetylene consumed, as shown in Eq. (4.1). In the notation used, f denotes feed and e denotes effluent.

$$Selectivity = \frac{C_e^{Ethylene} - C_f^{Ethylene}}{C_f^{Acetylene} - C_e^{Acetylene}} \times 100\% \tag{4.1}$$

The change $\Delta C^{Ethylene}$ is caused by production of ethylene from acetylene hydrogenation and consumption to ethane. Therefore, a positive selectivity indicates a net gain in ethylene compared to the feed. A negative value represents a loss due to consumption of the feed ethylene in addition to total hydrogenation of acetylene to ethane. This definition of selectivity differs from an equation used by Osswald et al. [76] who consider the change in ethylene concentration $\Delta C^{Ethylene}$ to be unreliable, and use equation (4.2) instead.

$$Selectivity = \frac{C_f^{Acetylene} - C_e^{Acetylene}}{C_f^{Acetylene} - C_e^{Acetylene} + C_e^{Ethane} + 2C_e^{other}} \tag{4.2}$$

This alternate definition of selectivity was used to compare our results with those of Osswald et al. [76]. The term C_e^{other} was omitted as there was no green oil detected in the present work. The comparison (Table 4.1) showed that the performance of Pd-NP/C was

comparable to Pd_3Ga_7 and significantly better than Pd/Al_2O_3. Another study by Studt et al. [7] reported data in terms of ethane production, but using $\sim$ 26x lower ethylene content in the feed. The ethane content of the present work is shown in Figure 4.5 as moles of ethane in the effluent per mole of ethylene in the feed to compare the data on the same basis. Using this approach, it can be seen that the Pd-NP/C catalyst prepared in this work showed higher selectivity than the $Pd/MgAl_2O_4$ reported by Studt et al. [7]. The high selectivity of Pd-NP/C could be a result of the size of the nanoparticles, the carbon support, or possible carbonaceous species derived from the catalyst precursor and is under investigation. As the nanoparticles formed in solution, any carbonaceous impurities present could have deposited onto the particle as the sample dried. The presence of carbonaceous layers may have resulted in improved selectivity, as reported previously in the literature [78]. One possible cause has been attributed to formation of a carbonaceous species due to the differences between pulse and flow operation. Under standard reaction conditions, the reactant gasses were allowed to flow through the reactor continuously, and sampled by the GC. In pulsed operation, the gas flow was turned off while the sample was analyzed, then turned on two minutes before the subsequent sample was collected. Evidence for a carbonaceous layer can be seen in the curvature of the selectivity plots (Figure 4.4). The selectivity can be divided into three different regimes; single turnover, kinetic limited and diffusion limited. At low temperatures, the hydrogenation is a single turnover event, and results in 100 % selectivity. Some carbonaceous deposits form, resulting in positive selectivity at higher temperatures. These deposits are removed during the course of reaction, resulting in peak selectivity between the kinetic and diffusion regime. Above this peak, full hydrogenation begins to take place. When the test was conducted in pulse mode, the carbonaceous deposits did not form, as there was no reactant stream to continuously replenish the carbon.

4.4 Conclusions

In summary, a simple route to a highly active and selective Pd-NP/C heterogeneous hydrogenation catalyst has been developed. The Pd^0 NPs were synthesized from the ambient temperature reduction of $Pd(OAc)_2$ in MeOH under anhydrous conditions. The inclusion of Vulcan XC72R during the synthesis led to isolation of the active catalyst that did not require any additional treatment. This technique alleviated the need to pre-treat the catalyst, and provided a substantial improvement in selectivity. Additional work on understanding the performance of these catalysts, and Pd NPs on other supports, is being undertaken to explore the broader utility of this simple route to Pd^0 nanoparticles.

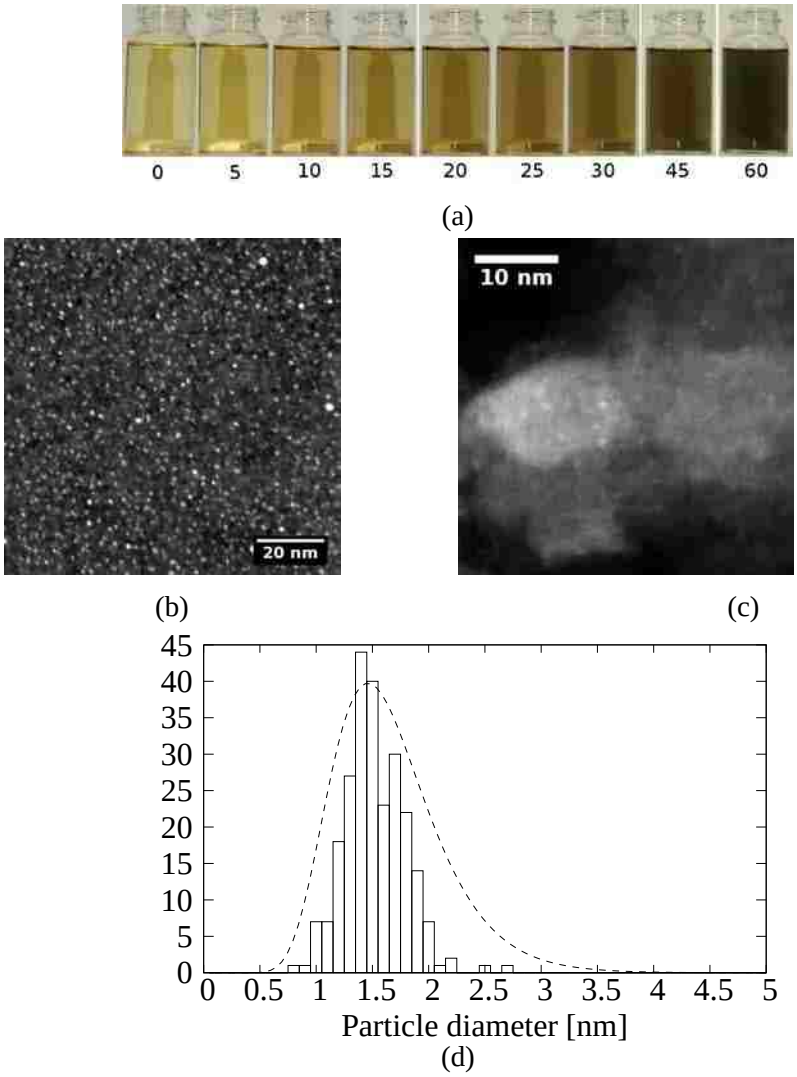

Figure 4.1: (a) Time-progression (in min) of formation of air-exposed Pd NP solution in MeOH, (b) STEM image of colloid deposited on carbon film, (c) Pd-NP/C before reaction, (d) particle size distribution of Pd NP from MeOH.

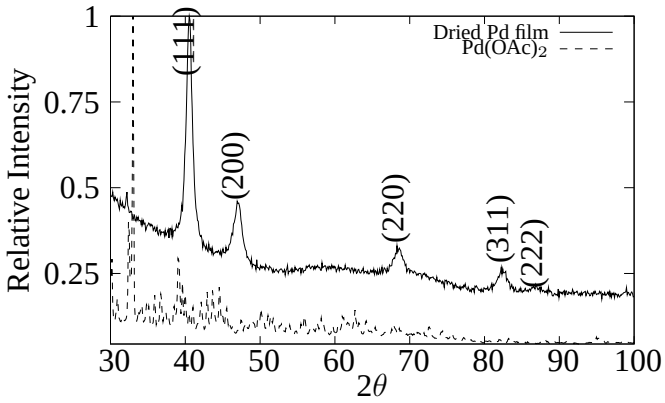

Figure 4.2: XRD pattern of dried film colloid on a Si substrate matches Pd. The precursor, $Pd(OAc)_2$, shows a very different pattern, indicating that the organic precursor was reduced to fcc metal.

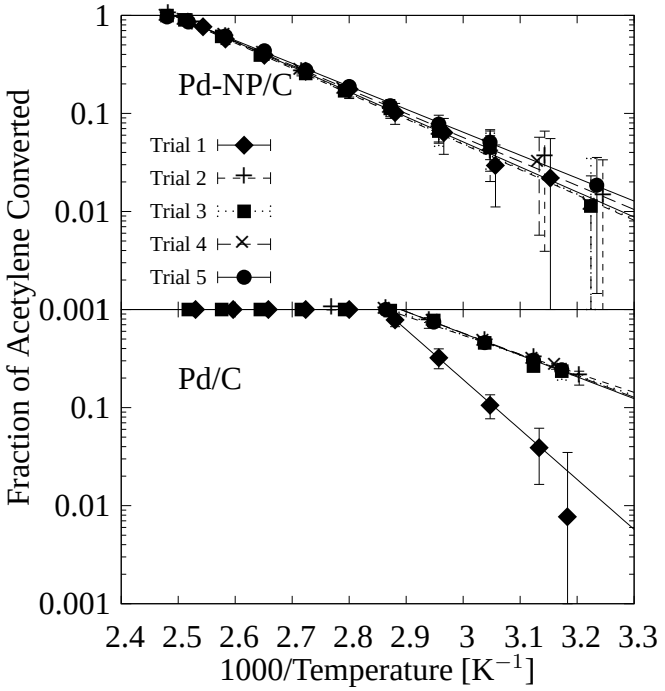

Figure 4.3: Graph of fraction of acetylene generated over the reaction temperature range for Pd-NP/C (top graph) and Pd/C (bottom graph). Five repeat trials are shown for each catalyst.

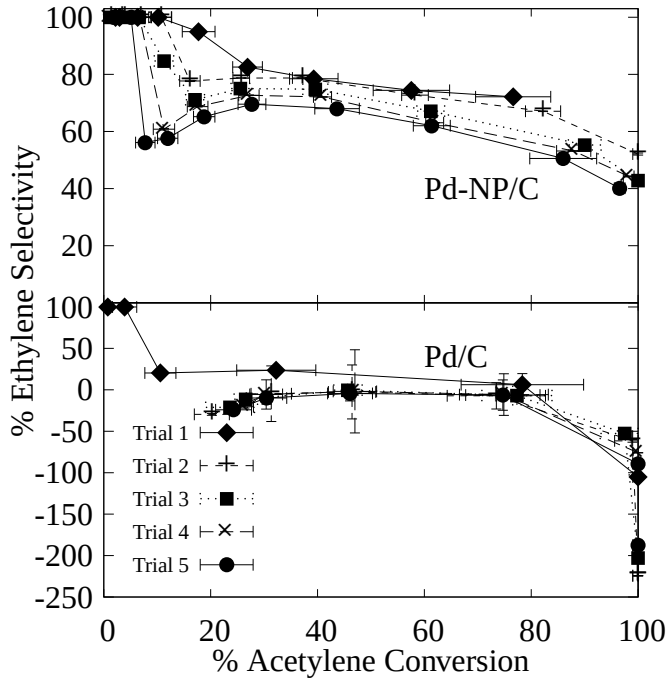

Figure 4.4: Graph of ethylene selectivity showing excess C_2H_4 production as positive selectivity (consumption as negative values). As in Figure 4.3, five repeat trials are shown for both Pd-NP/C (top) and Pd/C (bottom). Lines are added as a visual aid.

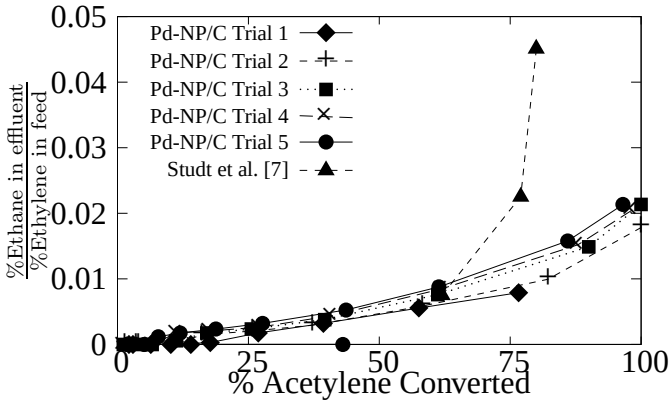

Figure 4.5: Ethane content of outlet gas in the present work normalized to inlet ethylene for comparison to the literature [7]. Lines added as a visual aid.

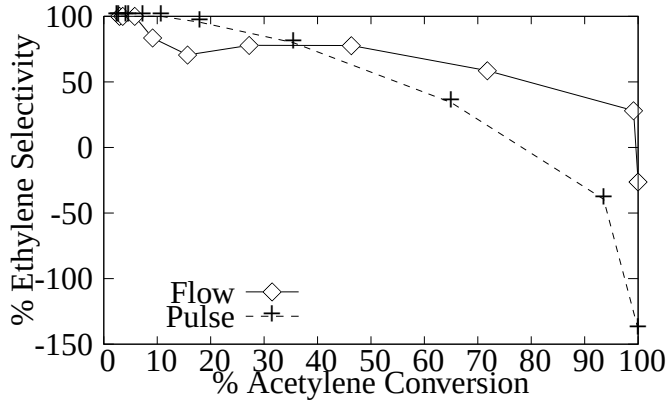

Figure 4.6: Selectivity comparison between pulse and flow operation of PdNP/C catalyst bed.

Chapter 5

Ligand and support effects of supported PdNP catalysts for acetylene hydrogenation

The synthesis of heterogeneous catalysts has typically been achieved using one of two wet chemical routes, both of which can result in metal particles of varying size and dispersion. The most common and well-documented technique is to simply contact a dissolved metal precursor with the desired support. This can be achieved by incipient wetness [79, 80] or coprecipitation methods [21], both of which require a heat treatment in either an oxidizing or reducing environment, depending on the precursor used. Particle growth is not mediated by any control mechanism and the resulting particles often vary in size by a factor of 6-7 [21, 80].

An increasingly popular alternative is to synthesize particles prior to impregnating on the support, thus achieving a much finer degree of control over the particle size and, ideally, dispersion on the surface. Many elegant routes to prepare colloidal capped nanoparticles have been described [81, 82], but they suffer from a common problem in that the particle

size is not maintained when preparing and activating the catalyst. Choo et al. [81] report a critical limitation of polymer encapsulation synthesis for the production of heterogeneous catalysts. They found that the particle size was inversely proportional to the concentration of the polymer used. This presents a challenge as the smallest, most desirable particles are also the ones that are coated with the most organic material. The difficulty arises due to the need to remove the capping agents to expose the metal surface for catalytic reaction. Heat treatment is not a viable option as it results in the same particle growth described in the impregnation method. Radio-frequency plasma generation can remove organic material without heating to elevated temperatures; however, Gehl et al. report that surface modification is unavoidable with this technique [83].

In previous work, we found that Pd NPs could be synthesized with a narrow size distribution without capping agents, which enabled us to produce an active Pd/C catalyst without pretreatment [84]. The activity and selectivity of a reaction, specifically alkyne hydrogenation, has been shown to be strongly dependent on the initial state of the catalyst [85]. Clean Pd, PdH and surface PdC were reported to produce drastically different results under identical reaction conditions. The authors reported that formation of PdC inhibited hydrogen uptake, while on a clean Pd surface, a hydride formed easily. The clean and PdH surfaces indiscriminately hydrogenated any adsorbed hydrocarbon, while PdC selectively hydrogenated alkyne to alkene. Other reports describe surface carbon [78] and Pd alloys [76, 86] achieving a similar result. Electronic effects have been suggested where PdC [87], PdAg [7] or acetylene poisoning [88] energetically favor alkyne adsorption but not the alkene. The need for carbon in monometallic selective hydrogenation catalysts can be evaluated by comparing oxide and carbon supported Pd NPs.

The solution synthesis technique developed in our group [84] enables the rapid, facile production of Pd NPs which were easily deposited on a carbon support. In this work, we have synthesized a series of PdNP/C and PdNP/oxide powders in order to understand the influence of synthesis conditions on the activity and selectivity of the final product. Pre-

treatment was found to be a significant factor in the selectivity of the catalyst. Residual precursor on the oxide-supported samples reduced during reaction conditions, producing numerous clusters of non-selective particles. In contrast, the carbon-supported sample consisted entirely of pre-reduced NPs, which were more favorable for selective hydrogenation. Additionally, formation of coke [78] and green oil [80] is a significant consideration which our clean, environmentally benign synthesis avoids.

5.1 Experimental

Oxide- and carbon-supported catalysts were prepared using methanol-assisted photoreduction as described in previous work [84]. Supports used in this study include γ-Al_2O_3 (Sasol Capatal B, calcined to 850°C for 5 hours prior to use), TiO_2 (anatase, Aldrich 99.97%), carbon (Vulcan XC72R) and ZnO (Aldrich 99.99 %). Powders were transferred to the glovebox by slurrying with 5-10 mL of methanol (MeOH) or pyridine (py) and drying under vacuum. Nanoparticles were prepared by dissolving 0.02 g $Pd(OAc)_2$ in 20 mL MeOH in an argon-filled glovebox. The solution was decanted into a 250 mL flask containing 1 g of the support powder. This process was repeated twice to dissolve as much of the precursor as possible, using 60 mL total volume of solvent. Any residual solids after the third addition were assumed to be insoluble and not added to the flask. Subsequently, the flask was transferred to a rotovap, where the powder was dried while maintaining the flask at room temperature in a water bath. The slurry was fully dried in about 10 minutes. A non-functionalized alumina supported sample was prepared in the same manner, except that the alumina powder was added outside the glovebox after 20 min. of reaction time. This sample will be refered to simply as PdNP/Al_2O_3. Fourier-transform infrared spectroscopy (FTIR) scans were conducted before and after each reaction using an attenuated total reflectance (ATR, Smart Orbit) attachment on a Nicolet 6700 scanning at 128 scans with a resolution of 4 cm^{-1}. Thermogravimetric analysis and differential thermal analysis

(TGA/DTA) were performed on a TA SQT Q600 under flowing N_2 at a ramp rate of 20 °C per minute. CO oxidation experiments were performed using a Varian CP-4900 Micro-GC utilizing a TCD detector. A balance of UHP He was used to maintain a ∼2% CO concentration in the gas stream (He=75 mL/min, CO=1.5 mL/min, O_2=1 mL/min). Each sample (0.020 g) was packed between portions of glass wool in a stainless steel reactor tube. The temperature was set to increase to 300 °C from room temperature at a rate of 2 °/min. The gas exit stream of the reactor was sampled every 3 minutes for the entire duration of the temperature ramp. Acetylene hydrogenation samples were prepared by pressing each powder under ∼7 metric tons and subsequently crushing and sieving to between 100 and 250 μm to attain a suitable packing size for the 0.25 inch glass tube reactor. A 0.015 g sample was mixed with 0.30g SiC (350 μm average grain size, Washington Mills) as an inert to alleviate thermal effects and mixed thoroughly in the reactor tube before capping with quartz wool. The reactant gases consisted of a mixture of 0.5% acetylene, 35% ethylene (balance nitrogen) and hydrogen to produce a 5:1 ratio of hydrogen to acetylene. Gas flowrates were 66 mL/min hydrocarbon and 1.4 mL/min hydrogen; all were UHP grade from Matheson Trigas. Product gases were sampled by a Varian 3800 gas chromatograph at intervals of 10 °C. After the test was complete, the reactor was purged with N_2 and cooled to room temperature before repeating for a total of 5 trials for each sample. The catalyst powders were examined by scanning transmission electron microscopy (STEM, JEOL 2010F 200 kV) to determine the size and composition of the particles before and after pretreatment.

Figure 5.1: The dried (as-prepared) PdNP/MeOH-Al_2O_3 (left) was substantially darker than PdNP/py-Al_2O_3 (right).

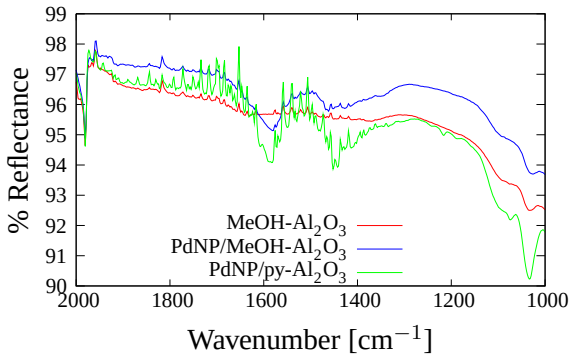

Figure 5.2: FTIR-ATR plots of MeOH-Al_2O_3 and PdNP/MeOH-Al_2O_3.

5.2 Results and Discussion

5.2.1 Reduction of $Pd(OAc)_2$ to Pd^0

Reduction in solution

Once the $Pd(OAc)_2$/MeOH solution was mixed with MeOH-Al_2O_3 as described in the previous section, rapid reduction was observed. As the solution was mixed with the dried powder, a rapid color change from yellow to olive green/grey was observed. This color change was previously noted [84] and attributed to particle aggregation in solution. The resulting powder was a dark brown (Figure 5.1), visually suggesting that rapid reduction and growth had taken place. ATR-FTIR scans indicated the presence of organic species on the surface (Figure 5.2). Clearly, the AP catalyst was coated with organic material. This

suggests that some residual precursor monomers were present, despite an observed reduction in solution. The the extent of reduction was highly dependent on the oxide surface chemistry. When the oxide was slurred in py and dried prior to synthesis, no observable color change took place. The solution was light yellow, and when mixed with the γ-Al_2O_3 powder, the resulting suspension was beige. Upon drying, the resulting powder was only slightly shaded, appearing white unless held next to a stock sample for comparison. In contrast, the MeOH-functionalized γ-Al_2O_3 was not an attractive surface for the precursor monomers, which proceeded to reduce in solution.

5.2.2 Reduction on the oxide

Other oxides used in this study did not exhibit a pronounced color change during synthesis, and the resulting powders were light beige. Comparisons between MeOH- and py-ZnO, -TiO_2 and -MgO indicated that the presence of bound solvent did not strongly influence the synthesis.

Pd-NP/TiO_2

Like the γ-Al_2O_3 in Section 5.2.1 the pretreatment of the oxide influenced the presence of acetate peaks in the prepared sample. The MeOH$-TiO_2$ exhibited minor peaks in the 1400-1600 cm^{-1} range; however, py$-TiO_2$ demonstrated many more features in this region. Two very sharp peaks at 1600 and 1400 were attributed directly to the py, while broad shoulders were found after depositing the PdNP in solution (5.7). These peaks directly match the features of $Pd(OAc)_2$, which suggests that some residual organic material accumulated on the oxide during solution synthesis. After reduction, the sharp peaks at 1600 and 1400 were significantly diminished, while the shoulder remained relatively unchanged. A TGA/DTA scan of the powder in H_2 to 350 °C showed fewer events than the PdNP/py-TiO_2 (Figure 5.3). Micrographs of the catalyst taken before (Figure 5.4a) and

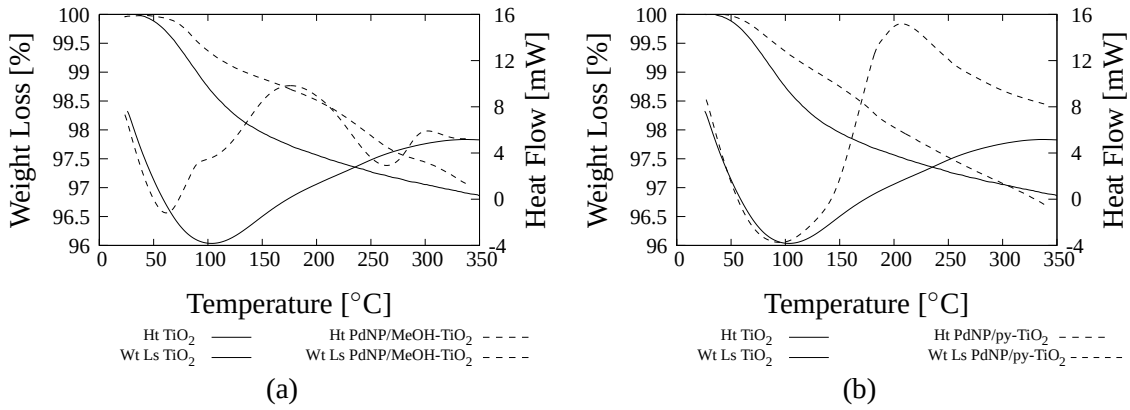

Figure 5.3: TGA of (a) PdNP/MeOH-TiO_2 and (b) PdNP/py-TiO_2.

after (Figure 5.4b) TGA reduction show the presence of sub-nanometer particles which grow slightly to 2-3 nm upon reduction.

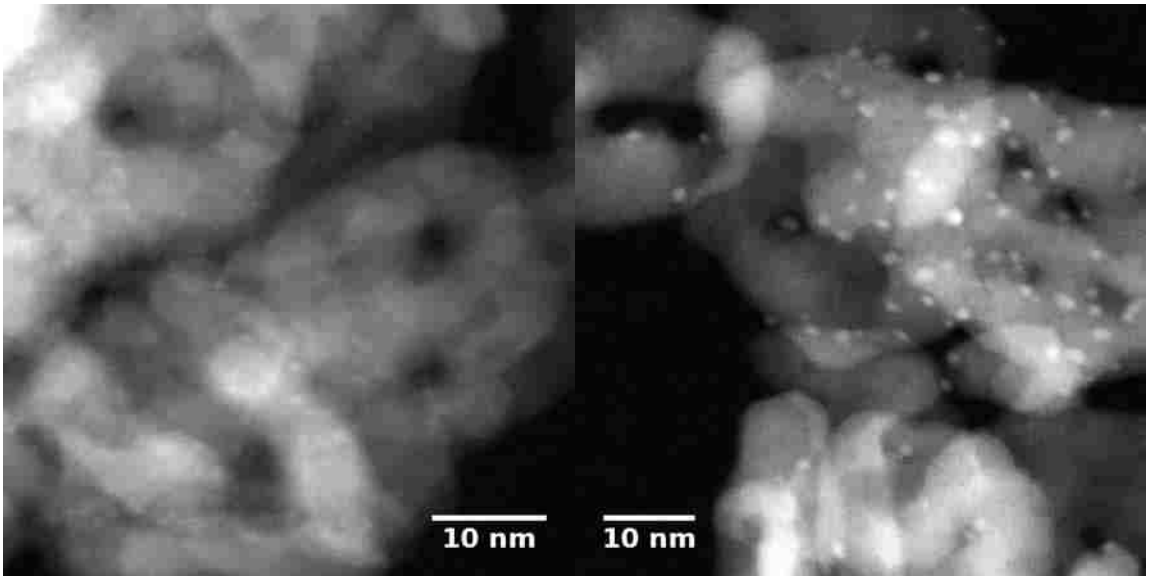

Figure 5.4: TEM micrographs of PdNP/MeOH-TiO_2 (a) as-prepared and (b) after reduction in H_2 at 350 °C.

5.2.3 CO oxidation

CO oxidation experiments confirmed the presence of residue, which was easily removed under reaction conditions. CO oxidation confirms a substantial difference between the two catalysts, as the PdNP/MeOH-Al_2O_3 did not undergo an activation process (Figure 5.5a). The nearly white PdNP/py-Al_2O_3 did reduce under reaction conditions, resulting in a much more pronounced change in activity between the first and second trials (Figure 5.5b).

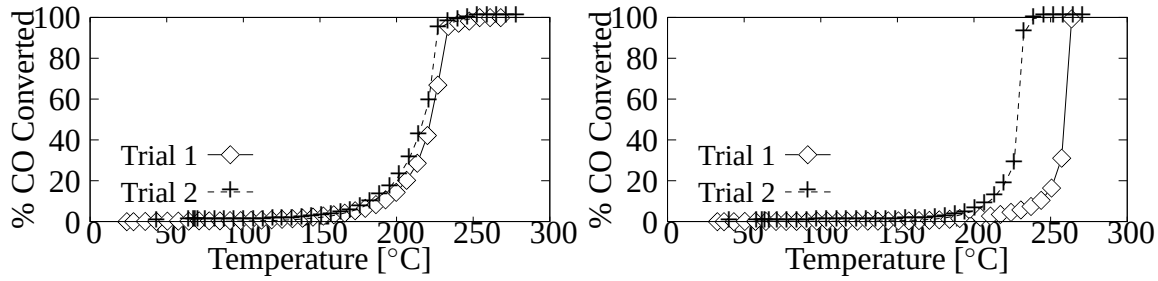

(a) PdNP/MeOH-Al_2O_3 (b) PdNP/py-Al_2O_3

Figure 5.5: Oxidation of CO over supported catalysts.

The CO oxidation activity correlates closely to the acetylene hydrogenation activity. The activation observed after the first acetylene trial suggests that the excess hydrogen in the feed reduced the monomers, resulting in more active sites for each subsequent trial. The excess hydrogen in the feed likely prevented PdC formation, as García-Mota et al. [87] report that PdC formation is not favorable on existing PdH surfaces. The reduction was highly dependent on the oxide pretreatment, as shown by the differing activities in Figures 5.6a and 5.6b. Interestingly, the py-TiO_2 demonstrated a substantial improvement upon reduction, which may be due to the bound py preventing agglomeration. This suggests that the PdNP/py-TiO_2 surface underwent minor changes. Paradoxically, the PdNP/py-TiO_2 showed the greatest drop in CO light-off temperature (Figure 5.6b)

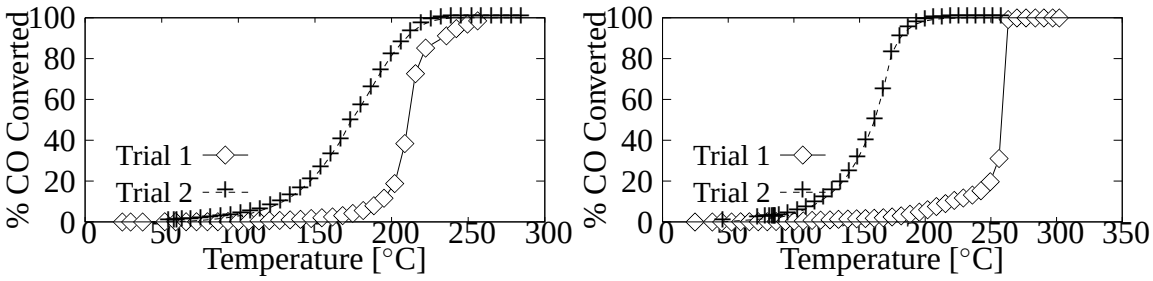

(a) PdNP/MeOH-TiO_2 (b) PdNP/py-TiO_2

Figure 5.6: Oxidation of CO over TiO_2.

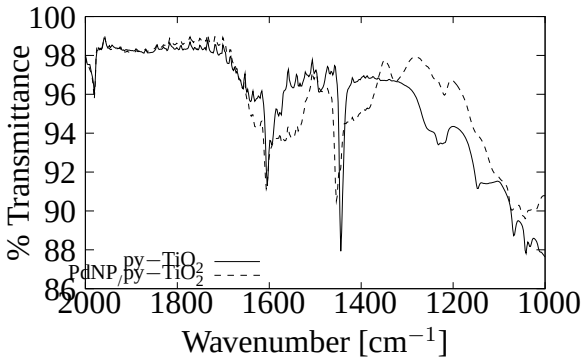

Figure 5.7: FTIR-ATR plots of TiO_2 support.

Pd-NP/ZnO

The ZnO-supported samples showed much less change between the AP and reduced catalysts. While TiO_2-supported catalysts underwent substantial reduction during the CO oxidation reaction, the ZnO-supported powders exhibited only a small change in light-off temperature (Figure 5.8a). This small change in activity corresponds to minor surface changes observed by TGA and FTIR. Much less mass was volatilized under reduction conditions

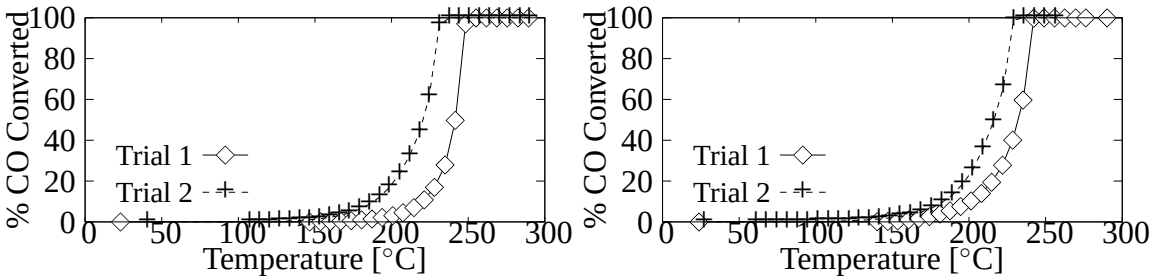

(a) PdNP/MeOH-ZnO (b) PdNP/py-ZnO

Figure 5.8: Oxidation of CO over ZnO.

5.3 Acetylene hydrogenation

The activity and selectivity of PdNP/γ-Al_2O_3 underwent an activation process, as shown in 5.9. After the initial reaction, each subsequent trial demonstrated a slight thermal runaway at the first temperature point. Although the temperature controller was set at 35 °C, the recorded temperature was 40 °C for trials 2-4. Each subsequent point was within 1 °C

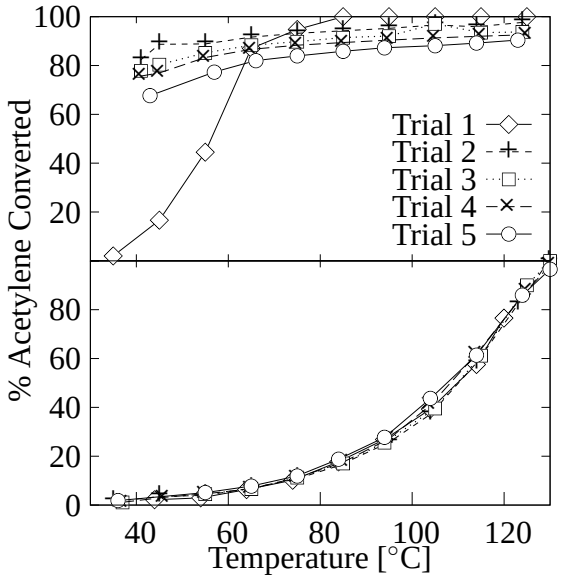

Figure 5.9: Conversion of acetylene over PdNP/γ-Al_2O_3 (top) and Pd-NP/C (bottom) catalysts after repeated trails. Lines are added as a visual aid only.

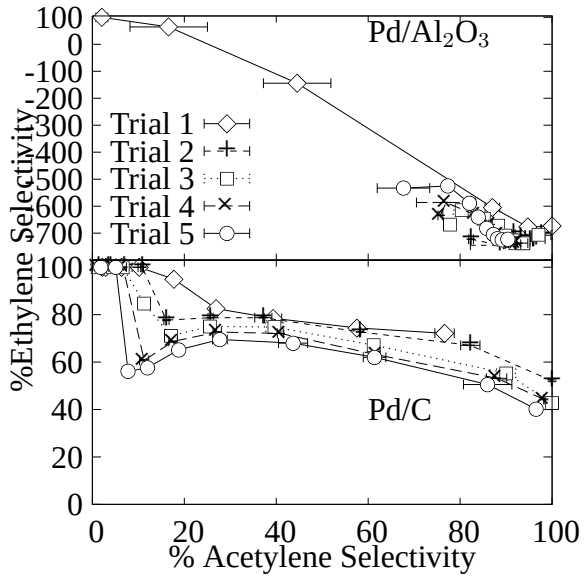

Figure 5.10: Ethylene selectivity over Pd-NP/γ-Al_2O_3 (top) and Pd-NP/C (bottom) catalysts after repeated trails. Lines are added as a visual aid only.

of the setpoint. The conversion at low temperatures also increased significantly; trials 2-4 each begin at $\sim$ 75 % conversion whereas the initial trial showed negligible activity. Due to the increased activity, the corresponding selectivity was only comparable at high conversion (Figure 5.10), although minimal differences were observed between each trail.

5.3.1 PdC-NP/C

The acetylene hydrogenation activity of PdC-NP/C remained constant after several trials (5.9), which suggests that the surface was not modified during reaction. The selectivity to ethylene decreased slightly at each trial (Figure 5.10) however, net production of ethylene was maintained at full conversion for each trial. These observations suggest that the surface of the NPs remains constant while surface adsorbates cause a change in selectivity.

5.4 Conclusion

This work has shown that the support used when preparing heterogeneous catalysts via the alcohol reduction route influences the composition of the resulting NPs. The resulting Pd-NP/C catalyst exhibited greater selectivity, but reduced activity in comparison to the Pd-NP/oxide catalysts. It is likely that the high selectivity was due to abundant carbon deposits on the Pd-NP/C catalyst. Literature reports [87, 89] describe diffusion limitations when generating surface PdC *in operando*. As the pre-formed NPs were already coated in carbon, the production of PdC was facile in this case. This PdC species was responsible for the high selectivity observed in this work and previously [84]. In contrast, the Pd-NP/oxide catalysts exhibited poor selectivity, which is frequently reported [85, 87] to be due to clean Pd metal or PdH. These surfaces *were* formed during reaction due to the presence of unreduced precursor. Reports in the literature [90, 91] describe strong binding of acetylacetonate to oxide surfaces. As the $Pd(OAc)_2$ precursor is chemically similar to acetylacetonate, it is likely that residual monomers bonded to the oxide during synthesis. These monomers were not removed when the powder was dried, and were only reduced when subjected to excess hydrogen in the reactor. As noted in Section 5.2.1, a hydrogen-rich environment prevents PdC formation, thus *in operando* reduction leads to a non-selective catalyst. In contrast, the precursor monomers were not strongly bound to the carbon, and thus only the fully reduced nanoparticles remained on the surface when drying. The fully reduced metal therefore exhibited consistent catalytic performance when subjected to a reducing environment. These particles were slightly larger than the adsorbed monomeric species present on the oxide, which is why the activity of Pd-NP/C was lower.

Therefore, we conclude that the alcohol reduction method to prepare NPs for supported catalysts is dependent on the support used.

Chapter 6

Density Functional Theory

6.1 Background Theory

Density functional theory is a method to solve the N-electron Schrödinger equation. Each of the N electrons requires 3N dimensions to describe, so large systems become difficult to calculate very quickly. To simplify the matter, Hohenberg and Kohn [92] showed that the 3N electrons can be modeled by a single electron in an effective potential [93]. The benefit to this manipulation is that by mapping the entire system onto a single electron, the 3N dimensions shrink to only 3, which rapidly reduces the complexity of the problem [94]. The effective potential itself thus becomes the problem of interest. The Kohn-Sham [95] system is able to find the potential exactly from the probability density. It does so by taking the liberty of using a system of non-interacting electrons with the same density as the real system [94]. A non-interacting particle obviously doesn't exist, but it is a useful concept to model the system. Actually achieving this numerically remains difficult [93], so there are many ways to work around this limitation and calculate problems as accurately as possible. The simplest is the Hartree-Fock effective potential, which is able to produce a good pattern, but is not exact. It misses the correlation energy [94], which

is improved upon by a local density approximation (LDA) and further by a generalized gradient expansion (GGA). The LDA approximates the total energy by setting the kinetic energy density equal to a uniform electron gas [94]. Thus, when the kinetic energy density is numerically equal to the uniform electron gas density, the approximation is perfect, and when it's not, the approximation only has a small error ($\approx 15\%$). Most important to this study, the LDA overestimates cohesive energies and can miss transition state barriers entirely [94], which makes it less than ideal. The LDA can be improved upon by using a gradient expansion of the density functional. The gradient expansion approximation is an improvement over the LDA in most respects. It is more accurate, but instead of slightly underestimating the exact values, it tends to overestimate. Burke [94] notes that a simple gradient is not sufficient to correct the LDA, it must be 'patched' in a few places. First, the LDA is uniform, but when a gradient is applied, errors in the LDA propagate to very large values at one end of the spectrum. This must be accounted for by artificial constructions, producing the generalized gradient approximation (GGA). The error in a GGA calculation is numerically smaller than an LDA, so the GGA is a useful tool in density functional calculations.

Many of the numerical methods used rely upon plane waves for computational efficiency [93, 94]. Specifically, plane waves are easy to treat with fast Fourier transforms; making periodic calculations comparatively simple. In the instances where periodic calculations are more difficult; such as the core electrons, a pseudopotential is used to simplify the matter. Pseudopotentials simplify the calculation by replacing the core electrons with an effective potential. While this enables the calculation to execute in less time and preserve the valence electrons, it does introduce a contrived nature to the calculation.

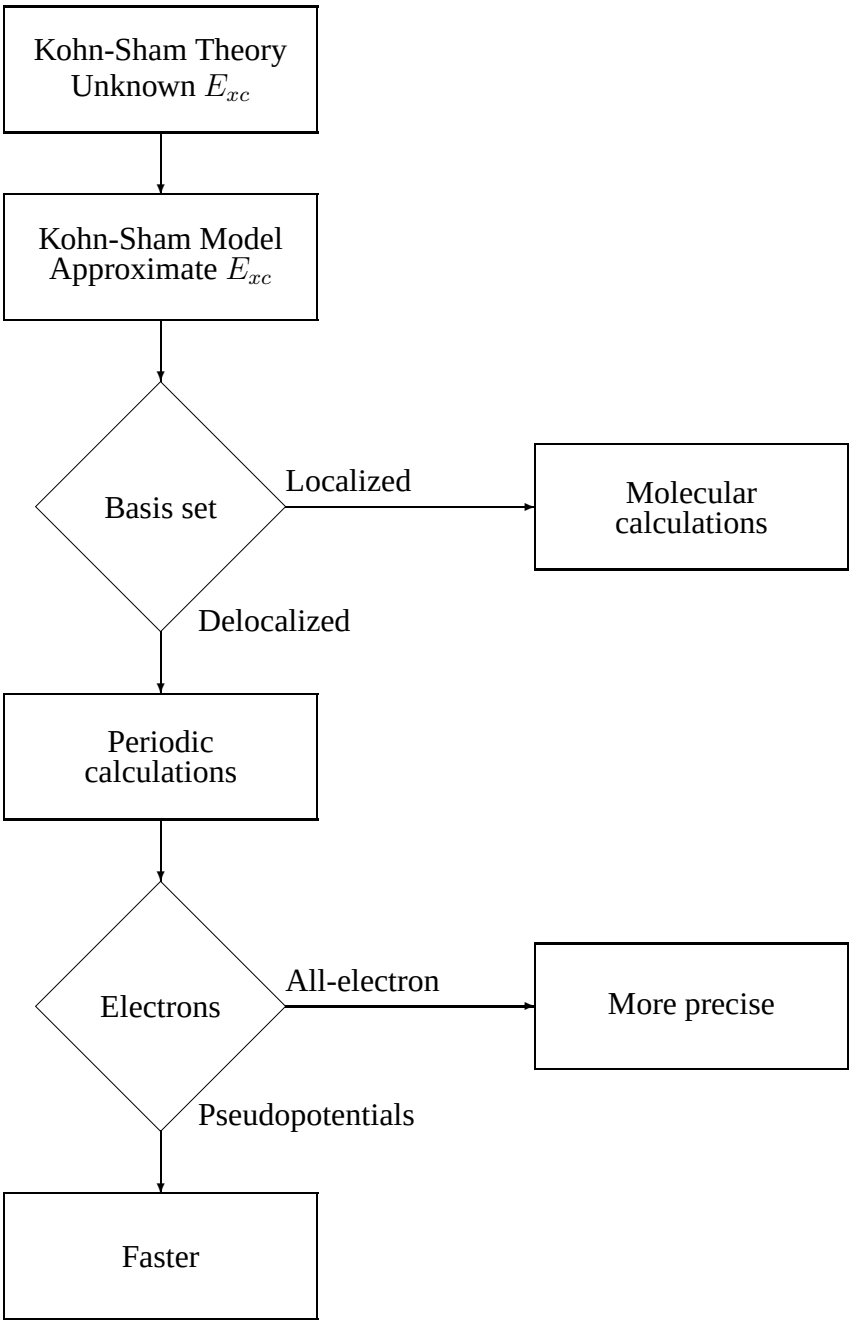

Figure 6.1: Conceptual flowchart of DFT

Chapter 7

Long-Range Effects on Adsorbates

7.1 Introduction

PdZn is a well known methanol steam reforming catalyst; however, the precise mechanism by which it performs is not well understood. Specifically, it is known that Zn modifies Pd to produce a reforming catalyst, (Equation 1.5) while pure Pd merely decomposes methanol (Equation 1.6). Many researchers have attempted to deconvolute the behavior of PdZn by investigating individual components of the reactions. The behavior of PdZn has been shown to differ strongly from bulk Pd. In particular, recent surface studies by Jeroro et al. [22] have investigated several different structures of Zn in a Pd(111) surface. A range of Zn coverages from 0.00 ML to 0.50 ML was used to investigate the CO binding energy on PdZn bimetallic surfaces. An unexpected behavior was noted for the 0.06 ML coverage in which the CO molecule was noticeably less strongly bound to the 0.06 ML surface than the pure Pd surface. Despite the isolation of the Zn atoms at such a low coverage, these samples demonstrated unexpected CO desorption behavior. Density functional theory (DFT) serves as a useful tool to investigate the atomic nature of heterogeneous catalysts. Previous studies on PdZn [19], Ag-Pt [96] and other transition

metals [97] have shown that bulk alloys can be effectively modeled by DFT. These studies suggest that DFT can be extended to model systems with a much more disparate ratio of constituent elements. Instead of a true alloy behavior, these systems behave as enhanced modifications of the original substrate, analogous to a doped semiconductor in an otherwise nonreactive substrate. Neyman et al. [98] have shown that the position of Zn in Pd-Zn clusters influences the adsorption energy of CO molecules. The extent of Zn coverage was not investigated and remains unknown. This open question provided the motivation for the current work, in which we investigated the CO binding energy on transition-metal (Cu or Zn) doped Pd(111) surfaces. We have shown that the behavior of the CO on the surface was strongly influenced by atop-bound Zn atoms. Atop Zn extended a greater region of influence over the surface than a Zn atom substituted in the Pd surface. The CO binding energy was found to diminish substantially within the region of influence of a modifier atom (2.25 Å), however, the effect was not noticed at binding sites farther away from the modifier. These findings suggest that very small amounts of a modifying metal can influence the binding energy at sufficiently high temperatures.

7.2 Method

Calculations in this study were performed using the GPAW [99] projector-augmented wave method [100] with the ASE interface [101]. Electronic exchange-correlation was described by the RPBE functional [102]. All calculations used a grid spacing of 0.2. The bulk properties (equilibrium lattice parameter and cohesive energy) were found by calculating the energy of a bulk Pd unit cell with varying lattice parameters and fit to the Murnaghan [103] equation of state (See Appendix E). The optimized lattice parameter was 4.026 Å and was used to construct a (111) slab. Pd surfaces were constructed to mimic the 0.06 LEED model reported by Jeroro et al. [22] by one of two different approaches. The first treated the foreign metal as a substitution defect, replacing a single Pd atom in a 4×4

Pd(111) surface with four layers and 12 Å of vacuum between each surface. The second technique treated the modifier as an adatom adsorbed to an fcc site on a pure 4×4 Pd(111) surface. In both cases, a k-point sampling of $2 \times 2 \times 1$ was found to be sufficient, yielding 2 k-points in the irreducible Brillouin zone. The supercell geometry resulted in a 0.0625 ML surface coverage of Zn or Cu, which closely matched the experimentally characterized 0.06 ML surface [22]. The bottom two layers of each surface were constrained, while all other atoms were allowed to relax using a quasi-newton minimization scheme. A single CO molecule was adsorbed to various sites (Figure 7.1 and Figure 7.2) with the C oriented towards the surface as described by the Blyholder model [104]. The entire structure was allowed to relax by a QuasiNewton minimization scheme until the force was less than 0.03 eV/Å. A corresponding study was conducted on a simple 2×2 surface to find the binding behavior of CO on large coverages ($\theta > 0.25$ ML) of Zn.

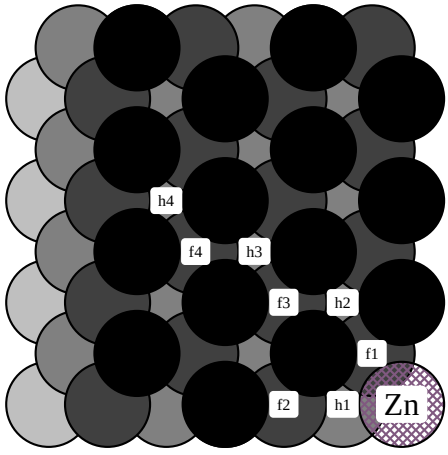

Figure 7.1: Schematic of 4×4 Pd slab showing each site of adsorbed CO. Atomic layers are shaded from darkest (top) to lightest, and atomic radii are condensed to more clearly illustrate each binding site.

The binding energy was found by subtracting the energy of each component from the energy of the relaxed surface;

$$E_b = E_{slab+CO} - E_{slab} - E_{CO} \tag{7.1}$$

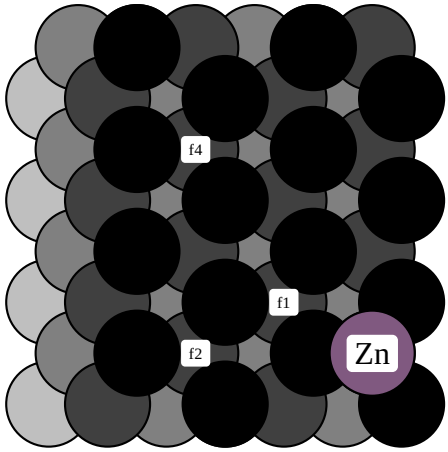

Figure 7.2: Zn atop-adsorbate.

In order to make an effective comparison of each binding site, the binding energy as a function of distance from the modifier atom has been plotted in Figure 7.3.

7.3 Results

The most substantial effect was observed when the CO molecule was in direct contact with the modifier atom (Figure 7.3). CO was less strongly bound to both Cu and Zn when attached at either an fcc or hcp site. The nearest fcc site to the atop modifier (denoted as f1 in Figure 7.2) presented an interesting result. Since the modifier was outside the lattice, it was free to interact over a longer range than its in-lattice counterparts. All other binding sites demonstrated a similar binding energy to an unmodified Pd slab (Figure 7.3, dotted lines). Likewise, the influence of the modifying constituent was most noticeable at the immediately adjacent site. The difference between binding to Zn- and Cu-doped surfaces was numerically significant at this site, where elsewhere on the surface, there was no appreciable difference between the two surfaces. Thus; the modifier atom, whether Cu or Zn, behaved as an ‘atomic island’, where the behavior of CO near the island was more

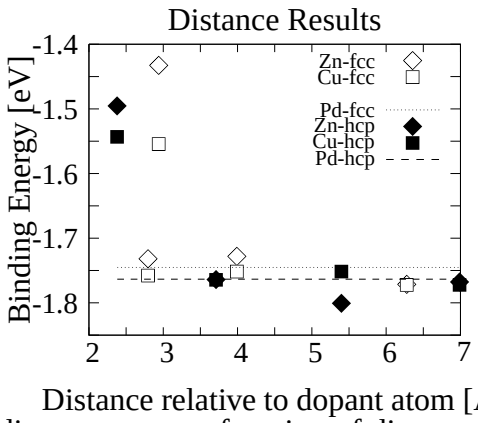

Figure 7.3: Plot of CO binding energy as a function of distance from the modifier atom. FCC sites are marked by filled symbols, while HCP sites correspond to open markers.

strongly influenced by the modifier metal than at positions farther away into the bulk. This shielding effect precluded the possibility of a long-range effect caused by the modifier metal. Such an observation negated one of the proposed causes for the unexplained CO desorption observed by Jerroro et al. [22]; i.e. direct CO desorption from the surface. One possible mechanism provided the possibility that the modifier atoms exerted a long-range electronic effect on the neighboring Pd atoms. In this scenario, the adsorbed CO was thought to directly desorb from the electronically modified Pd surface; i.e. the molecule would not have been in direct contact with the modifier atom. However; it was observed (Figure 7.3) that this was not the case. The CO molecule binding energy was not affected by the modifier atom due to the shielding of the neighboring Pd atoms.

7.4 Discussion

The short-range activity of transition metal modifiers in Pd surfaces suggested that the Redhead treatment [105] of uniform CO could not explain the desorption behavior observed by Jerroro et al. [22]. The models used in this study illustrated that CO behaved differently in correlation to proximity to the modifying atom. Specifically, the CO binding

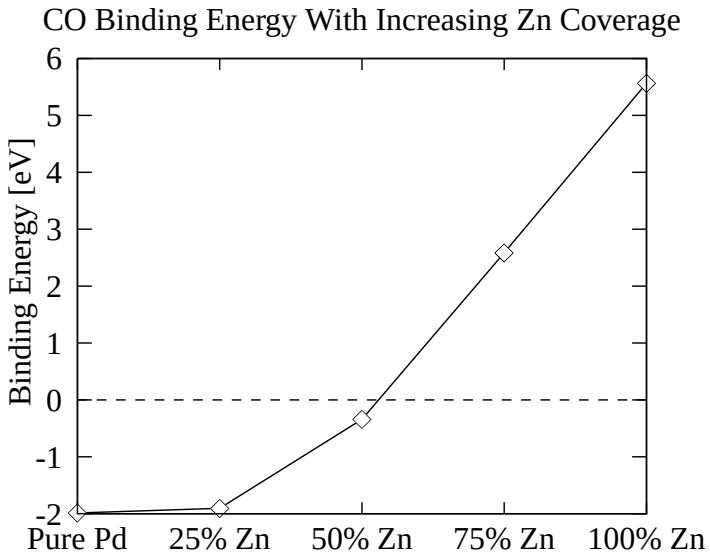

Figure 7.4: Plot of CO binding energy as a function of Zn coverage on a Pd(111) surface. Lines are added as a visual aid.

energy followed a steady trend proportional to distance from the atom. In the case of in-lattice modification, the effect of the modifier was limited to adsorption sites in immediate contact with the atom. This resulted in a very pronounced distinction between the behavior of the modifier and bulk surface. These results were interpreted to be a manifestation of the ensemble; the surrounding Pd atoms blocked any electronic effect of the modifier atom. Huang and coworkers [106] reported a stronger influence of sub-lattice atoms compared to surface atoms, which agrees with this study.

In conclusion, we have demonstrated that the change in CO binding energy by modifier Cu or Zn atoms in a Pd(111) surface was strongly dependent on surface transition metal modifiers. This small region of influence could not have contributed to the unexpected desorption activity reported by Jeroro et al. [22].

Chapter 8

Conclusion and Outlook

8.1 Influence of synthesis on catalytic activity

This work has shown that the catalyst preparation technique is vitally important to the performance of the end product. Achieving maximum particle dispersion and minimum particle size is best accomplished by matching the precursor to the optimum support. Typical techniques such as incipient wetness and impregnation cannot sufficiently match the metal phase to the support as they are bulk processes. As a result, large metal aggregates form, and interfacial phenomena cannot be studied. Initial trials of *ex situ* particle nucleation addressed this problem, but relied upon a surfactant to prevent ripening. This approach successfully isolated the metal phase; however, reactivity and particle-support interactions were compromised. Capping agents can be avoided by using a mild reducing agent to slowly reduce the precursor. This technique is very effective when depositing particles on carbon, as the resulting powder is an immediately usable catalyst. When used on oxides, the deposition technique is strongly dependent upon surface chemistry, as illustrated by the stark contrast between MeOH-Al_2O_3 and py-Al_2O_3. This is a simple and effective synthesis technique.

8.2 Support and particle interaction

Support interactions are important to methanol steam reforming, particularly PdZn alloy formation from Pd/ZnO catalysts. Idealized ZnO surfaces featuring high exposure of (0001) planes have been prepared, but are not compatible with the current Pd deposition technique. The ZnO platelets are often coated in residual organic material, which interferes with characterization of organic residues on the surface of the support, or the deposited particles. Once this limitation is overcome, the technique developed provides the potential to prepare highly dispersed sub-nanometer particles directly onto an oxide support. Density functional studies conducted in this work illustrated the strong influence that single atoms can have over a limited region. A larger concentration of these atomic islands could provide substantial catalytic activity with orders of magnitude less metal phase than larger ($<$ 5 nm) particles currently require. The synthetic techniques outlined here could achieve an idealized result in a practical catalyst.

Appendices

Appendix A

Calibration Tests and Supplimental Information

A.1 Characterization and Baseline Activity of Vulcan XC72R

The Vulcan XC72R used in this study (Chapter 4) was examined to determine if there were significant contaminants that would interfere with the acetylene hydrogen reaction study. The carbon itself is slightly active, but this is diminished by diluting with a 1:5 ratio of SiC, as done in the experimental procedure (Section 4.2). It was concluded that the support would not contribute any significant error to the experimental results.

A.2 Weight Percent by EDS Analysis

EDS analysis was used as one technique to determine the weight loading of Pd nanoparticles on Vulcan XC72R supports. Carbon-less TEM grids were used to avoid background noise and were prepared by depositing ground sample in a thick ethanol slurry onto the

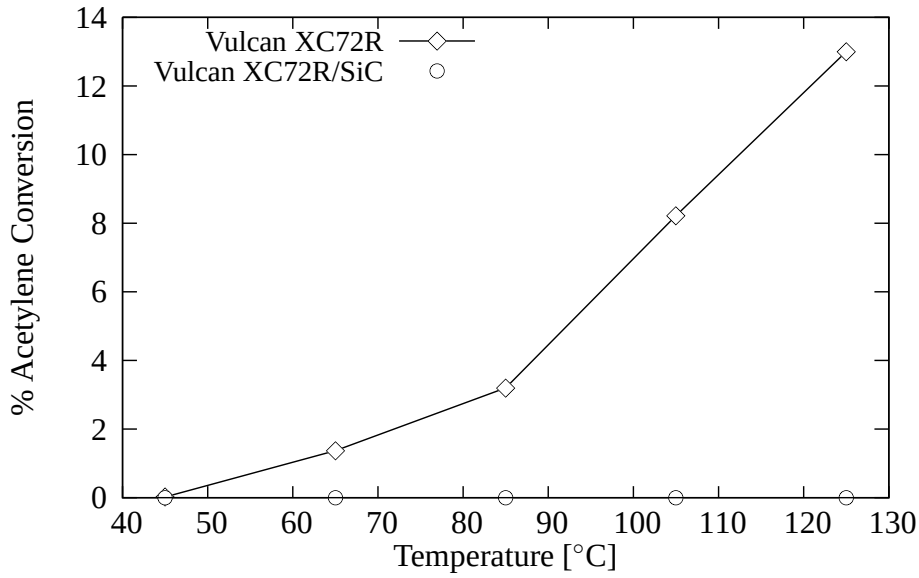

Figure A.1: Baseline activity of Vulcan XC72R compared to the same powder with SiC as an inert.

grid. Once in the TEM, the sample was tilted towards the EDS detector by 15° to reduce shadowing. EDS spectra were collected with INCA software and exported as plain text files and summary html reports. Data analysis was conducted by plotting each spectrum within windows displaying the $C_{K_{\alpha 1}}$ and $Pd_{L_{\alpha 1}}$ peaks. The quality of the data was assessed by comparing the C peak to the nearby noise peak to ensure that the C peak was greater, thus assuring that a reliable signal was collected. Likewise, the Pd peak was compared to the surrounding data points to ensure that the peak could be accurately extracted from the background. Spectra meeting both of these criteria were used analyzed to provide a weight loading for the sample.

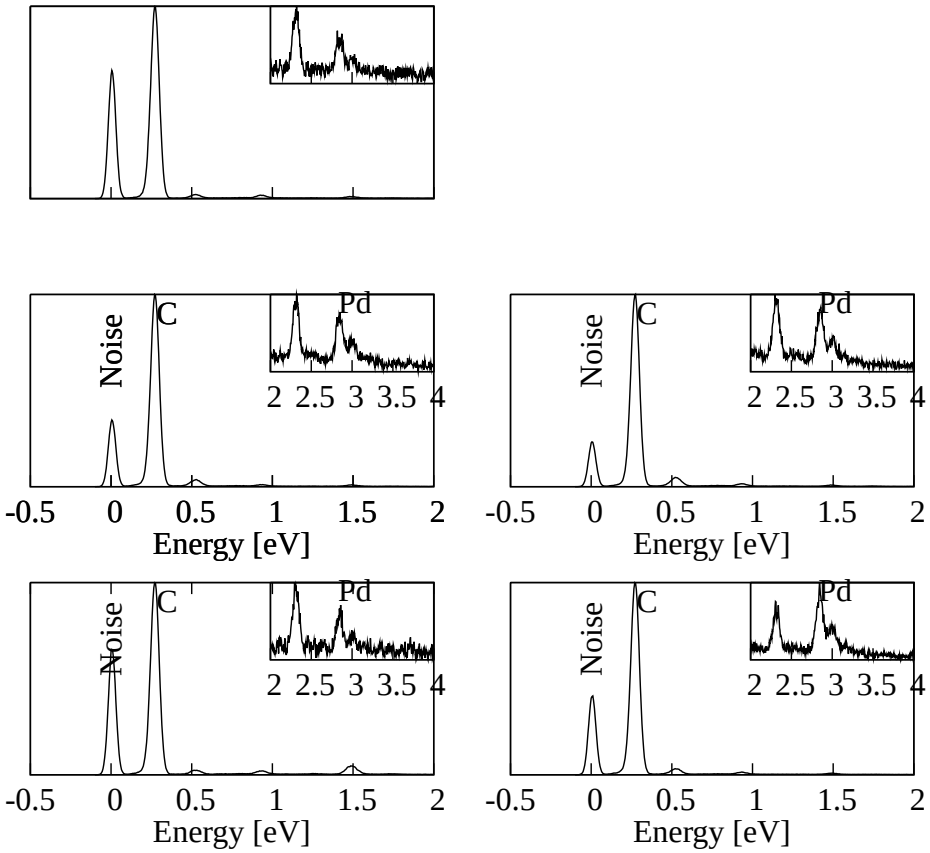

Figure A.2: Accepted EDS spectra.

Beginning of EDS multiple plot code

```
#!/bin/bash
mkdir plots
FILENAMES=$(ls *.txt)
for i in $FILENAMES
do
        CLEAN=$(echo ‘basename "$i" .txt‘)
        grep ^[^\#] $i > plots/data$CLEAN.txt
        sed "s/XXXX/$CLEAN/g" plot.gnu > plots/plot$CLEAN.gnu
        gnuplot plots/plot$CLEAN.gnu
done
```

End of Code

A.3 Catalyst Bed Layering

In order to prevent channel formation in the packed catalyst, a sample was loaded in multiple layers separated by small amounts of SiC. Samples packed in this manner with between 3 and 5 striations demonstrated substantially improved catalytic activity as each band behaved as a plug-flow reactor in series with the other components.

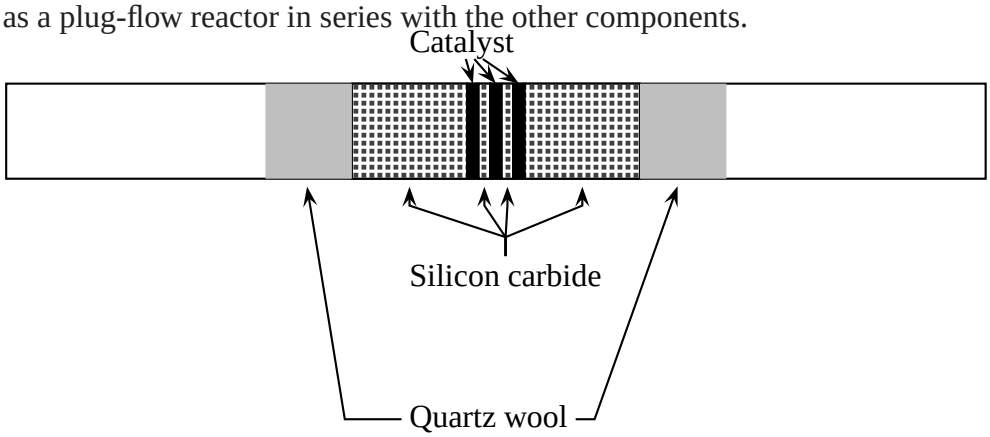

Figure A.3: Schematic of a 3-zone paching scheme for a Pd/C sample.

Appendix B

Mathematical Formulas and Derivations

The thickness of the ZnO plates discussed in Chapter 3 was found by equating the BET surface area to the theoretical surface area per unit mass of a cylindrical disc.

$$BET = \frac{SA}{unit\ mass} \tag{B.1}$$

$$BET = \frac{2(\frac{\pi a^2}{4}) + \pi ac}{unit\ mass} \tag{B.2}$$

$$BET \times \rho = \frac{\frac{\pi a^2}{2} + \pi ac}{unit\ volume} \tag{B.3}$$

$$BET\rho = \frac{\pi(\frac{a^2}{2} + ac)}{\frac{\pi a^2}{4}c} \tag{B.4}$$

$$BET\rho = \frac{2}{c} + \frac{4}{a} \tag{B.5}$$

Assume $c \ll a$

$$c = \frac{2}{BET \times \rho_{ZnO}} \tag{B.6}$$

Appendix C

Reitveld Refinement

Reitveld refinment of XRD samples was performed using General Structure Analysis Software (GSAS) [49] and EXPGUI [50]. EXPGUI is a graphical front-end to GSAS and is explained below. Both GSAS and EXPGUI are available on Windows, Mac OS X and Linux systems. This tutorial uses the Mac OS X version, however, operation is consistent across each platform. In addition to GSAS and EXPGUI, convX [107] is a useful utility to convert raw data to a GSAS compatible file.

1. Initialize the program and select the proper directory.
2. Enter the desired file name, followed by a `.exp` extension.
3. Change the number of calculation cycles to 30 (figure C.1). Most patterns will require at least 30 cycles per calculation, however, this is merely a suggested starting point.
4. Click the `Phase` tab and add a `.cif` file (figure C.2). Many `.cif` files are available online from Downs et al. [1].
5. Click the `Histogram` tab and add a collected pattern by clicking the `Add New`

`Histogram` button (figure C.3). Data generated with the Pan'Analytical X'Pert Pro can be converted to a GSAS `.raw` format by using an external program titled conveX. ConveX inter-converts several different XRD data formats.

6. Click the `Profile` tab and change the phase type to 2 for each phase.

7. The actual refinement step is performed by GSAS on a command line. Powpref and genles are executed from EXPGUI and display in a terminal or X window, depending on the operating system used. Run `powpref` and press `enter` to return to EXPGUI (figure C.4l). Press `Load New` to proceed when prompted.

8. Execute `genles` to calculate the curve fits. Make note of the χ^2 value and the convergence before pressing `enter` to return to EXPGUI (figure C.4).

9. View the pattern and fit by clicking on `liveplot` (figure C.5).

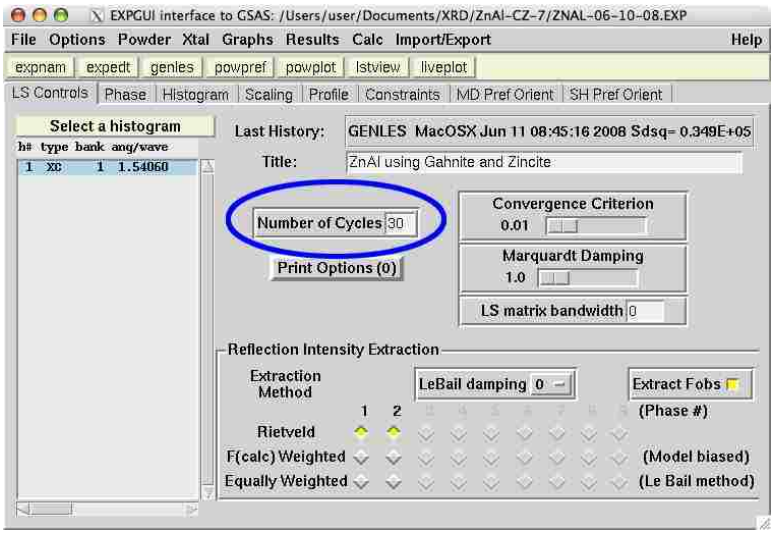

Figure C.1: Initial screen view for EXPGUI. To increase the number of calculations per run, adjust the circled setting.

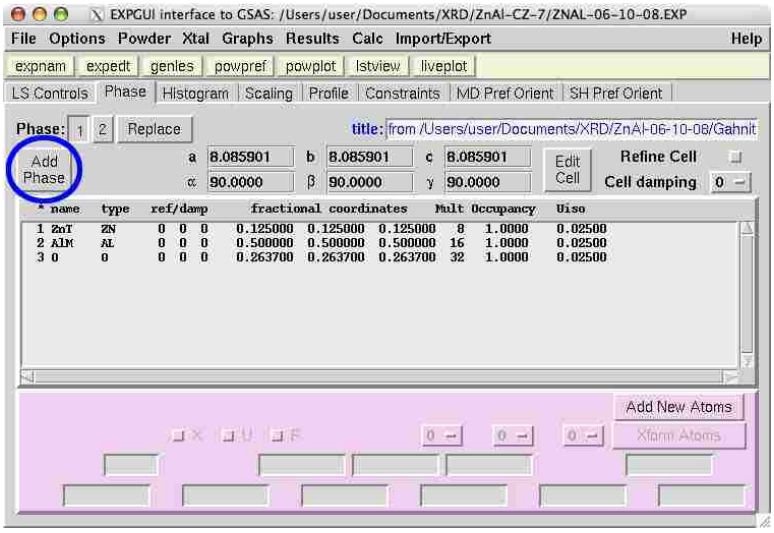

Figure C.2: Add reference phases as crystallographic information files (`.cif`).

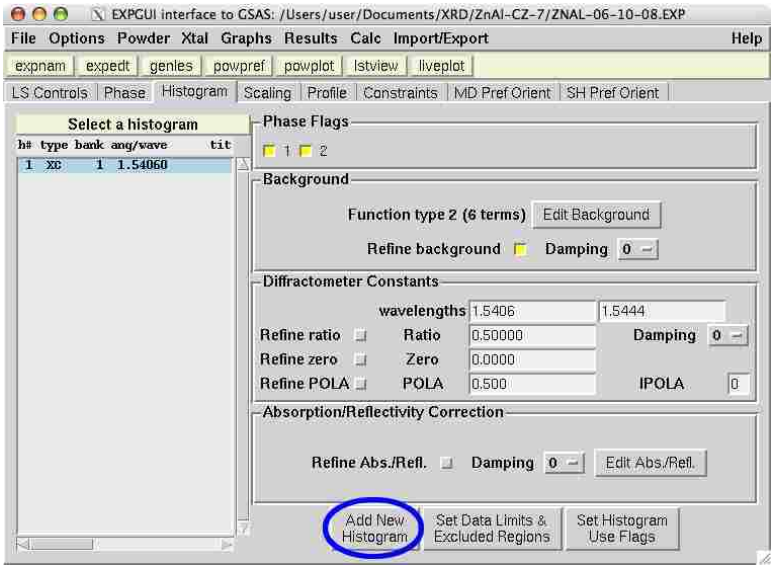

Figure C.3: Enter collected XRD patterns using the circled menu.

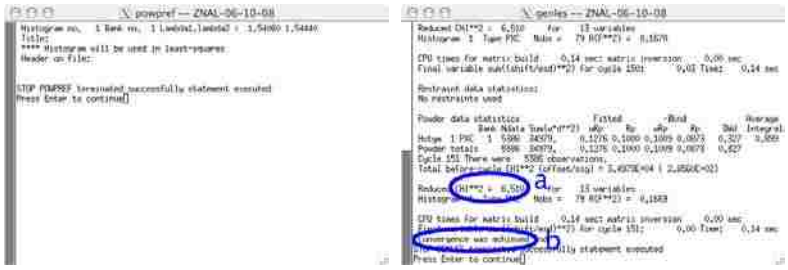

(a) Powpref window (b) Genles window

Figure C.4: Powpref and completed genles window displaying χ^2 value (a) and convergence (b).

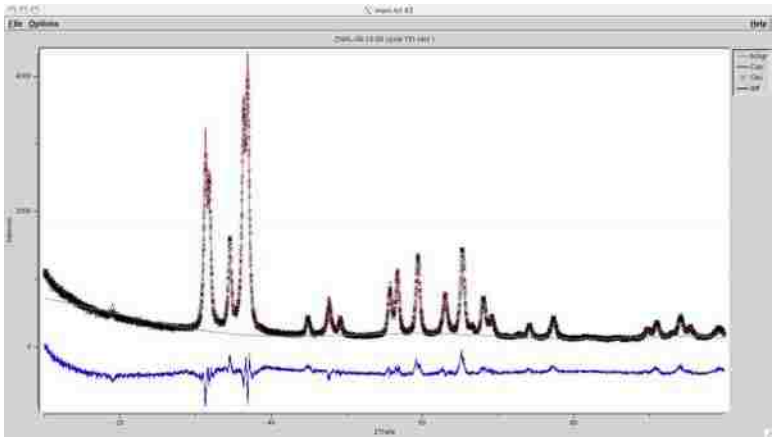

Figure C.5: The liveplot feature displays the completed Reitveld refinement with the original data as well as a difference pattern.

Appendix D

Acetylene Hydrogenation Reaction

D.1 Startup

1. Load a glass tube reactor with catalyst or catalyst/SiC powder and pack between two plugs of quartz wool (figure D.2).
2. Place tube in chosen reactor position (A, B, or C, figure D.1) and secure with fittings just until finger-tight.
3. Wrap the tube and fittings with resistance heating tape (figure D.2, red coil).
4. Open valve V3x (where x corresponds to position A, B, or C) and turn valve V2 to feed to position x.
5. Begin flowing reactant gases (H_2, V1c and hydrocarbon mix, V1b).
6. Set temperature controller TC to desired set-point before turning the variac to 120 V (position towards the operator).
7. Allow system to ramp and equilibrate for 15 minutes for a 10 °C temperature increment.

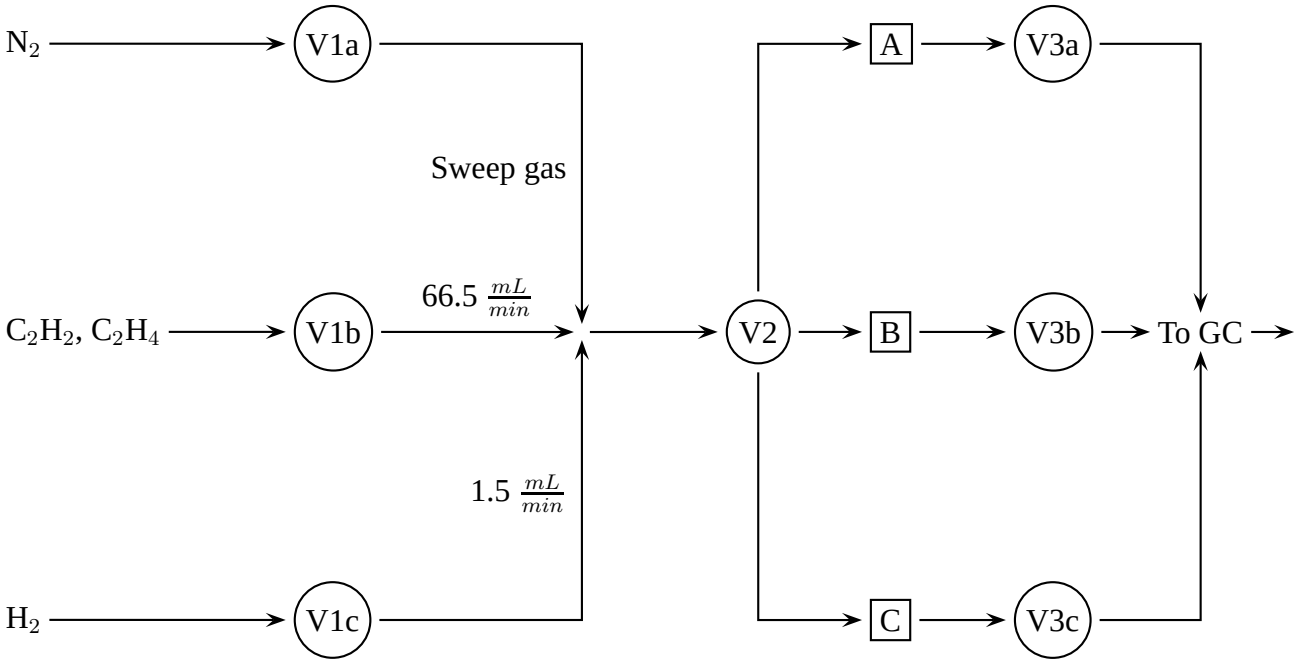

Figure D.1: Overall schematic of acetylene hydrogenation system.

D.2 Operation

1. Open `Varian Star Chromatography Station` if not already open. If you are prompted to select an IP address, select `10.2.128.6`.

2. Start the `Acetylene_Hydrogenation` method.

3. Select `File, New Sample List` to open the sample list dialog box.

4. Click the Add Lines button (figure D.3a) and change the number of samples to 5. Change `Default Sample` to a descriptive name.

5. Click the Data Files button in the sample list dialog box to select the folder to save each output file in.

6. Once the sample has equilibrated at the desired temperature (section D.1, item 7), click Begin (figure D.3b).

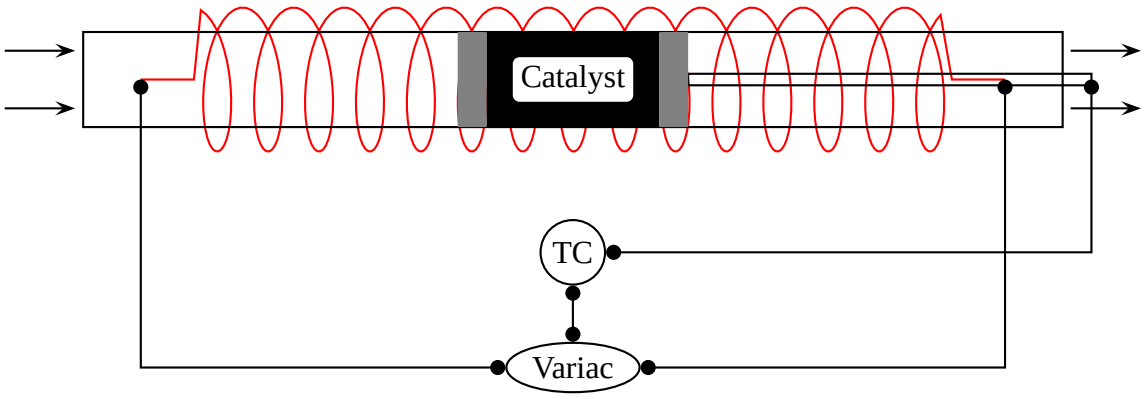

Figure D.2: Close-up view of a single reactor.

7. Allow sample to run for 30 minutes.

8. After data collection is complete, export the results files to ASCII text format by right-clicking on each file and choosing the `Convert Raw Data and Results to ASCII` option (figure D.4).

9. Adjust the temperature as soon as the last sample is injected; for a five sample series, this will occur at 30 minutes past the start point.

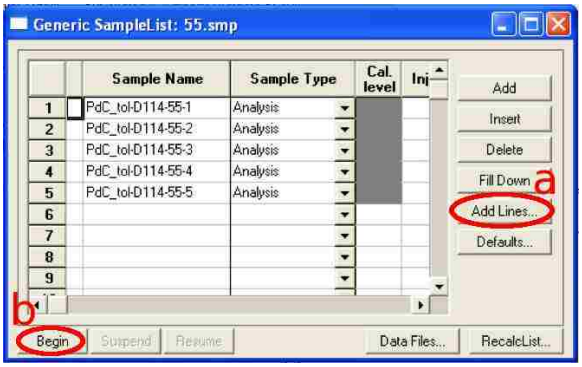

Figure D.3: example caption

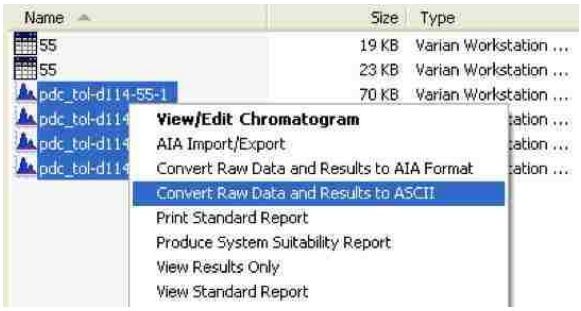

Figure D.4: example caption

D.3 Shut down

1. Once data collection is complete, turn the reactant gasses off and turn N_2 (V1a) on to full flow.
2. Turn the temperature controller and variac off.
3. Allow the line to flush while the reactor cools.
4. Turn off the N_2, close valve V3x.

Appendix E

Density Functional Theory Background Calculations

E.1 Bulk Metal and Alloy Study

The lattice parameters of Pd, Zn and Pd_XZn_Y (where X and Y = 1 and 3 or vice versa) alloys were investigated using GPAW [108]. The constant was varied around the experimental value of Pd and allowed to fluctuate between 3.847 and 4.188 Å. The total energy of the system was found using the RPBE functional [102] with an $8 \times 8 \times 8$ Monkhorst-Pack grid yielding 20 irreducible k-points. The resulting data points were fit to the Rose [103] and Murnaghan [109, 110] equations of state. The Murnaghan equation of state produced a better fit for each system studied, so it was used to provide lattice parameters for the following slab calculations. In addition, the curve fit provided data on the bulk modulus, B_0, which has been included in table E.1.

E.1.1 Bulk Pd

The study began by finding the appropriate energy cutoff and k-point mesh.

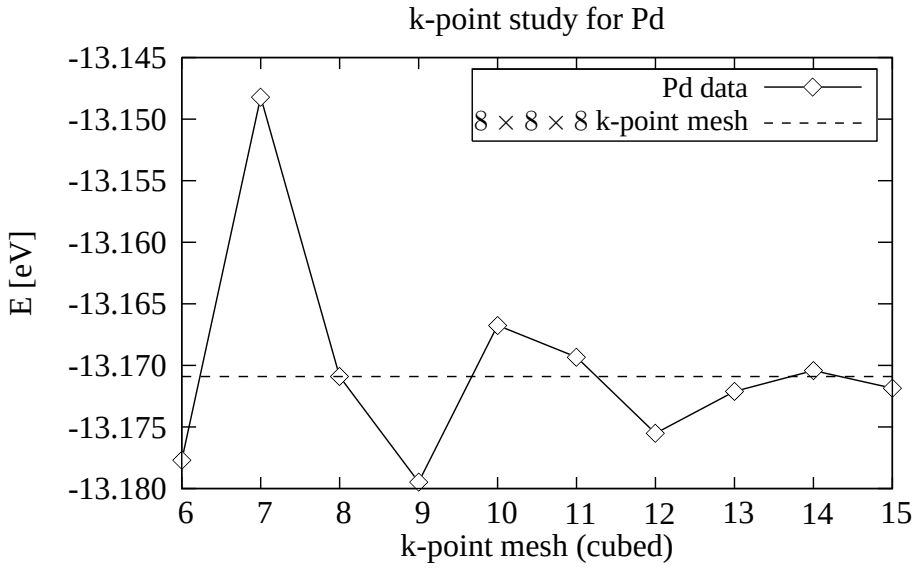

Figure E.1: The total energy with respect to k-points fluctuated around the value of the $8 \times 8 \times 8$ grid (-13.17 eV). Since no significant improvement could be obtained by using a finer k-point grid, subsequent calculations used the $8 \times 8 \times 8$ mesh.

The grid spacing was found to be varying as the size of the unit cell changed, so the grid points were manually set at $24 \times 24 \times 24$, which improved the output considerably. The slope of the curve matches the data points; however, the bulk modulus as calculated from the fit did not agree with literature values (see table E.1). The discrepancy between the literature and calculated bulk moduli is rather large and suggests a serious error. The resulting lattice parameter was calculated as 4.026 Å.

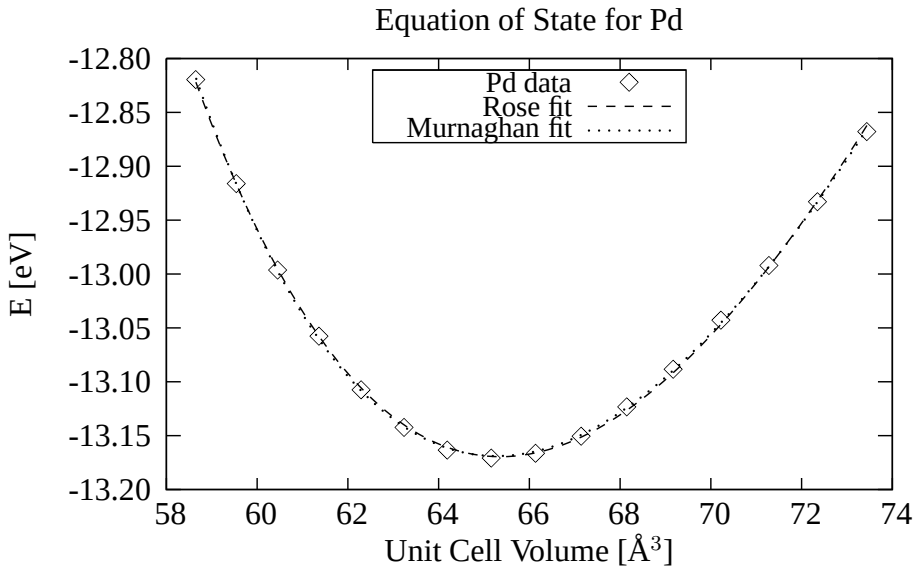

Figure E.2: Fit to the total energy as a function of unit cell volume for Pd. The minimum lattice parameter was found to be 4.026 Å.

E.1.2 Bulk PdZn

The PdZn calculation likewise improved from fixing the grid points at $24 \times 24 \times 24$ and narrowing the range of lattice parameters. The equilibrium lattice parameter decreased slightly from the bulk Pd calculation to 3.981 Å.

E.1.3 Bulk Pd_3Zn

The Pd_3Zn behaved similarly to the bulk Pd. The lattice parameter was 4.005 Å and the bulk modulus was 115.21 GPa, which closely mirrored the values obtained for Pd.

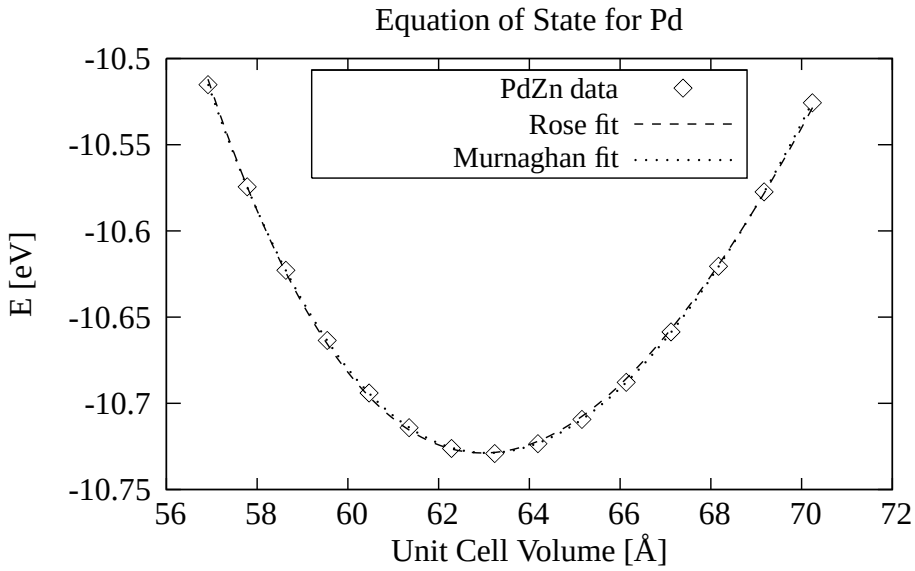

Figure E.3: PdZn total energy with respect to unit cell volume. The minimum lattice parameter was 3.981 Å.

E.1.4 Bulk $PdZn_3$

$PdZn_3$ demonstrated substantially lower energy values than the other alloys due to the high concentration of Zn atoms in the lattice. Since Zn is an hcp crystal, not fcc, it is likely that the minimum energy calculated is not a true minimum. Further investigations in which the Pd is treated as the dopant in an hcp system are underway.

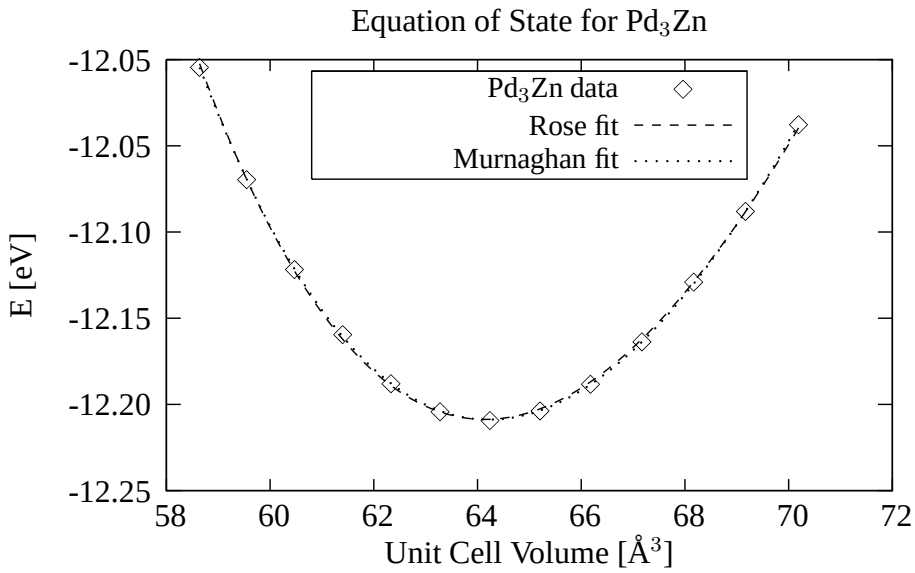

Figure E.4: Fit to the total energy as a function of unit cell volume for Pd_3Zn. The minimum lattice parameter was 4.005 Å.

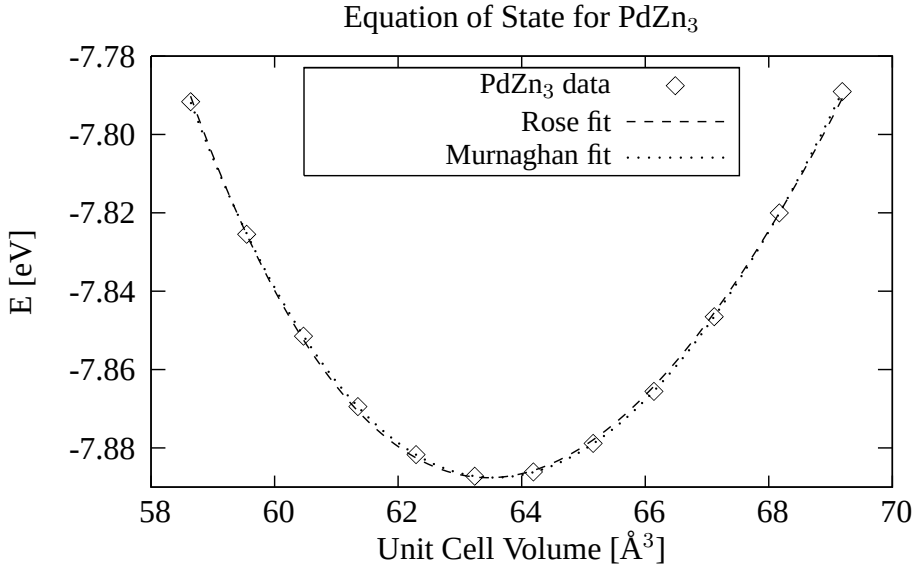

Figure E.5: Plot of $PdZn_3$ total energy with respect to the unit cell volume.

Table E.1: Equilibrium lattice parameters (Å) and bulk moduli (GPa) of Pd and Pd_XZn_Y alloys.

Material	a_0(Å)	B_0(GPa)
Pd	4.026	126.44
Pd [111]	3.94	163
PdZn	3.981	95.74
PdZn[19]	4.148	Not Available
Pd_3Zn	4.005	115.21
$PdZn_3$	3.991	71.6

References

[1] R. T. Downs and M. Hall-Wallace. The American Mineralogist Crystal Structure Database. *American Mineralogist*, 88:247–250, 2003.

[2] Koichi Momma and Fujio Izumi. An integrated three-dimensional visualization system VESTA using wxWidgets. *Commission on Crystallographic Computing International Union of Crystallography Newsletter*, 7:106–119, 2006.

[3] Ayman Karim. *Pd-Zn Catalyst Design for Pd-Zn Catalyst Design for Steam Reforming of Methanol*. PhD thesis, University of New Mexico, Albuquerque, NM, 2006.

[4] Nobuhiro Iwasa and Nobutsune Takezawa. New Supported Pd and Pt Alloy Catalysts for Steam Reforming and Dehydrogenation of Methanol. *Topics in Catalysis*, V22(3):215–224, 2003. doi: 10.1023/A:1023571819211.

[5] Ayman M. Karim, Travis Conant, and Abhaya K. Datye. Controlling ZnO morphology for improved methanol steam reforming reactivity. *Physical Chemistry Chemical Physics*, 10:5584–5590, July 2008. doi: 10.1039/b800009c.

[6] Michael D. Abràmoff, Paulo J. Magalhães, and Sunanda J. Ram. Image processing with imageJ. *Biophotonics International*, 11(7):36–41, 2004.

[7] Felix Studt, Frank Abild-Pedersen, Thomas Bligaard, Rasmus Z. Sørensen, Claus H. Christensen, and Jens K. Nørskov. Identification of Non-Precious Metal

Alloy Catalysts for Selective Hydrogenation of Acetylene. *Science*, 320(5881): 1320–1322, 2008. doi: 10.1126/science.1156660.

[8] Darren Browning, Peter Jones, and Ken Packer. An investigation of hydrogen storage methods for fuel cell operation with man-portable equipment. *Journal of Power Sources*, 65(1-2):187–195, 1997.

[9] Stephen Brunauer, P. H. Emmett, and Edward Teller. Adsorption of Gases in Multimolecular Layers. *Journal of the American Chemical Society*, 60(2):309–319, 1938.

[10] R. Rashidi, I. Dincer, G. F. Naterer, and P. Berg. Performance evaluation of direct methanol fuel cells for portable applications. *Journal of Power Sources*, 187(2): 509–516, 2009.

[11] G. Aydinli, N. S. Sisworahardjo, and M. S. Alam. Reliability and sensitivity analysis of low power portable direct methanol fuel cell. In *EUROCON 2007 - The International Conference on Computer as a Tool, Sep 9-12 2007*, pages 1457–1462. Institute of Electrical and Electronics Engineers Computer Society, 2007.

[12] H. Dohle, J. Divisek, and R. Jung. Process engineering of the direct methanol fuel cell. *Journal of Power Sources*, 86(1-2):469–477, 2000.

[13] Andrea Casalegno, Paolo Grassini, and Renzo Marchesi. Experimental analysis of methanol cross-over in a direct methanol fuel cell. *Applied Thermal Engineering*, 27(4):748–754, 2007.

[14] K. Scott, W. M. Taama, and P. Argyropoulos. Engineering aspects of the direct methanol fuel cell system. *Journal of Power Sources*, 79(1):43–59, 1999.

[15] Jamelyn D. Holladay, Yong Wang, and Evan Jones. Review of developments in portable hydrogen production using microreactor technology. *Chemical Reviews*, 104(10):4767–4789, 2004.

[16] Kok Hwa Lim, Zhao-Xu Chen, Konstantin M. Neyman, and Notker Rösch. Comparative theoretical study of formaldehyde decomposition on PdZn, Cu, and Pd surfaces. *Journal of Physical Chemistry B*, 110(30):14890–14897, 2006.

[17] Simon Penner, Bernd Jenewein, Harald Gabasch, Bernhard Klotzer, Di Wang, Axel Knop-Gericke, Robert Schlögl, and Konrad Hayek. Growth and structural stability of well-ordered PdZn alloy nanoparticles. *Journal of Catalysis*, 241(1):14 – 19, 2006. ISSN 0021-9517.

[18] Travis Conant. *Pd-Zn Bimetallic Catalysts for the Steam Pd-Zn Bimetallic Catalysts for the Steam Reforming of Methanol*. PhD thesis, University of New Mexico, Albuquerque, NM, May 2008.

[19] Zhao-Xu Chen, Konstantin M. Neyman, Aleksey B. Gordienko, and Notker Rösch. Surface Structure and Stability of PdZn and PtZn Alloys:Density-functional Slab Model Studies. *Phys. Rev. B*, 68(7):075417, Aug 2003.

[20] Kok Hwa Lim. *Density Functional Studies Relevant to Methanol Steam Reforming on PdZn*. PhD thesis, Technischen Universität München, 2006.

[21] Ayman Karim, Travis Conant, and Abhaya Datye. The Role of PdZn Alloy Formation and Particle Size on the Selectivity for Steam Reforming of Methanol. *Journal of Catalysis*, 243(2):420 – 427, 2006.

[22] E. Jeroro, V. Lebarbier, A. Datye, Y. Wang, and J.M. Vohs. Interaction of CO with surface PdZn alloys. *Surface Science*, 601(23):5546 – 5554, 2007.

[23] B. Halevi and John M. Vohs. Reactions of CH_3SH and $(CH_3)_2S_2$ on the (0001) and $(000\bar{1})$ surfaces of ZnO. *Journal of Physical Chemistry B*, 109(50):23976–23982, 2005. ISSN 15206106.

[24] Matthew P. Hyman, Vannesa M. Lebarbier, Yong Wang, Abhaya K. Datye, and John M. Vohs. A Comparison of the Reactivity of Pd Supported on ZnO$(10\bar{1}0)$ and

ZnO(0001). *The Journal of Physical Chemistry C*, 113(17):7251–7259, 2009. ISSN 1932-7447. doi: 10.1021/jp809934f.

[25] Jianli Hu, Yong Wang, Dave VanderWiel, Cathy Chin, Daniel Palo, Robert Rozmiarek, Robert Dagle, James Cao, Jamie Holladay, and Ed Baker. Fuel processing for portable power applications. *Chemical Engineering Journal*, 93(1):55 – 60, 2003.

[26] S. T. Liu, K. Takahashi, K. Fuchigami, and K. Uematsu. Hydrogen production by oxidative methanol reforming on Pd/ZnO: Catalyst deactivation. *Applied Catalysis A: General*, 299:58 – 65, JAN 2006.

[27] A. Bayer, K. Flechtner, R. Denecke, H. P. Steinruck, K. M. Neyman, and N. Rosch. Electronic properties of thin Zn layers on Pd(111) during growth and alloying. *Surface Science*, 600(1):78 – 94, JAN 2006.

[28] H. Gabasch, A. Knop-Gericke, R. Schlögl, S. Penner, B. Jenewein, K. Hayek, and B. Klotzer. Zn adsorption on Pd(111): ZnO and PdZn alloy formation. *Journal of Physical Chemistry B*, 110(23):11391 – 11398, JUN 2006.

[29] I. Ritzkopf, S. Vukojevic, C. Weidenthaler, J. D. Grunwaldt, and F. Schuth. Decreased CO production in methanol steam reforming over Cu/ZrO_2 catalysts prepared by the microemulsion technique. *Applied Catalysis A: General*, 302(2):215 – 223, APR 2006.

[30] S. W. Kim, J. Park, Y. Jang, Y. Chung, S. Hwang, T. Hyeon, and Y. W. Kim. Synthesis of Monodisperse Palladium Nanoparticles. *Nano Letters*, 3(9):1289 – 1291, SEP 2003.

[31] S. H. Sun, C. B. Murray, D. Weller, L. Folks, and A. Moser. Monodisperse FePt Nanoparticles and Ferromagnetic FePt Nanocrystal Superlattices. *Science*, 287 (5460):1989 – 1992, MAR 2000.

[32] Gerd H. Woehrle, Leif O. Brown, and James E. Hutchison. Thiol-functionalized, 1.5-nm gold nanoparticles through ligand exchange reactions: Scope and mechanism of ligand exchange. *Journal of the American Chemical Society*, 127(7):2172 – 2183, 2005.

[33] Peter C. K. Vesborg, Ib Chorkendorff, Ida Knudsen, Olivier Balmes, Jesper Nerlov, Alfons M. Molenbroek, Bjerne S. Clausen, and Stig Helveg. Transient behavior of Cu/ZnO-based methanol synthesis catalysts. *Journal of Catalysis*, 262(1):65–72, 2 2009. doi: 10.1016/j.jcat.2008.11.028.

[34] W. H. Cheng, S. Akhter, and H. H. Kung. Structure sensitivity in methanol decomposition on ZnO single-crystal surfaces. *Journal of Catalysis*, 82(2):341–350, 1983. ISSN 0021-9517. doi: 10.1016/0021-9517(83)90200-2.

[35] H. Wilmer, M. Kurtz, K. V. Klementiev, O. P. Tkachenko, W. Grünert, O. Hinrichsen, A. Birkner, S. Rabe, K. Merz, M. Driess, Ch. Wöll, and M. Muhler. Methanol synthesis over ZnO: A structure-sensitive reaction? *Physical Chemistry Chemical Physics*, 5:4736–4742, 2003. doi: 10.1039/b304425d.

[36] J.M. Vohs and M.A. Barteau. Conversion of methanol, formaldehyde and formic acid on the polar faces of zinc oxide. *Surface Science*, 176(1-2):91–114, 1986. ISSN 0039-6028. doi: 10.1016/0039-6028(86)90165-2.

[37] Michael Bowker, Hilary Houghton, and Kenneth C. Waugh. Mechanism and kinetics of methanol synthesis on zinc oxide. *Journal of the Chemical Society, Faraday Transactions 1: Physical Chemistry in Condensed Phases*, 77:3023–3036, 1981. doi: 10.1039/F19817703023.

[38] Ulrike Diebold, Lynn Vogel Koplitz, and Olga Dulub. Atomic-scale properties of low-index ZnO surfaces. *Applied Surface Science*, 237(1-4):336–342, 2004.

[39] Olga Dulub, Lynn A. Boatner, and Ulrike Diebold. STM study of the geometric and electronic structure of ZnO(0 0 0 1)-Zn, (0 0 0 $\bar{1}$)-O, (1 0 $\bar{1}$ 0), and (1 1 $\bar{2}$ 0) surfaces. *Surface Science*, 519(3):201–217, 2002. ISSN 00396028.

[40] Kezban Ada, Murat Gökgöz, Müşerref Önal, and Yüksel Sarıkaya. Preparation and characterization of a ZnO powder with the hexagonal plate particles. *Powder Technology*, 181(3):285–291, 2008. ISSN 0032-5910. doi: 10.1016/j.powtec.2007.05.015.

[41] G. R. Li, T. Hu, G. L. Pan, T. Y. Yan, X. P. Gao, and H. Y. Zhu. Morphology-Function Relationship of ZnO: Polar Planes, Oxygen Vacancies, and Activity. *The Journal of Physical Chemistry C*, 112(31):11859–11864, 2008. ISSN 1932-7447. doi: 10.1021/jp8038626.

[42] C. X. Xu, X. W. Sun, Z. L. Dong, and M. B. Yu. Zinc oxide nanodisk. *Applied Physics Letters*, 85(17):3878–3880, 2004. doi: 10.1063/1.1811380.

[43] Feifei Wang and Ruibin Liu and Anlian Pan and Li Cao and Ke Cheng and Bofei Xue and Geng Wang and Qingbo Meng and Jinghong Li and Qi Li and Yanguo Wang and Taihong Wang and Bingsuo Zou. The optical properties of ZnO sheets electrodeposited on ITO glass. *Materials Letters*, 61(10):2000 – 2003, 2007. ISSN 0167-577X. doi: 10.1016/j.matlet.2006.08.007.

[44] V. Staemmler, K. Fink, B. Meyer, D. Marx, M. Kunat, S. Gil Girol, U. Burghaus, and Ch. Wöll. Stabilization of polar ZnO surfaces: Validating microscopic models by using CO as a probe molecule. *Physical Review Letters*, 90(10):106102/1 – 106102/4, 2003. ISSN 00319007.

[45] Q. Yu, C. Yu, H. Yang, W. Fu, L. Chang, J. Xu, R. Wei, H. Li, H. Zhu, M. Li, G. Zou, G. Wang, C. Shao, and Y. Liu. Growth of Dumbbell-like ZnO Microcrystals under Mild Conditions and their Photoluminescence Properties. *Inorganic Chemistry*, 46 (15):6204–6210, 2007. ISSN 0020-1669. doi: 10.1021/ic070008a.

[46] Mingsong Wang, Sung Hong Hahn, Jae Seong Kim, Jin Suk Chung, Eui Jung Kim, and Kee-Kahb Koo. Solvent-controlled crystallization of zinc oxide nano(micro)disks. *Journal of Crystal Growth*, 310(6):1213–1219, 2008. ISSN 0022-0248. doi: DOI: 10.1016/j.jcrysgro.2008.01.001.

[47] Zhengrong R Tian, James A Voigt, Jun Liu, Bonnie McKenzie, Matthew J McDermott, Mark A Rodriguez, Hiromi Konishi, and Huifang Xu. Complex and oriented ZnO nanostructures. *Nat Mater*, 2(12):821–6, Dec 2003. doi: 10.1038/nmat1014.

[48] H. M. Rietveld. A profile refinement method for nuclear and magnetic structures. *Journal of Applied Crystallography*, 2(2):65–71, Jun 1969. doi: 10.1107/S0021889869006558.

[49] A. C. Larson and R. B. Von Dreele. General Structure Analysis System (GSAS). Technical report, Los Alamos National Laboratory Report LAUR 86-748, 2004.

[50] Brian H. Toby. $EXPGUI$, a Graphical User Interface for $GSAS$. *Journal of Applied Crystallography*, 34(2):210–213, Apr 2001. doi: 10.1107/S0021889801002242.

[51] Seungho Cho, Ji-Wook Jang, Seung-Ho Jung, Bo Ram Lee, Eugene Oh, and Kun-Hong Lee. Precursor Effects of Citric Acid and Citrates on ZnO Crystal Formation. *Langmuir*, 25(6):3825–3831, 02 2009. doi: 10.1021/la804009g.

[52] Ann M. Chippindale, Simon J. Hibble, and Edward J. Bilbé. Dicopper(II) trihydroxide cyanoureate dihydrate. *Acta Crystallographica Section C*, 65(7):i39–i41, Jul 2009. doi: 10.1107/S0108270109020885. URL `http://dx.doi.org/10.1107/S0108270109020885`.

[53] Xueli Cao, Haibo Zeng, Ming Wang, Xijin Xu, Ming Fang, Shulin Ji, and Lide Zhang. Large Scale Fabrication of Quasi-Aligned ZnO Stacking Nanoplates. *The Journal of Physical Chemistry C*, 112(14):5267–5270, 2008. doi: 10.1021/jp800499r.

[54] Jeong Park, Cesar Aliaga, J. Renzas, Hyunjoo Lee, and Gabor Somorjai. The role of organic capping layers of platinum nanoparticles in catalytic activity of co oxidation. *Catal. Lett.*, 129(1-2):1–6, 2009. doi: 10.1007/s10562-009-9871-8.

[55] Takashi Harada, Shigeru Ikeda, Mayu Miyazaki, Takao Sakata, Hirotaro Mori, and Michio Matsumura. A simple method for preparing highly active palladium catalysts loaded on various carbon supports for liquid-phase oxidation and hydrogenation reactions. *J. Mol. Catal. A: Chem.*, 268(1-2):59–64, 2007. ISSN 1381-1169. doi: 10.1016/j.molcata.2006.12.010.

[56] Hidefumi Hirai. Formation and catalytic functionality of synthetic polymer-noble metal colloid. *J. Macromol. Sci. Part A Pure Appl. Chem.*, 13(5):633–649, 1979. ISSN 0022-233x. doi: 10.1080/00222337908056678.

[57] Kunio Esumi, Tetsuyuki Itakura, and Kanjiro Torigoe. Preparation of organo palladium sols from palladium complexes in various alcohols. *Colloids Surf., A*, 82(1): 111–113, 1994. ISSN 0927-7757. doi: 10.1016/0927-7757(93)02619-P.

[58] John S. Bradley, Ernestine W. Hill, Carl Klein, Bruno Chaudret, and Anne Duteil. Synthesis of monodispersed bimetallic palladium-copper nanoscale colloids. *Chem. Matr.*, 5(3):254–256, 1993. doi: 10.1021/cm00027a005.

[59] Royale S. Underhill and Guojun Liu. Preparation and performance of pd particles encapsulated in block copolymer nanospheres as a hydrogenation catalyst. *Chem. Matr.*, 12(12):3633–3641, 2000. doi: 10.1021/cm0005743.

[60] Mathias Brust, Merryl Walker, Donald Bethell, David J. Schiffrin, and Robin Whyman. Synthesis of thiol-derivatised gold nanoparticles in a two-phase liquid-liquid system. *J. Chem. Soc., Chem. Commun.*, 7:801–802, 1994.

[61] Owen C. Compton and Frank E. Osterloh. Evolution of Size and Shape in the

Colloidal Crystallization of Gold Nanoparticlesau. *J. Am. Chem. Soc.*, 129(25): 7793–7798, 2007. ISSN 0002-7863. doi: 10.1021/ja069033q.

[62] Ana Rodriguez, Catherine Amiens, Bruno Chaudret, Marie-Jose Casanove, Pierre Lecante, and John S. Bradley. Synthesis and isolation of cuboctahedral and icosahedral platinum nanoparticles. ligand-dependent structures. *Chem. Matr.*, 8(8):1978–1986, 1996. doi: 10.1021/cm960338l.

[63] Hidefumi Hirai and Noboru Yakura. Protecting polymers in suspension of metal nanoparticles. *Polym. Advan. Technol.*, 12(11-12):724–733, 2001. ISSN 1099-1581. doi: 10.1002/pat.95.

[64] T. Teranishi and M. Miyake. Size control of palladium nanoparticles and their crystal structures. *Chem. Matr.*, 10(2):594 – 600, Feb 1998. ISSN 0897-4756. doi: 10.1021/cm9705808.

[65] John S. Bradley, Ernestine W. Hill, Bruno Chaudret, and Anne Duteil. Surface chemistry on colloidal metals. reversible adsorbate-induced surface composition changes in colloidal palladium-copper alloys. *Langmuir*, 11(3):693–695, 1995. doi: 10.1021/la00003a002.

[66] Weixia Tu and Hanfan Liu. Rapid synthesis of nanoscale colloidal metal clusters by microwave irradiation. *J. Mater. Chem.*, 10:2207–2211, 2000. doi: 10.1039/B002232M.

[67] Lokesh Kesavan, Ramchandra Tiruvalam, Mohd Hasbi Ab Rahim, Mohd Izham bin Saiman, Dan I. Enache, Robert L. Jenkins, Nikolaos Dimitratos, Jose A. Lopez-Sanchez, Stuart H. Taylor, David W. Knight, Christopher J. Kiely, and Graham J. Hutchings. Solvent-Free Oxidation of Primary Carbon-Hydrogen Bonds in Toluene Using Au-Pd Alloy Nanoparticles. *Science*, 331(6014):195–199, 2011. doi: 10.1126/science.1198458.

[68] Maria Mifsud, Ksenia V. Parkhomenko, Isabel W.C.E. Arends, and Roger A. Sheldon. Pd nanoparticles as catalysts for green and sustainable oxidation of functionalized alcohols in aqueous media. *Tetrahedron*, 66(5):1040–1044, 2010. ISSN 0040-4020. doi: DOI: 10.1016/j.tet.2009.11.007.

[69] Patrick Burton, David Lavenson, Michael Johnson, David Gorm, Ayman Karim, Travis Conant, Abhaya Datye, Bernadette Hernandez-Sanchez, and Timothy J. Boyle. Synthesis and Activity of Heterogeneous Pd/Al_2O_3 and Pd/ZnO Catalysts Prepared from Colloidal Palladium Nanoparticles. *Top. Catal.*, 49(3):227–232, 2008. doi: 10.1007/s11244-008-9092-1.

[70] Andrzej Gniewek, Józef J. Ziólkowski, Anna M. Trzeciak, Miroslaw Zawadzki, Hanna Grabowska, and Józef Wrzyszcz. Palladium nanoparticles supported on alumina-based oxides as heterogeneous catalysts of the suzuki-miyaura reaction. *J. Catal.*, 254(1):121–130, 2008. ISSN 0021-9517. doi: DOI: 10.1016/j.jcat.2007.12.004.

[71] Kunio Esumi, Takafumi Tano, Kanjiro Torigoe, and Kenjiro Meguro. Preparation and characterization of bimetallic palladium-copper colloids by thermal decomposition of their acetate compounds in organic solvents. *Chem. Matr.*, 2(5):564–567, 1990. doi: 10.1021/cm00011a019.

[72] J. Athilakshmi, S. Ramanathan, and Dillip Kumar Chand. Facile synthesis of palladium nanoclusters and their catalytic activity in sonogashira coupling reactions. *Tetrahedron Letters*, 49(36):5286–5288, 2008. ISSN 0040-4039. doi: 10.1016/j.tetlet.2008.06.089.

[73] V. Ananikov and I. Beletskaya. Using nanosized, homogeneous, and heterogeneous catalytic systems in organic synthesis: changing the structure of active center in chemical reactions in solution. *Nanotechnol. Russ.*, 5(1):1–17, 2010. doi: 10.1134/S1995078010010015.

[74] Xiaomei Chen, Genghuang Wu, Jinmei Chen, Xi Chen, Zhaoxiong Xie, and Xiaoru Wang. Synthesis of "clean and well-dispersive pd nanoparticles with excellent electrocatalytic property on graphene oxide. *Journal of the American Chemical Society*, ASAP(DOI 10.1021/ja110313d), 2011. doi: 10.1021/ja110313d.

[75] Marvin M. Johnson, Darrell W. Walker, and Gerhard P. Nowack. Selective hydrogenation catalyst. United States Patent 4,404,124, Standard Oil Company, Chicago, IL, Sep 1983.

[76] Jürgen Osswald, Kirill Kovnir, Marc Armbrüster, Rainer Giedigkeit, Rolf E. Jentoft, Ute Wild, Yuri Grin, and Robert Schlögl. Palladium-gallium intermetallic compounds for the selective hydrogenation of acetylene: Part ii: Surface characterization and catalytic performance. *J. Catal.*, 258(1):219–227, 2008. ISSN 0021-9517. doi: 10.1016/j.jcat.2008.06.014.

[77] H. Molero, B. F. Bartlett, and W. T. Tysoe. The hydrogenation of acetylene catalyzed by palladium: Hydrogen pressure dependence. *J. Catal.*, 181(1):49–56, 1999. ISSN 0021-9517. doi: 10.1006/jcat.1998.2294.

[78] Willem G. Augustyn, Robert I. McCrindle, and Neil J. Coville. The selective hydrogenation of acetylene on palladium-carbon nanostructured catalysts. *Applied Catalysis A: General*, 388(1-2):1–6, 2010. ISSN 0926-860X. doi: 10.1016/j.apcata.2010.07.038.

[79] Thomas A. Westrich, Xiaoyin Chen, and Johannes W. Schwank. Isooctane decomposition and carbon deposition over ceria-zirconia supported nickel catalysts. *Applied Catalysis A: General*, 386(1-2):83–93, 2010. ISSN 0926-860X. doi: 10.1016/j.apcata.2010.07.029.

[80] R. J. Liu, P. A. Crozier, C. M. Smith, D. A. Hucul, J. Blackson, and G. Salaita. Metal sintering mechanisms and regeneration of palladium/alumina hydrogena-

tion catalysts. *Applied Catalysis A: General*, 282(1-2):111–121, 2005. doi: 10.1016/j.apcata.2004.12.015.

[81] H. P. Choo, K. Y. Liew, and H. F. Liu. Factors affecting the size of polymer stabilized Pd nanoparticles. *Journal of Materials Chemistry*, 12(4):934 – 937, 2002. ISSN 0959-9428. doi: 10.1039/b108260b.

[82] Chengmin Shen, Chao Hui, Tianzhong Yang, Congwen Xiao, Jifa Tian, Lihong Bao, Shutang Chen, Hao Ding, and Hongjun Gao. Monodisperse noble-metal nanoparticles and their surface enhanced raman scattering properties. *Chemistry of Materials*, 20(22):6939–6944, 2008. doi: 10.1021/cm800882n.

[83] Bernhard Gehl, Andreas Frömsdorf, Vesna Aleksandrovic, Thomas Schmidt, Angelika Pretorius, Jan-Ingo Flege, Sigrid Bernstorff, Andreas Rosenauer, Jens Falta, Horst Weller, and Marcus Bäumer. Structural and chemical effects of plasma treatment on close-packed colloidal nanoparticle layers. *Advanced Functional Materials*, 18(16):2398–2410, AUG 22 2008. ISSN 1616-301X. doi: 10.1002/adfm.200800274.

[84] Patrick D. Burton, Timothy J. Boyle, and Abhaya K. Datye. Facile, surfactant-free synthesis of pd nanoparticles for heterogeneous catalysts. In Press, 2011.

[85] Detre Teschner, János Borsodi, Zoltán Kis, László Szentmiklósi, Zsolt Révay, Axel Knop-Gericke, Robert Schlögl, Daniel Torres, and Philippe Sautet. Role of Hydrogen Species in Palladium-Catalyzed Alkyne Hydrogenation. *The Journal of Physical Chemistry C*, 114(5):2293–2299, 2010. doi: 10.1021/jp9103799.

[86] Priyam A. Sheth, Matthew Neurock, and C. Michael Smith. First-principles analysis of the effects of alloying pd with ag for the catalytic hydrogenation of acetyleneethylene mixtures. *The Journal of Physical Chemistry B*, 109(25):12449–12466, 2005. doi: 10.1021/jp050194a.

[87] Mónica García-Mota, Blaise Bridier, Javier Pérez-Ramírez, and Núria López. Interplay between carbon monoxide, hydrides, and carbides in selective alkyne hydrogenation on palladium. *Journal of Catalysis*, 273(2):92 – 102, 2010. ISSN 0021-9517. doi: 10.1016/j.jcat.2010.04.018.

[88] J. Will Medlin and Mark D. Allendorf. Theoretical Study of the Adsorption of Acetylene on the (111) Surfaces of Pd, Pt, Ni, and Rh. *The Journal of Physical Chemistry B*, 107(1):217–223, 2003. doi: 10.1021/jp026555t.

[89] Detre Teschner, Zsolt Révay, János Borsodi, Michael Hävecker, Axel Knop-Gericke, Robert Schlögl, David Milroy, S. David Jackson, Daniel Torres, and Philippe Sautet. Understanding Palladium Hydrogenation Catalysts: When the Nature of the Reactive Molecule Controls the Nature of the Catalyst Active Phase. *Angewandte Chemie International Edition*, 47(48):9274–9278, 2008. ISSN 1521-3773. doi: http://dx.doi.org/10.1002/anie.200802134.

[90] Tangui Le Bahers, Thierry Pauporté, Frédéric Labat, Grégory Lefèvre, and Ilaria Ciofini. Acetylacetone, an interesting anchoring group for zno-based organicinorganic hybrid materials: A combined experimental and theoretical study. *Langmuir*, 27(7):3442–3450, 2011. doi: 10.1021/la103634v. URL `http://pubs.acs.org/doi/abs/10.1021/la103634v`.

[91] William R. McNamara, Robert C. Snoeberger, Gonghu Li, James M. Schleicher, Clyde W. Cady, Macarena Poyatos, Charles A. Schmuttenmaer, Robert H. Crabtree, Gary W. Brudvig, and Victor S. Batista. Acetylacetonate anchors for robust functionalization of tio_2 nanoparticles with mn(ii)terpyridine complexes. *Journal of the American Chemical Society*, 130(43):14329–14338, 2008. doi: 10.1021/ja805498w. URL `http://pubs.acs.org/doi/abs/10.1021/ja805498w`.

[92] P. Hohenberg and W. Kohn. Inhomogenous Electron Gas. *Physical Review*, 136 (3B):B864–B871, Nov 1964.

[93] Jürgen Hafner. *Ab-initio* simulations of matrials using VASP; Density-functional theory and beyond. *Jounal of Computational Chemistry*, 29(13):2044–2078, 2008.

[94] Kieron Burke and friends. The ABC of DFT. URL `http://dft.uci.edu/book/gamma/g1.pdf`.

[95] W. Kohn and L. J. Sham. Self-Consistent Equations Including Exchange and Correlation Effects. *Phys. Rev.*, 140(4A):A1133–A1138, Nov 1965. doi: 10.1103/PhysRev.140.A1133.

[96] Melanie T. Schaal, Matthew P. Hyman, Meghana Rangan, Shuguo Ma, Christopher T. Williams, John R. Monnier, and J. Will Medlin. Theoretical and experimental studies of Ag-Pt interactions for supported Ag-Pt bimetallic catalysts. *Surface Science*, 603(4):690–696, 2 2009/2/15.

[97] Jeff Greeley and Jens K. Nørskov. A general scheme for the estimation of oxygen binding energies on binary transition metal surface alloys. *Surface Science*, 592 (1-3):104–111, 2005. ISSN 0039-6028. doi: 10.1016/j.susc.2005.07.018.

[98] K. M. Neyman, R. Sahnoun, C. Inntam, S. Hengrasmee, and N. Rösch. Computational study of model Pd-Zn nanoclusters and their adsorption complexes with CO molecules. *Journal of Physical Chemistry B*, 108(17):5424 – 5430, APR 2004. ISSN 1520-6106.

[99] J. J. Mortensen, L. B. Hansen, and K. W. Jacobsen. Real-space grid implementation of the projector augmented wave method. *Phys. Rev. B*, 71(3):035109, JAN 2005. ISSN 1098-0121. doi: 10.1103/PhysRevB.71.035109.

[100] Peter E. Blöchl, Clemens J. Först, and Johannes Schimpl. Projector augmented

wave method: *Ab initio* molecular dynamics with full wave functions. *Bulletin of Materials Science*, 26(1):33–41, 2003.

[101] S. R. Bahn and K. W. Jacobsen. An object-oriented scripting interface to a legacy electronic structure code. *Comput. Sci. Eng.*, 4(3):56–66, MAY-JUN 2002. ISSN 1521-9615. doi: 10.1109/5992.998641.

[102] B. Hammer, L. B. Hansen, and J. K. Nørskov. Improved Adsorption Energetics Within Density-Functional Theory Using Revised Perdew-Burke-Ernzerhof Functionals. *Phys. Rev. B*, 59(11):7413–7421, Mar 1999.

[103] J. H. Li, S. H. Liang, H. B. Guo, and B. X. Liu. Four-parameter equation of state of solids. *Applied Physics Letters*, 87(19):194111, 2005.

[104] George Blyholder. Molecular Orbital View of Chemisorbed Carbon Monoxide. *Journal of Physical Chemistry*, 68(10):2772, 1964.

[105] P.A. Redhead. Thermal desorption of gases. *Vacuum*, 12(4):203–211, 1962. ISSN 0042-207X. doi: DOI: 10.1016/0042-207X(62)90978-8.

[106] Yucheng Huang, Weiping Ding, and Zhao-Xu Chen. Effect of zn on the adsorption of co on pd(111). *The Journal of Chemical Physics*, 133(21):214702, 2010. doi: 10.1063/1.3512631.

[107] Mark Bowden. ConvX–Data File Conversion Software for Windows 95, 2000.

[108] J. J. Mortensen, L. B. Hansen, and K. W. Jacobsen. Real-space Grid Implementation of the Projector Augmented Wave Method. *Phys. Rev. B*, 71(3):035109, JAN 2005.

[109] F. D. Murnaghan. The Compressibility of Media under Extreme Pressures. *Proceedings of the National Academy of Sciences of the United States of America*, 30 (9):244–247, 1944. ISSN 00278424.

[110] V. G. Tyuterev and Nathalie Vast. Murnaghan's equation of state for the electronic ground state energy. *Computational Materials Science*, 38(2):350–353, 2006/12.

[111] Mira Todorova, Karsten Reuter, and Matthias Scheffler. Oxygen Overlayers on Pd(111) Studied by Density Functional Theory. *Journal of Physical Chemistry B*, 108(38):14477–14483, 2004.